ABSTRACT

Title of Dissertation:	SHAPE AND DOUBLE BLUE ZONES IN LAMINAR CO-FLOW DIFFUSION FLAMES
	Zhengyang Wang, Doctor of Philosophy, 2019
Dissertation directed by:	Professor Peter B. Sunderland Department of Fire Protection Engineering

Many studies have examined the stoichiometric lengths of laminar gas jet diffusion flames. However, these have emphasized normal flames of undiluted fuel burning in air. Many questions remain about the effects of fuel dilution, oxygen-enhanced combustion, and inverse flames. In addition, past experimental and computational work indicates that double blue zones are possible in hydrocarbon diffusion flames. However, much remains unknown about double blue zones in diffusion flames.

Thus, in this dissertation, the shape and double blue zones of the laminar co-flow jet diffusion flames are studied for more than 300 normal and inverse diffusion flames. Flame conditions including fuel type, reactant mole fraction, reactant flow rate, dilution agents, burner port material, burner port diameter, and flame T_{ad} and Z_{st} are varied. Chemiluminescence associated with excited species (C_2^*, CO_2^* CH^*, and OH^*) are measured through image deconvolution and broadband CO_2^* emission correction. Temperatures are measured with B-type thermocouples and TFP.

Nitrogen addition to the fuel and/or oxidizer is found to increase the stoichiometric lengths of both normal and inverse diffusion flames, but this effect is small at high reactant mole fraction. This counters previous assertions that inert addition to the fuel stream has a negligible effect on the lengths of normal diffusion flames. The analytical model of Roper is extended to these conditions by specifying the characteristic diffusivity to be the mean diffusivity of the fuel and oxidizer into stoichiometric products and a characteristic temperature that scales with the adiabatic flame temperature and the ambient temperature. The extended model correlates the measured lengths of normal and inverse flames with coefficients of determination of 0.87 for methane and 0.97 for propane.

Double blue zones, separated by up to 1.6 mm (and 0.9 mm) at the flame tip for IDFs (and NDFs), are observed in all the flames we measured. For both flame types, the blue zone toward the fuel side is rich and blue-green, while that toward the oxidizer side is stoichiometric, blue, and thicker. The rich zone results from emissions from CH^* and C_2^*. The stoichiometric zone results from CO_2^* emissions and is coincident with the peak in OH^*. All the deconvolved spectral emissive power peaks are higher in the IDF than in the NDF owing to higher scalar dissipation rates. The temperature profile of an NDF (and an IDF) was measured by B type thermocouple (and TFP). The result support the finding that the temperature peaks at the stoichiometric location for both NDFs and IDFs.

SHAPE AND DOUBLE BLUE ZONES IN LAMINAR CO-FLOW DIFFUSION FLAMES

by

Zhengyang Wang

Dissertation submitted to the Faculty of the Graduate School of the
University of Maryland, College Park, in partial fulfillment
of the requirements for the degree of
Doctor of Philosophy
2019

Advisory Committee:
Professor Peter B. Sunderland (Fire Protection Engineering), Chair
Associate Professor Johan Larsson (Mechanical Engineering)
Associate Professor Michael J. Gollner (Fire Protection Engineering)
Associate Professor Stanislav I. Stoliarov (Fire Protection Engineering)
Professor Bao Yang (Mechanical Engineering)

Acknowledgements

This work is supported by the Advanced Combustion via Microgravity Experiments (ACME) program Flame Design project from NASA and Teaching Assistantship from the Department of Fire Protection Engineering.

First and foremost I'd like to thank my Ph.D advisor, Professor Peter Sunderland. He taught me how to think and conduct research scientifically, and presenting work concisely and precisely. It is very lucky for me to work with him.

I would also like to thank my committee, Dr. Bao Yang, Dr. Johan Larsson, Dr. Michael J. Gollner, Dr. Stanislav I. Stoliarov, Dr. Arnaud Trouvé and Dr. Christopher Cadou (Dr. Trouvé and Dr. Cadou were in my proposal committee) for their invaluable suggestions.

I would like to specially thank my master advisor, Prof. Liangbing Hu. He brought me to his lab at my first master year. Trained me, instructed me and pushed me to my next level.

I would like to specially thank Dr. Sunderland's group members, Dennis Kim, Akshit Markan, Parham Dehghani, Hanju Lee, Paul Anderson, Haiqing Guo, Eric Auth. Special thanks to Dennis as a great associate and friend.

I would also like to thank all my friends, staffs, and faculties in the department of fire protection engineering for their assistance and encouragement during my study. Special thanks to Yan Ding, Conor Mccoy and Sriram Hariharan who gave me great help in the past three years.

Table of Contents

List of Tables

List of Figures

List of Abbreviations

α	An empirical factor (Chapter 3)
	Ratios of CO_2^* intensity at wavelength λ divided by that at 455 nm (Chapter 4)
	Thermal diffusivity of air (Appendix B)
β	Ratios of CO_2^* pixel sensitivity at wavelength λ divided by that at 455 nm. (Chapter 4)
	Thermal expansion coefficient (Appendix B)
C_1	The first radiation constants (3.742×10^{-4} W-m^2)
C_2	The second radiation constants (1.439×10^4 μm/K)
CCD	Charge coupled device
CMOS	Complementary metal-oxide-semiconductor
D	Deconvolution operator
D	Travel length
D_o	Characteristic diffusivity of the gas mixture at ambient temperature
D_{bead}	Bead diameter
D_{k-j}	Binary diffusivity of species k and j
D [$E(\lambda)$]	Deconvolved spectral emissive power at its chemiluminescence peak
DAQ	Data acquisition
ε	Emissivity
E_b	Spectral emissive power of an ideal blackbody
$E_{species}$	Emissivity power of chemiluminenscence species
f	Camera f-number
$FWHM$	Bandpass filter's full-width at half maximum
g	Acceleration of gravity (9.81 m/s^2)

γ	Ratios of CO_2^* τ at wavelength λ divided by that at 455 nm
i	Camera and the color plane (Chapter 4)
I_B	Blue pixel values
ICCD	Intensified charge-coupled device
I_{DC}	Dark-current pixel values
IDFs	Inverse diffusion flames
I_G	Green pixel values
I_R	Red pixel values
ISO	International Organization for Standardization
k	Air thermal conductivity
L_{st}	Stoichiometric flame length
λ	Wavelength
$\dot{m}_{CH4}$	Methane mass flow rate
$\dot{m}_{O2}$	Oxygen mass flow rate
NDFs	Normal diffusion flames
NI	Normalized pixel values
Nu	Nusselt number
OH PLIF	Laser-induced fluorescence of hydroxyl radicals
ρ	Density of air
Pr	Prandtl number
Q	Volumetric flow rate of the inner port gas at ambient conditions
Ra	Rayleigh number
RGB	Red, green, and blue

S	The ratio of the volume of outer port gas to the volume of inner port gas for stoichiometric combustion (Chapter 3)
	Camera pixel sensitivity (Chapter 4)
t	Exposure time (Chapter 4)
	Travel time (Chapter 5)
T	Temperature (Chapter 4)
T_{ad}	The adiabatic flame temperature
T_f	Characteristic temperature for mass diffusion
T_m	Temperature measured by thermocouple
ΔT	Corrected temperature
T_0	Ambient temperature
TFP	Thin filament pyrometer
τ	Bandpass filter's peak transmittance
UV	Ultraviolet
V	Fixed excitation
V_{slide}	Corresponding voltage
X_{CH4}	Methane mole fraction
X_{O2}	Oxygen mole fraction
Z_{st}	Stoichiometric mixture fractions

Chapter 1 Introduction and Motivation

Combustion has been played an important role in society for centuries. Over 80% of world energy is converted by combustion including power generation and transportation [1]. Renewable energy is developed rapidly, but economic and safety issues complicate the application of this new energy [2-4]. As a result, combustion will remain as the major energy conversion process for a long time. The biggest challenge in combustion is the low energy conversion efficiency. Combustion products (e.g. CO_2 and soot) cause serious environmental problems, such as global warming and smog. Thus, understanding combustion processes and controlling the reactions to increase the energy efficiency and reduce emissions pollution is essential.

1.1 Laminar Co-flow Diffusion Flame

Laminar co-flow diffusion flames are a fundamental flame model in combustion research. The interactions between flow fields and reactions can be readily modified and studied. Knowledge obtained from co-flow laminar diffusion flames is not only of fundamental importance, but also facilitates the study of turbulent diffusion flames in practical industrial combustors [5].

Laminar co-flow diffusion flames are typically studied as normal diffusion flames (NDFs) due to their wide applications. Figure 1-1a presents an image of a methane NDF and a schematic of an NDF co-flow burner. Fuel flows through the inner burner port, while oxidizer flows through the outer port.

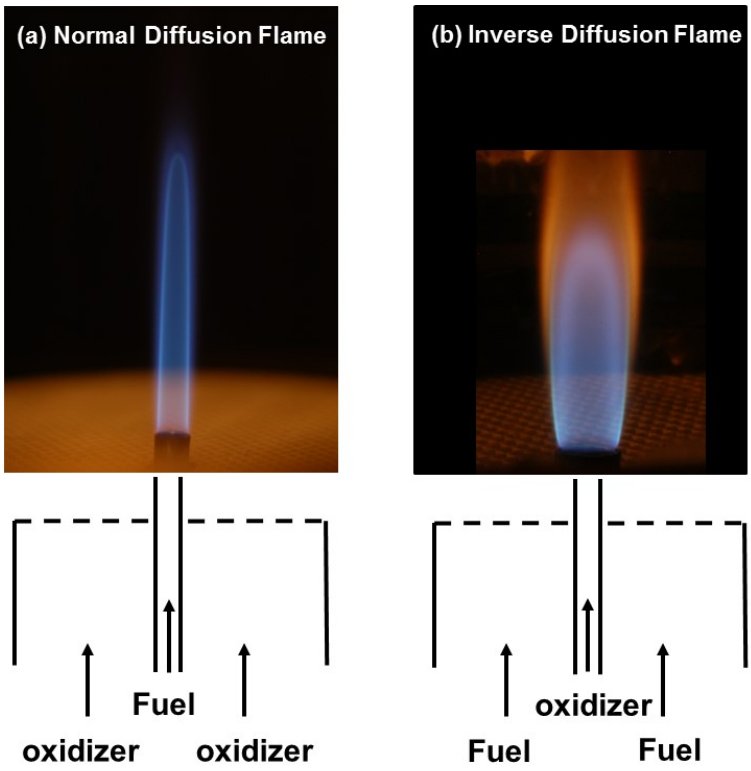

Figure 1-1: A schematics of (a) a normal diffusion flame and (b) an inverse diffusion flame.

Structurally inverse to the NDF, a laminar inverse co-flow diffusion flame (IDF) is a type of flame where oxidizer is surrounded by fuel (Figure 1-1b). Although these are less comment than NDFs in research and applications, they are equally important from a fundamental perspective and can be simulated with many of the same theories and numerical models [6-8].

1.2 Flame Length Measurement and Prediction

Flame length is an important flame property. It is affected by aerodynamics [9- 11], fuel properties [7,10], pressure [12], burner geometry [10], and gravity [10,13,14]. Flame length measurement and prediction is common in experiments and simulations.

1.2.1 Flame Length Measurement

Stoichiometric flame length is defined as the distance from the burner tip to the position on the axis where the fuel and oxidizer are in stoichiometric proportions. Flame length is measured visually by observing the thin blue luminous zone [15,16]. However, the blue region is difficult to observe for most sooty flames. Here, a luminous length can be used instead, which is the distance from the burner tip to the farthest part of the yellow region on the axis. This luminous length is assumed to be closed to the stoichiometric flame length (L_{st}) in lightly sooting, nonsmoking NDFs [10, 11, 17-19]. However, in heavily sooty NDFs, it is typically twice as long as the stoichiometric flame length [10,17-19]. Measurement of IDF stoichiometric flame lengths can be even more difficult as the soot in hydrocarbon IDFs forms outside and above the flames, obscuring the blue reaction zone [19].

Many diagnostic techniques have been used to measure stoichiometric flame lengths. Peak temperatures and maximum CO_2 concentrations were found to occur near the stoichiometric zone [17]. Roper *et. al* [20] used quartz microprobes and gas chromatography to measure the CO concentration on the centerline as an indication of flame length and the maximum temperature on the centerline (measured by a thermocouple) was used to determine the flame length [21, 22]. The peak blue intensity was capture by a color charge coupled device (CCD) camera with a 430 nm band pass filter, which indicated the luminosity of the CH^* [11,23]. Laser-induced fluorescence of hydroxyl radicals (OH PLIF) has also been used to measure stoichiometric lengths by detecting the highest OH concentrations [19].

1.2.2 Flame Length Prediction

Burke and Schumann [9] developed a classical model of stoichiometric flame length. The model assumed infinitely fast chemistry with a one-step global reaction. They also assumed parallel flow, uniform density, specific heat, and diffusion coefficient and unity Lewis number. Measured flame lengths agreed with the predictions.

The Burke and Schumann model was later refined by adjusting the assumptions [24,25]. Spalding [15] applied the Prandtl solution for a laminar free jet to a reactive flow. Roper [10] allowed axial velocity to vary with height and developed an often used correlation for NDF flame height for circular burners that depends only on fuel flow rate and stoichiometric air to fuel volume ratio. Roper also predicted length to be independent of gravity for circular port burners, as the competing effects of decreased advection time and decreased diffusion time cancel.

1.3 Dilution Effects on Flames

The burning of diluted fuels in ambients other than air has applications to exhaust-gas recirculation, oxygen-enhanced combustion, and fire safety [16,26-30]. For hydrocarbon flames, typical diluents are N_2, CO_2, CO and H_2O. Reactant dilution can result in thermal, chemical, diffusive, and radiative effects [16, 26-30].

Axelbaum and Law [27] found the thermal (and dilution) effects were dominant when moderate (and large) amounts of inert were added. Xu et al. [30] found both H_2O and CO_2 dilution decreased the flame temperatures due to the thermal and radiative effects. However, H_2O (CO_2) decreased (increased) flame height and radius due to the chemical and transport effects.

1.4 Double Blue Zones in Laminar Co-flow Diffusion Flames

Diffusion flames are composed of a rich zone, a lean zone, and a stoichiometric zone that separates them. According to the classical Burke–Schumann model, the stoichiometric zone is infinitely thin [9].

Several observations have questioned the model of an infinitely thin reaction zone. Diffusion flames with two reaction fronts have been predicted for hydrogen–fluorine systems [31]. The two reaction fronts are separated by a chemistry frozen diffusion zone. However, experimental evidence is lacking.

Many published color images of IDFs reveal parallel thin blue zones separated by a thin dark region [13,32-37]. These double blue zones are easily missed – only one study mentioned them [13]. They are evident for various fuels (CH_4, C_2H_4, C_2H_6, C_3H_8, and C_4H_{10}), in normal gravity and microgravity, in co-flowing and quiescent ambients, and in attached and lifted flames. The double zones are not visible in some IDFs [38- 40], nor in inverse spherical diffusion flames [41,42], perhaps owing to high soot loading and/or low image quality.

Double blue zones also are visible, although less pronounced, in many NDFs. For example, Gülder and co-workers [43-45] reported a two-zone structure in methane-oxygen flames. An inner blue region was surrounded by widely distributed blue haze. Saito et al. [17] reported similar behavior in methane-air flames. Weinberg and co-workers [46,47] observed distinct double blue zones in NDFs. All these studies [43- 47] attributed the zone toward the fuel to hydrocarbon oxidation and the zone toward the oxidizer to CO and/or H_2 oxidation.

Double blue zones were observed in CH_4-doped H_2 spherical inverse diffusion flames by Sung et al. [48]. The zones were separated by up to 8 mm. The zone toward the fuel was blue-green and was attributed to C_2^* emission from CH_4 consumption. The zone toward the oxidizer was blue and was attributed to CO_2^* emission from H_2 consumption. The double zones occurred only for CH_4 mole fractions in the fuel of 1.5 – 9.5%.

1.5 Chemiluminescence in Hydrocarbon Laminar Diffusion Flames

Flame chemiluminescence measurements are appealing in combustion research owing to their simplicity and non-intrusive nature [49-56]. The chemiluminescence of electronically excited radical species in a flame results from chemical reactions. Excited state species, such as C_2^*, CO_2^* CH^* and $OH^*$are responsible for most chemiluminescence in hydrocarbon flames. Their intensities provide information about local concentrations and reactions. Ratios of OH^*/CH^*, C_2^*/CH^*, and C_2^*/OH^* intensities in flames have been used to investigate the local reactions in both premixed [52,56] and diffusion flames [53]. Samaniego et al. [55] quantified the relationship between the species chemiluminescence intensities and heat release rates as functions of dilution, equivalence ratio, and steady and unsteady strain rates.

In hydrocarbon flames, the excited CO_2^* has broadband emissions that span the visible range [49-56]. Past work has corrected for this by mapping the target spectral emissions and subtracting the background intensity, which was assumed to be excited CO_2^* emission [50,52,53,56]. Kojima et al. [56] and Merotto et al. [53] measured methane/air laminar flame spectral intensities. They found the background intensity at 455 nm was same as at 430 nm, while 50% higher than that at 515 nm.

Giassi et al. [51] analyzed CH^* emissions and heat release rates in diluted methane NDFs in microgravity and normal gravity. They identified a radially extended CH^* emission zone, emissions from C_2^* and CO_2^*, and a 24 um displacement between the C_2^* and CH^* peaks. A sooty NDF in microgravity with double luminous zones was studied. By assuming the blue channel of the flame image only represents CH^* chemiluminescence, the inner luminous zone of the flame was subtracted as soot interference and the outer luminous zone was identified as CH^* chemiluminescence emissions.

Chapter 2 : Objectives

This study will focus on shape of the laminar co-flow jet diffusion flames. Five main objectives have been established in this study to further predict the flame shape and understand the chemistry. This research seeks to:

1) Study the effect of reactant diluent on the length of laminar gas jet diffusion flames. Measure the L_{st} of laminar co-flow normal and inverse diffusion flames. Vary the fuel type, reactant mole fraction, reactant flow rate, dilution agent, and burner port diameter.
2) Extend the analytical Roper model to these conditions. Consider properties of diluted reactant gases. Compare the predicted results with the measurements.
3) Examine the existence of double blue zones in both NDFs and IDFs. Vary the fuel type, reactant mole fraction, reactant flow rate, dilution agents, burner port material, burner port diameter, and flame T_{ad} and Z_{st} .
4) Investigate the flame chemiluminescence (C_2^*, CO_2^* CH^*, and OH^*) associated with double blue zones by using filtered images. Develop and apply image analysis, including image deconvolution and CO_2^* broadband emission. Calculate the $E_{species}$ of each image pixel.
5) Measure the temperature distributions of the double blue zones. Use and compare B type thermocouples and TFP. Seek relations among the flame temperature, flame major species chemiluminescence intensity (or intensity ratios) and local equivalent ratio.

Chapter 3 : Dilution Effects on Laminar Jet Diffusion Flame Lengths

3.1 Introduction

Laminar gas jet diffusion flames have been widely studied for both fundamental and practical reasons. To design burners and experiments, and to validate numerical models, it is helpful to understand the stoichiometric length behavior of these flames [14,16,22,57-60]. The burning of diluted fuels in ambients other than air has applications to exhaust-gas recirculation combustors, oxygen-enhanced combustion, and fire safety [16,26-30,61].

The effects of reactant dilution on stoichiometric lengths (L_{st}) of normal diffusion flames (NDFs) are not fully understood. McEnally and Pfefferle [22] found L_{st} increased monotonically as diluent was added to the fuel. In contrast, some experimental [62] and modeling [5,62] studies found L_{st} to be independent of diluent addition to the fuel. Oxidizer dilution was experimentally found to increase L_{st} [16]. None of these studies considered highly diluted fuels or oxygen enrichment.

Schug et al. [26] concluded from their experiments that "flame height … is strictly proportional to the volumetric fuel flow rate and not to the total rate of fuel plus additive." This claim was also published in other papers co-authored by Glassman. However, the flame heights measured in Ref. [26] were luminous lengths of sooty flames. Furthermore, subsequent experiments found inert addition could either reduce [63] or increase [64,65] luminous flame lengths.

Inverse diffusion flames (IDFs), where the oxidizer is surrounded by fuel, are less common in research and in applications. However, they are equally important from

a fundamental perspective and can be studied with many of the same diagnostics, theories, and numerical models [6-8]. To date the greatest research interest in IDFs has involved their soot formation behavior [36,67,68] and shapes [13,19,59,66,69,70]. Little has been published concerning the effects of dilution on the lengths of IDFs. Two experimental studies [59,60] found the L_{st} for IDFs to increase when nitrogen was added to the oxidizer, and Lee et al. [58] found it to increase with fuel stream dilution. All three studies involved a small range of dilution.

The analytical model of Roper [10,20] has been used to predict L_{st} of NDFs [11,16,69] and IDFs [19,59,69] with various burner geometries and fuels. Although these have been generally successful, no attempt has been made to apply the Roper model to NDFs and IDFs across a wide range of dilution conditions.

In this study, the L_{st} of normal and inverse steady laminar gas jet diffusion flames are measured. The fuels are methane and propane and the inert is nitrogen. A wide range of dilution is considered for both the fuel and the oxidizer. The Roper model is extended to these conditions, allowing for proper consideration of gas properties, and the results are compared with the measurements.

3.2 Experimental

Tests were performed using a co-flow burner and chimney, as shown in Fig. 3- 1a. The burner's inner port was stainless steel with an inside diameter of 2.9 mm, an outside diameter of 4.2 mm, and a blunt tip. The outer tube was brass with a diameter of 102 mm and its flow was conditioned with a ceramic honeycomb. The glass chimney was 155 mm long with an inside diameter of 100 mm. The top of the chimney was sealed with aluminum foil with a 15 mm round hole on axis. Ignition was

accomplished with a NiCr wire, which was withdrawn after ignition. For IDFs, a secondary flame was ignited above the chimney, as shown in Fig. 3-1b, to eliminate unburned fuel. This flame had no effect on the primary flame inside the chimney.

The gases were CH_4 (99.99%), C_3H_8 (99.5%), O_2 (99.994%), and N_2 (99.998%). Ambient conditions were 1.01 bar and 25 °C. The gas flow rates were controlled with

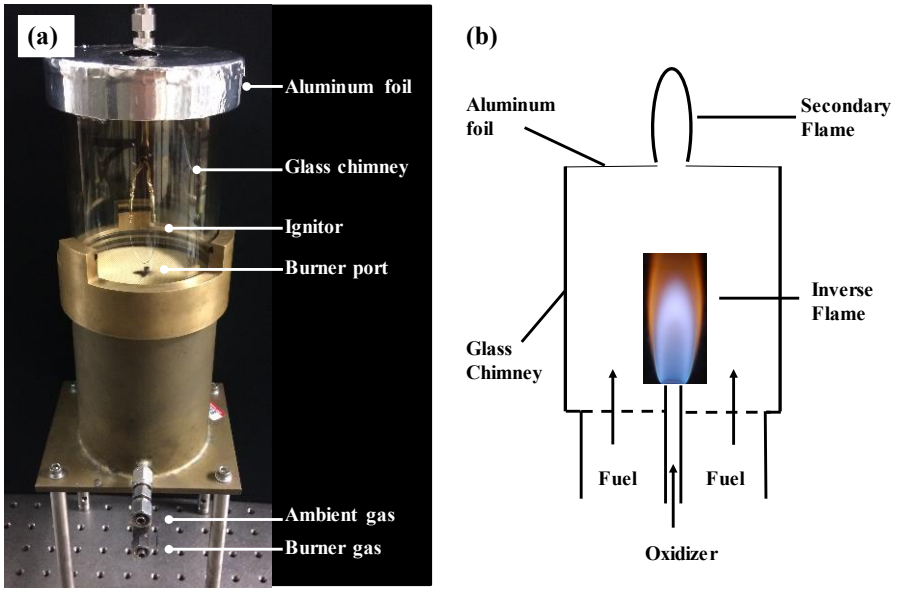

Figure 3-1 (a) Color image of the test apparatus. (b) Schematic of the IDF tests.

metering valves and measured with calibrated rotameters (See Fig.3-2). Uncertainties in the flow rates are estimated at ± 5%. The reactant and nitrogen flow rates were varied as widely as possible. Such variation was limited by flames shorter than 6 mm, flames whose tips approached the top of the chimney, flames that were lifted more than 1 mm, flames that flickered, and flames with too much soot to reasonably identify where the blue flame zone crosses the flame axis. The ambient reactant flow rate was maintained at a minimum of five times stoichiometric and the flame height was found to be independent of outer port gas flow rate.

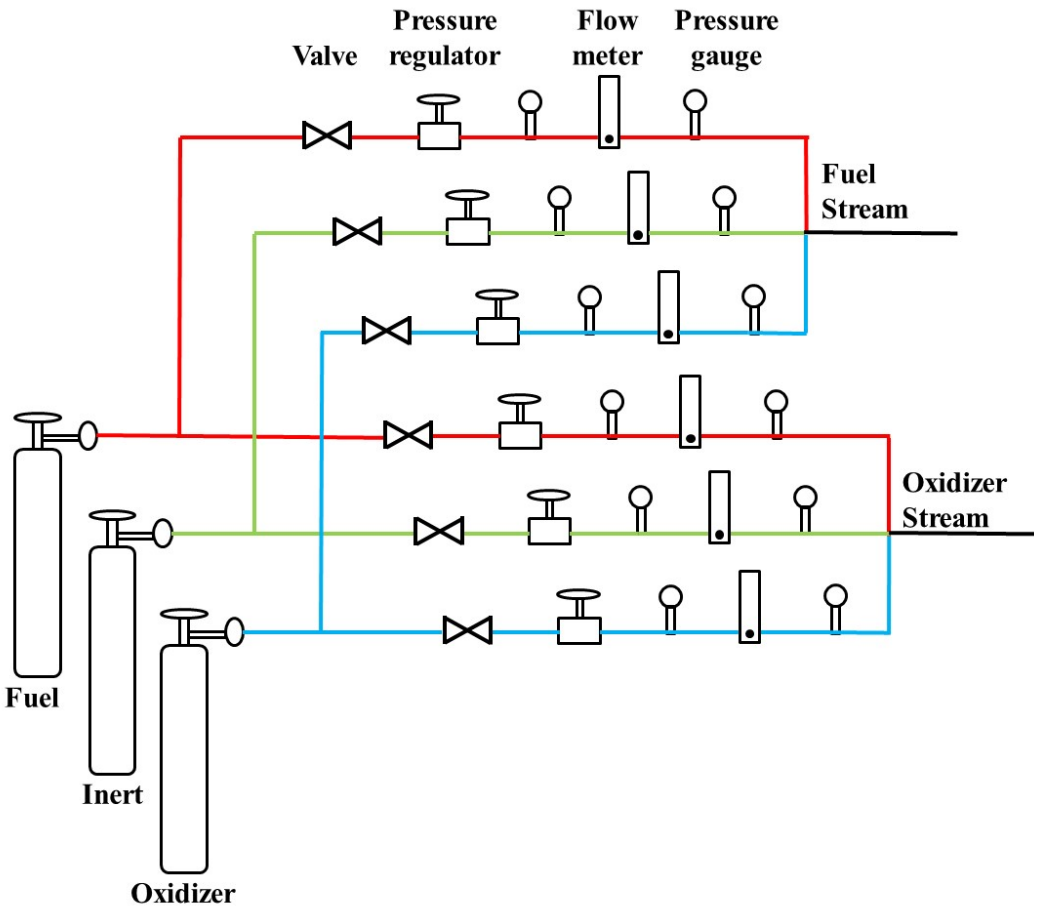

Figure 3-2: Schematic of the flow system.

The flames were imaged with a digital color camera (Nikon D100). Shutter times (0.66 – 300 ms) were selected such that the brightest region in each image was slightly below saturation. The front of the lens was 40 cm from the flame axis and the optical axis was 50 mm above the burner port. To avoid gamma corrections, flame images were saved in uncompressed Nikon-specific format, and converted to tif format by Dcraw. With the exceptions of "– 4" and "– T," only default settings were used. ImageJ was used to obtain the red, green, and blue intensities, from which grayscales were calculated as their average. Stoichiometric flame lengths were defined as the height above the burner tip of the highest grayscale intensity along the axis [16,19]. This

agreed with visual determinations based on the center of the blue flame zone. Uncertainties in the measured L_{st} are estimated at ± 10%. Several flames were imaged with a CH filter in front of the camera, but this complicated differentiating between blue and yellow emissions.

3.3 Analytical

Roper [10] developed an analytical model of mixture fraction distribution in steady laminar gas jet diffusion flames. His key assumptions were those of: equidiffusion of momentum, heat and mass (Sc = Le = 1); negligible axial diffusion; constant temperature and diffusivity near the reaction zone; and equal moles of reactants and products. This model predicts that the stoichiometric length of a diffusion flame on a circular burner is given by

$$L_{st,Roper} / Q = [\, 4 \pi D_o \ln (1 + 1 / S) \,]^{-1} (T_o / T_f)^{0.67} , \qquad (3\text{-}1)$$

where D_o is the characteristic diffusivity of the gas mixture at ambient temperature T_0; Q is the volumetric flow rate of the inner port gas (at ambient conditions); S is the ratio of the volume of outer gas to the volume of inner gas for stoichiometric combustion; and T_f is the characteristic temperature for mass diffusion. As examples, methane NDFs and IDFs have $S = 2\, X_{CH4} / X_{O2}$ and the inverse of this, where X is the reactant mole fraction in the supply stream.

Roper et al. [20] calibrated Eq. (3-1) using measured lengths of approximately 64 NDFs burning various fuels, nearly all of them in air. These lengths were determined from measurements of CO and soot concentrations, which may not accurately represent stoichiometric flame lengths. This calibration yielded T_f = 1500 K and D_o = 20 mm^2/s (which is the binary diffusivity of O_2 into N_2 at 293 K).

Figure 3-3 illustrates the effects of inert addition on the L_{st} predicted by Eq. (3- 1) for methane NDFs and IDFs. These plots include Q_{CH4} and Q_{O2}, defined as $Q_{CH4} = Q\,X_{CH4}$ and $Q_{O2} = Q\,X_{O2}$. As shown in Fig. 3-3, Roper's theory predicts that L_{st} increases with inert addition to the burner and/or outer port gas for both NDFs and IDFs. However, this effect is small for high reactant mole fraction. For example, a methane/air NDF will have a small length increase when the fuel is diluted (at constant methane flow rate) and a large length increase when the air is diluted. As shown by Ref. [16], the trends seen in Fig. 3-3 are also predicted by the analytical models of Altenkirch, Spalding, and Villermaux. These trends are counter to past claims that inert addition to the fuel streams has a negligible effect on stoichiometric flame length [5,62]. These studies involved fuel mole fractions of 0.4 – 1, which may have been too high for a significant effect (see Fig. 3-3).

The above values for T_f and D_0 do not fully account for changes that occur when the reactants, diluents, or dilution levels change significantly. Thus the Roper model is extended here by considering more robust definitions of T_f and D_0. For this it is assumed that the characteristic diffusivity in gas jet diffusion flames is that of reactants (here O_2 and CH_4 or C_3H_8) into the stoichiometric products (here H_2O, CO_2, and N_2). The mass diffusivity of reactant k into the product mixture is [71]:

$$D_{k-prods} = \frac{1 - X_k}{\sum_{j=1}^{3} X_j / D_{k-j}}\ , \tag{3-2}$$

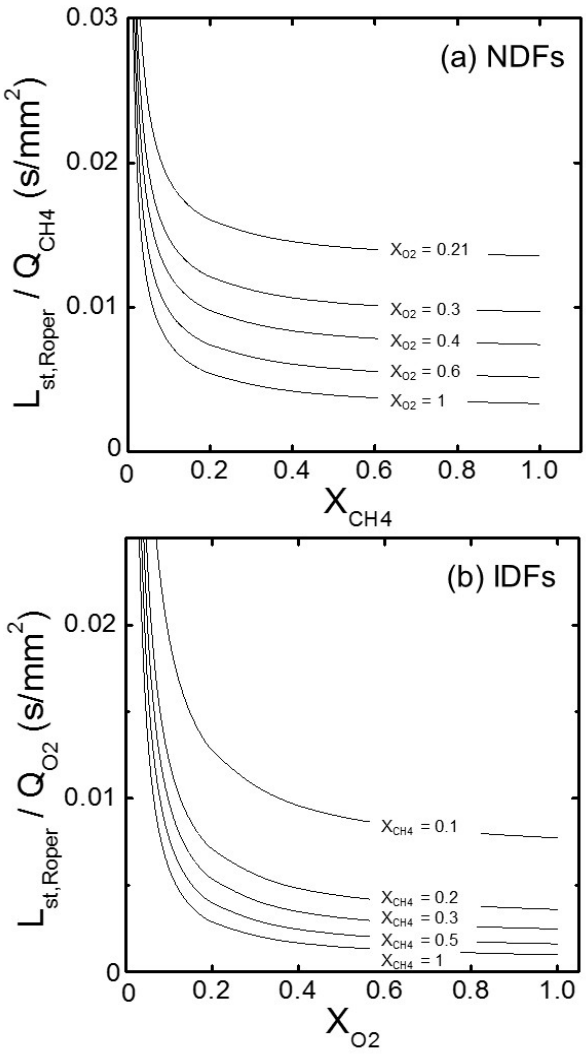

Figure 3-3: Stoichiometric flame lengths for methane predicted by the Roper model, Eq. (3-1), in terms of burner reactant mole fraction for (a) NDFs and (b) IDFs. For these plots T_f = 1500 K, T_0 = 293 K, and D_0 = 20 mm^2/s.

where D_{k-j} is the binary diffusivity of species k and j. The individual binary diffusivities are shown in Table 3-1.

Table 3-1: Binary gas diffusivity D_{k-j} (mm^2/s) of species k into species j at 1.01 bar and 298 K, found from the Lennard-Jones potential equation using the gas properties of Reid et al. [72].

		Species j		
		N_2	CO_2	H_2O
Species k	CH_4	21.9	16.6	14.9
	C_3H_8	11.3	8.0	9.7
	O_2	20.4	15.2	21.0

It is further assumed that the fuel and oxidizer contribute equally to the characteristic mass diffusivity, i.e.,

$$D_0 = 0.5 \left(D_{\text{fuel–prods}} + D_{\text{O2–prods}} \right) , \tag{3-3}$$

This differs from previous studies of NDF lengths where either fuel diffusivity [18,57] or oxidizer diffusivity [20] was assumed to control L_{st}.

Following past work [19,69], the characteristic temperature for mass diffusion in diffusion flames is assumed to be

$$T_f = T_0 + \alpha \left(T_{ad} - T_0 \right) , \tag{3-4}$$

where T_{ad} is adiabatic flame temperature and α is an empirical factor to be found below. This is the only calibration factor in this extension of the Roper model.

3.4 Result and Discussion

Figure 3-4 shows representative images of an NDF and an IDF. The NDF has a thin blue flame sheet surrounded by blue haze and has no visible soot. The IDF has a much thicker blue stoichiometric contour and yellow soot is visible outside and above

this. RGB and greyscale intensity profiles along the axis are plotted. For each flame, the four profiles reach their peaks at the same height where the flame length is defined.

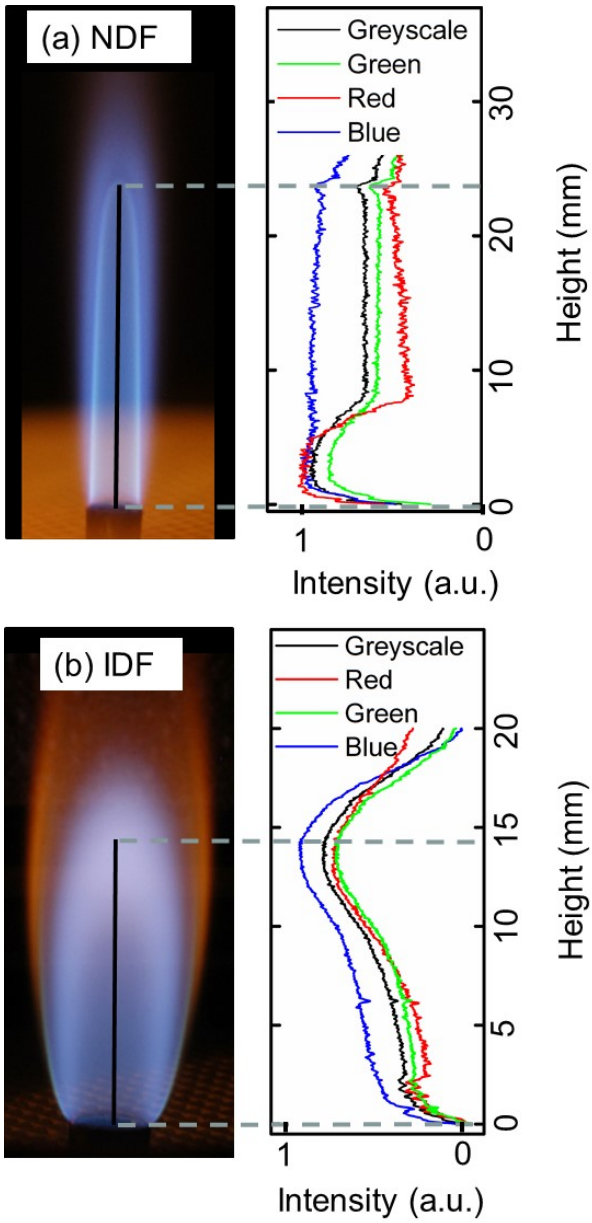

Figure 3-4: Representative methane flame images and intensity profiles, in arbitrary units. (a) An NDF with $\dot{m}_{CH4}$ = 2.93 mg/s, X_{O2} = 1, and X_{CH4} = 0.23. (b) An IDF with $\dot{m}_{O2}$ = 6.77 mg/s, X_{CH4} = 0.29, and X_{O2} = 0.82.

Figure 3-5 demonstrates the effects of nitrogen addition to the inert port gas. Figure 3-5a shows a sequence of representative NDFs with constant methane mass flow

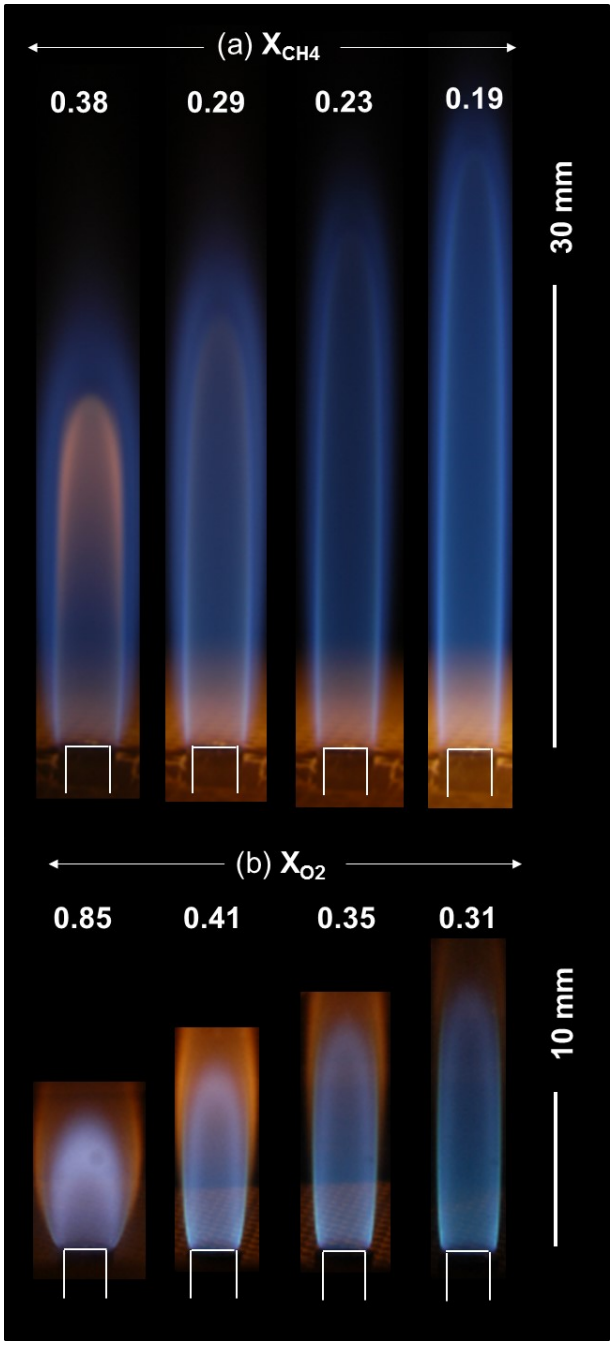

Figure 3-5: Color images of representative methane diffusion flames. (a) shows NDFs ($\dot{m}_{CH4}$ = 2.97 mg/s and X_{O2} = 0.5) and (b) shows IDFs ($\dot{m}_{O2}$ = 6.77 mg/s and X_{CH4} = 0.48).

rate ($\dot{m}_{CH4}$) and X_{O2}. At constant $\dot{m}_{CH4}$, the stoichiometric flame length increases with nitrogen addition to the fuel, in agreement with the observations of McEnally and Pfefferle [22]. Figure 3-5b presents a sequence of representative IDFs with constant $\dot{m}_{O2}$ and X_{CH4}. Again, L_{st} increases with nitrogen addition to the inner gas when the burner reactant flow rate is constant. Consistent with Fig. 3-3, these increases in L_{st} diminish with increasing burner reactant mole fraction.

A total of 174 NDFs and 113 IDFs were observed, as summarized in Fig. 3-6 and Table 3-2. The conditions sought to include the broadest possible range of reactant mole fractions, adiabatic flame temperatures, inner gas flow rates, and measured stoichiometric lengths ($L_{st,meas}$). The propane NDFs have a narrower range of X_{O2} than those of methane, owing to soot interference. Figure 3-6 shows the reactant concentrations for which Refs. [16,22,34] measured L_{st}, and these span a much smaller range.

Parameter α from Eq. (3-4) was optimized by maximizing the coefficient of determination in plots of modeled versus measured L_{st}. Its optimized value was found to be $\alpha = 0.735$, which is within the range of 0.3 – 1 found previously for fuel/air NDFs and IDFs [19,69].

The ranges of D_o and T_f are shown in Table 3-2. For all these flames D_o is lower than the Roper et al. [20] value of 20 mm^2/s, and T_f is higher than their value of 1500 K. For the present test matrix, Q and S are the key factors in predicting L_{st}. This is because they vary much more widely than do D_0 and T_f (see Table 3-2). Thus, at constant burner reactant flow rate, diluent addition increases L_{st} primarily by changing Q and/or S, although T_f and D_o also contribute.

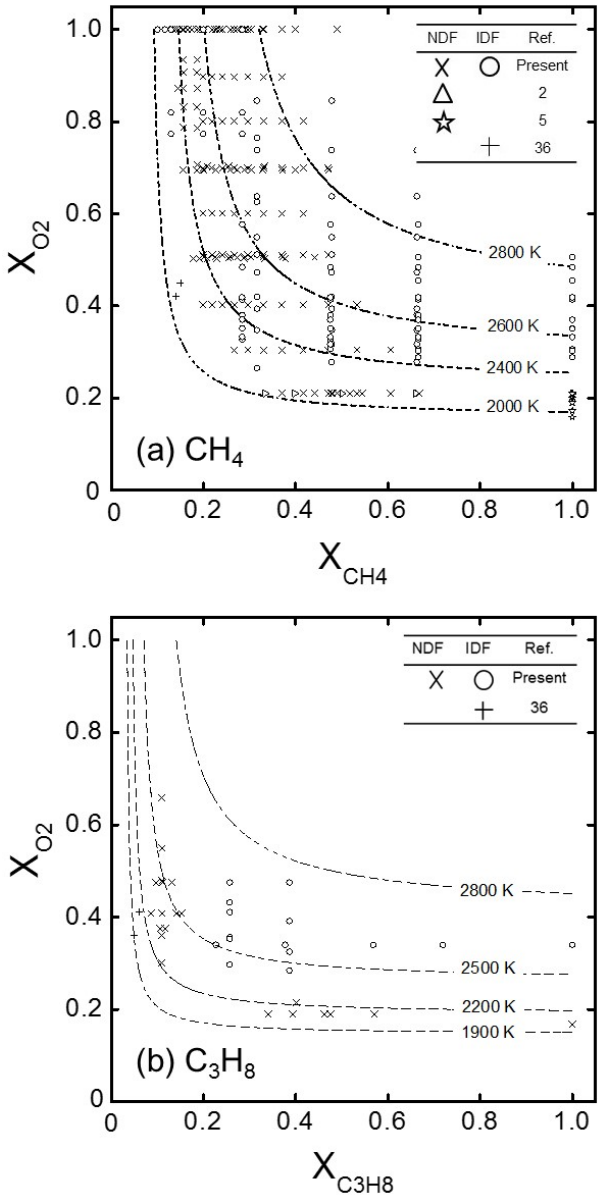

Figure 3-6: Test matrix of (a) methane and (b) propane jet diffusion flames. The dashed curves denote constant T_{ad}.

The measured flame lengths are compared with the extended Roper model predictions in Fig. 3-7. The predictions generally agree with the measurements, with R^2 coefficients of determination of 0.87 and 0.97 for methane and propane. The scatter

Table 3-2: Summary of the test matrix.

	CH_4		C_3H_8	
	NDF	IDF	NDF	IDF
Number of Flames	152	96	22	17
X_{fuel}	0.13 – 1	0.19 – 1	0.08 – 1	0.22 – 1
X_{O2}	0.1 – 1	0.26 – 1	0.16 – 0.66	0.28 – 0.48
S	0.27 – 10.58	0.14 – 4.99	0.83 – 28.98	0.06 – 0.36
D_0 (mm^2/s)	17.87 – 19.87	17.98 – 19.85	13.25 – 14.93	12.73 – 15.00
T_f (K)	1587 – 2227	1605 – 2212	1563 – 1990	1733 – 2085
T_{ad} (K)	2050 – 2920	2080 – 2900	2019 – 2600	2257 – 2753
$\dot{m}_{bur}$ (mg/s)	0.35 – 4.39	4.02 – 9.01	0.46 – 4.57	3.62 – 6.05
$L_{st,meas}$ (mm)	6.4 – 60.9	6.02 – 45	11.3 – 64.1	6.1 – 16.3

in these plots is attributed to experimental error and the assumptions made by the Roper model.

The original model of Roper et al. [20] (predicated on T_f = 1500 K, T_0 = 293 K, and D_0 = 20 mm^2/s) yields correlations with R^2 of 0.83 and 0.85 for methane and propane (Figure 3-8). This difference is small for methane, which was the fuel used most in the Roper et al. [20] tests, but is significant for propane. Evidently the original Roper model is valid for methane NDFs and IDFs with nitrogen dilution, but the extended model is more robust for fuels like propane with diffusivities different from methane's.

The extended Roper model predicts stoichiometric lengths best when the fuel and oxygen mole fractions are between 0.3 – 0.7, but it overestimates (and underestimates) lengths at higher (and lower) reactant mole fractions. Consistent with this, the measurements of Ref. [11,16,22,34] are above the fits in Fig. 3-7 and those of Ref. [19] are generally below the fit. These trends arise because the Roper model does not

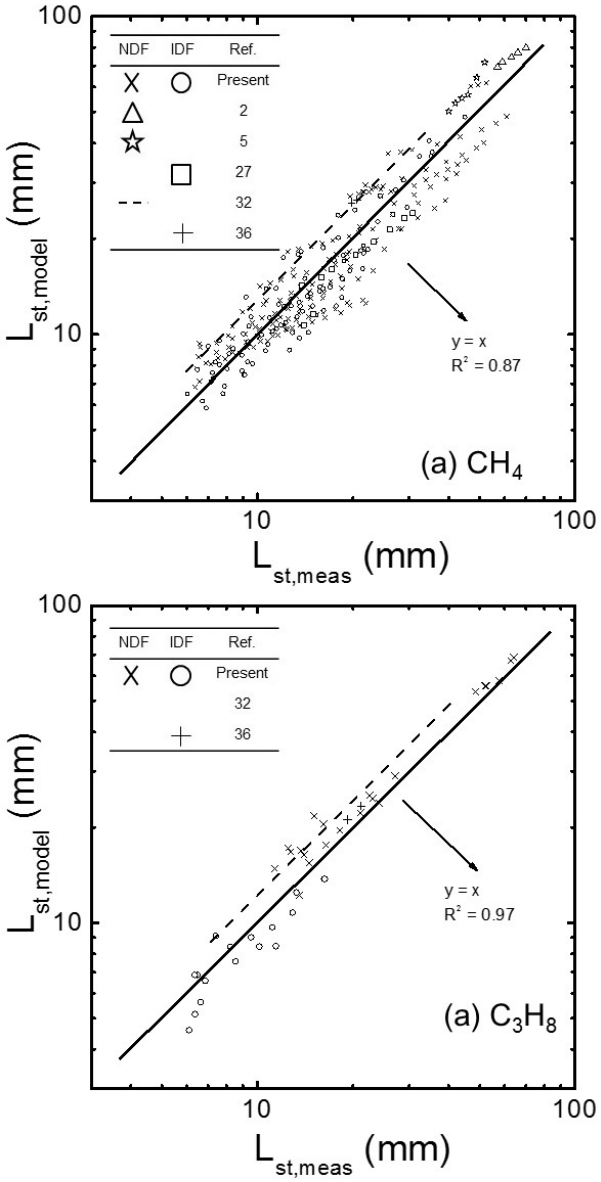

Figure 3-7: Flame length measurements compared to the extended Roper model predictions for (a) methane and (b) propane. Previous results are also shown, but are not included in the determinations of R^2.

account for radiative losses (e.g., by decreasing T_f), which generally increase with increasing reactant mole fractions.

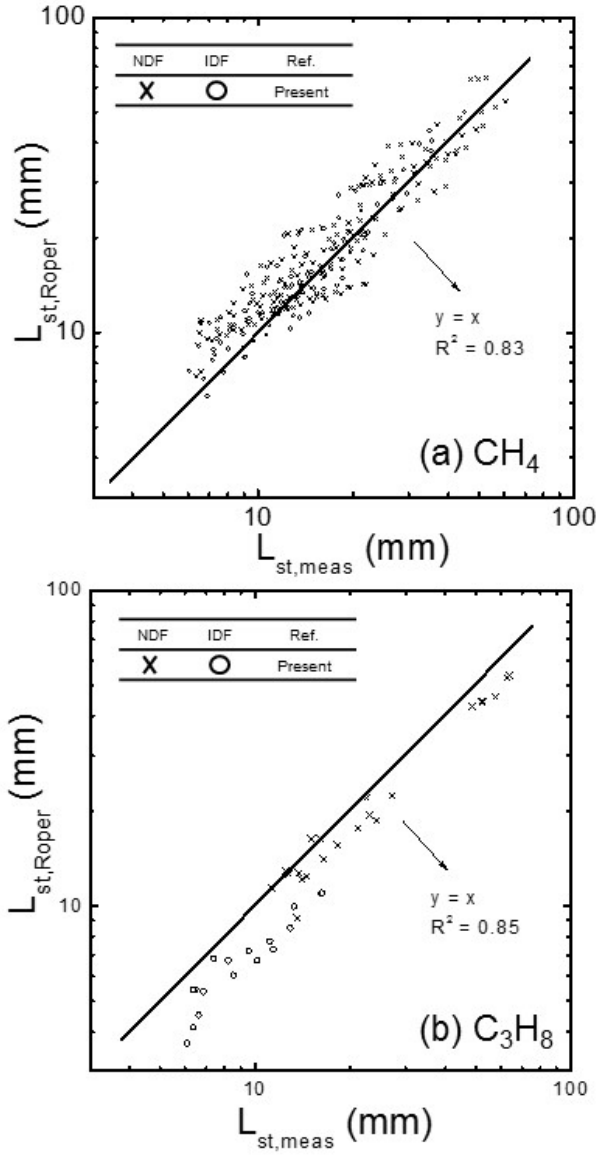

Figure 3-8: Flame length measurements compared to the Roper model predictions without extension for (a) methane and (b) propane.

The measured flame length is not, but closed to the flame stoichiometric length. This will make the measurement and empirical parameter inaccurate, but the prediction will still agree with the measurement.

3.5 Conclusion

The stoichiometric lengths of 174 normal and 113 inverse jet diffusion flames were measured. The ranges of conditions were as wide as possible, and far wider than in past work. Reactant dilution increased the stoichiometric lengths of both NDFs and IDFs when burner reactant flow rate was constant, although this effect was small for high reactant mole fractions. This counters past assertions that inert addition to the burner reactant has a negligible effect on flame length.

The analytical model of Roper for stoichiometric flame length predictions was found to hold for normal and inverse diffusion flames over a wide range of conditions. An improved property model is proposed to improve generality and accuracy, especially for fuels with diffusivities different from methane's. The characteristic diffusivity of the gas mixture was taken to be the average diffusivity of the fuel and oxygen into the stoichiometric products. The characteristic temperature was set empirically to 0.735 times the adiabatic temperature plus 0.265 times the ambient temperature, which is the only calibration factor used in the model. The extended Roper model reproduces the measured lengths reasonably well.

Chapter 4 : Double Blue Zones in Inverse and Normal Laminar Jet Diffusion Flames

4.1 Introduction

As discussed in Chapter 1, previous experimental and computational work indicates that double blue zones are possible for various flame conditions. These blue zones are easily missed; indeed, few past studies mentioned them [13,43-47].

Studies from NDFs [43-47] attributed the zone toward the fuel to hydrocarbon oxidation and the zone toward the oxidizer to CO and/or H_2 oxidation.

The double blue zones in IDFs and NDFs may arise because the products and intermediates in diffusion flames do not have coincident peak concentrations. In methane-air NDFs, the concentrations of H_2, C_2, and CO were found to peak on the rich side of stoichiometric, whereas CO_2, OH, and temperature peaked on the lean side [23,73]. In a methane-air IDF, Wu and Essenhigh [21] found the locations of peak H_2, CO, and CO_2 were consistent with those identified by Refs. [23,73].

Where luminosity from soot and soot precursors can be ruled out, the double blue zones can be attributed to chemiluminescence from excited-state C_2^*, CO_2^* CH^*, and OH^*, which produce most of the visible chemiluminescence in hydrocarbon flames [55]. Most past measurements of flame chemiluminescence were in premixed flames, for which chemiluminescence from these species peaked near the flame front [52-56]. Past studies of flame chemiluminescence in diffusion flames were either obstructed by soot [51] or had inadequate spatial resolution [53,74,75] to resolve possible double blue zones.

Despite the above past work, much remains unknown about double blue zones in diffusion flames. For monocomponent fuels, it is unknown how the zones may correspond with the stoichiometric region or with peaks in species concentrations. To address this, the double blue zones in both NDFs and IDFs are examined here. The effects of fuel type, burner diameter, burner material, diluent type, and reactant dilution level on the double blue zones in diffusion flames are examined. Flame chemiluminescence from C_2^*, CO_2^* CH^*, and OH^* is investigated using filtered images and image deconvolution. The results contribute to an improved fundamental understanding of diffusion flame structure and insight into the visual identification of the stoichiometric zone and various species peaks in IDFs and NDFs.

4.2 Experimental

Diffusion flames were observed using a co-flow burner. The burner set up and flow system is presented in Section 3.2. The reactants were CH_4 (99.99%), C_3H_8 (99.5%) and O_2 (99.994%) and the diluents were Ar (99.999%), CO_2 (99.999%), He (99.999%), and N_2 (99.998%). For some tests, partially premixed fuel and oxidizer was supplied to the inner and/or outer ports. All the flames were laminar and steady.

Figure 4-1 is the imaging system schematic. A digital color camera was used for color imaging and to image C_2^*, CO_2^* and CH^*. This was a Nikon D100 charged-couple device (CCD) digital camera with 6 megapixels and a 60 mm AF Micro-Nikkor lens. The *ISO* (International Organization for Standardization) setting was 200, the f-number (*f*) was 2.8, and the exposure time, *t*, varied between 0.003 – 30 s such that images were

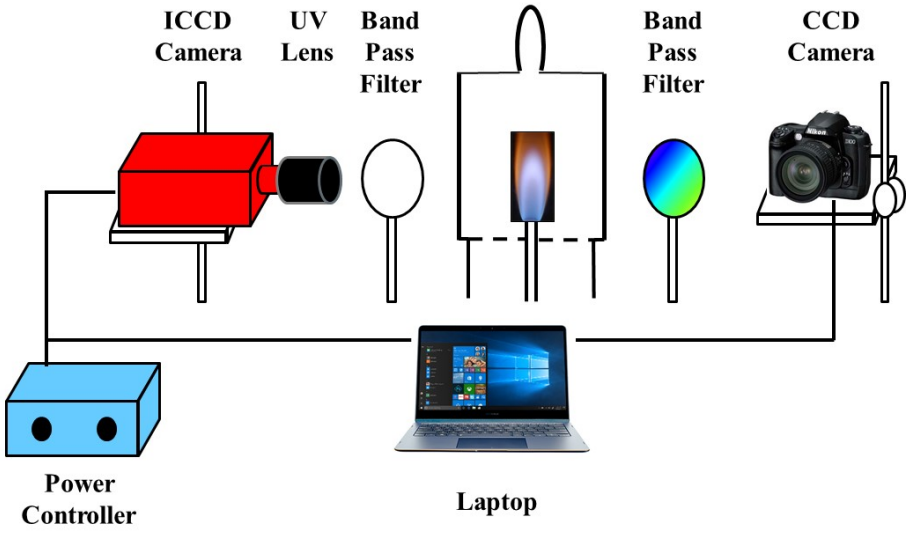

Figure 4-1: Schematic of the imaging system.

bright but without saturation at any pixel in any color plane. The white balance was direct sunlight, but this had no effect because the images were recorded in raw format. The front of the lens was 15 cm from the flame axis and its optical axis was 50 mm above the inner port. The pixel spacing in the object plane was 10 μm.

CCD images were recorded in raw format and converted to 3 × 16 bit tif format using Dcraw (with default settings except –4 and –T) to avoid gamma corrections [76]. For each pixel the red, green, and blue pixel values (I_R, I_G, and I_B) were extracted with MATLAB's imread and im2double functions. The dark-current pixel values, I_{DC}, were small (below 0.004 in each color plane) and had negligible variation with shutter time.

An ultra-violet (UV) camera was used to image OH^* emissions. This was an intensified charge-coupled device (ICCD) camera (XYBION Electronic System, ISG-250-GQU3) with 0.4 megapixels and a 105 mm Nikkor UV lens. This camera is sensitive to 180 – 900 nm. The intensifier gain was 2.5 V, f was 4.5, and t was 33 ms such that images were bright but without saturation at any pixel. The front of the lens

was 40 cm from the flame axis and its optical axis was 50 mm above the inner port. The pixel spacing in the object plane was 17 μm.

The UV video output was recorded at 30 frames/s to mp4 video using Elgato video capture. Still grayscale images, in 8 bit tif format, were obtained using VLC media player. For each pixel the grayscale pixel values (I_{ICCD}) were extracted with MATLAB's imread and im2double functions. The dark-current pixel values were negligible.

A 50 mm round bandpass filter was placed in front of the CCD or ICCD camera lens for most images. Four such filters were paired with the cameras as shown in Table 4-1. The filters for OH^*, CH^*, and C_2^* match chemiluminescence peaks for these species, while the filter for CO_2^* is in a region of broadband CO_2^* emissions [51-56].

Grayscale pixel values for the CCD camera were defined as

$$I_{GS} = (I_R + I_G + I_B) / 3 , \tag{4-1}$$

where I is pixel value. For both cameras normalized pixel values were defined as

$$NI_i = (I_i - I_{i,DC}) f^2 / t , \tag{4-2}$$

where DC is dark current and i denotes the camera and the color plane.

Table 4-1: The bandpass filter wavelengths and transmittances, the associated species, the cameras used, and parameters α, β and γ. The filters are bandpass filters from Andover Corp. and have *FWHM*s of 10 nm.

Filter central λ (nm)	Filter peak τ	Species	Camera(s) used	α	β	γ
310	0.15	OH^*	ICCD	0.33	0.67	0.24
430	0.46	CH^*	CCD	1	0.89	0.73
455	0.63	CO_2^*	ICCD & CCD	1	1	1
515	0.65	C_2^*	CCD	0.67	0.75	1.03

A blackbody furnace (Oriel 67032) was used to calibrate both cameras when paired with various bandpass filters. The blackbody had a 25 mm aperture diameter, a temperature of T = 1000 °C a temperature accuracy of ± 0.2 °C, and an emissivity of $\varepsilon = 0.99 \pm 0.01$. This emissivity in the visible was confirmed for a similar blackbody [77]. For the CCD and ICCD cameras, the lens distance was 15 and 40 cm, respectively, and it was focused on the aperture. For each CCD (and ICCD) image, a 200 × 200 (and 100 × 100) pixel region centered on the aperture was considered, which corresponded to about 1% (and 8%) of the aperture.

Figure 4-2: Blackbody furnace (Oriel 67032).

The pixel sensitivity associated with each camera, lens, and bandpass filter is defined as

$$S_i(\lambda) = NI_i / [\, \varepsilon\, E_b(\lambda, T)\, \tau(\lambda)\, FWHM \,], \qquad (4\text{-}3)$$

where ε and T are the blackbody emissivity and temperature, λ, τ and $FWHM$ are the bandpass filter's central wavelength, peak transmittance, and full-width at half maximum (see Table 4-1), and E_b is the spectral emissive power of an ideal blackbody,

$$E_b(\lambda, T) = C_1 / \{\, \lambda^5 [\, \exp(C_2 / \lambda T) - 1 \,] \,\}, \qquad (4\text{-}4)$$

where C_1, and C_2 are the first and second radiation constants (3.742×10^{-4} W-m^2 and 1.439×10^4 μm/K).

Figure 4-3 summarizes the pixel sensitivities for each paring of camera and filter shown in Table 4-1. For the CCD camera this is consistent with past calibrations of similar CCD and complementary metal-oxide-semiconductor (CMOS) cameras [78,79]. Although the R, G, and B sensitivities vary with wavelength, the GS sensitivity is relatively constant.

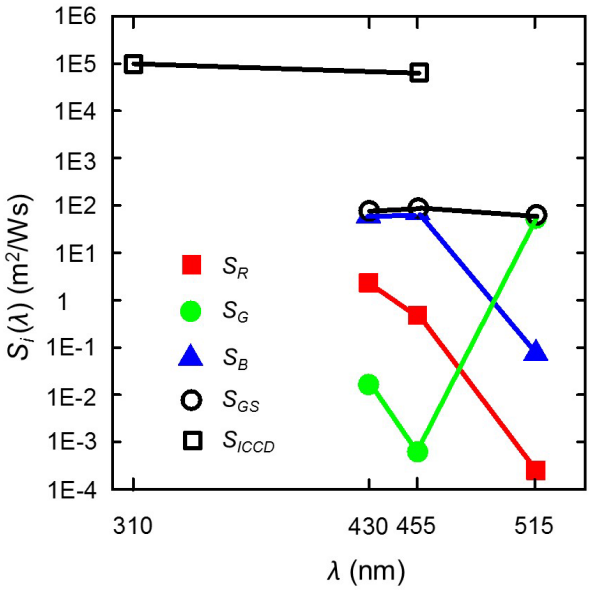

Figure 4-3: Sensitivities of the CCD and ICCD pixels.

For the ICCD the sensitivity was measured at 455 nm and estimated at 310 nm using this measurement and the camera specifications because the blackbody emissions at 310 nm were too dim to be measured. This UV lens has relatively flat transmittance between 310 and 455 nm.

Compared to the CCD, the ICCD has a higher sensitivity owing to its intensifier array. At 455 nm the CCD GS signal-to-noise ratio (the pixel value mean divided by its standard deviation) is 64, compared 25 for the ICCD.

Image deconvolution was performed because line-of-sight images can complicate image interpretation. Deconvolution has been used widely to obtain properties such as soot temperature and soot volume fraction in axisymmetric flames [76,80] and more recently has yielded deconvolved flame images [51,52]. Onion peeling deconvolution was used here, for which the local property per unit length is the product of the projected property and a reconstruction matrix [80-83].

The deconvolution was performed separately on the NI_R, NI_G, and NI_B for the unfiltered images, and NI_{GS} for the filtered images. These values were found from Eqs. (4-1) and (4-2).

For both the filtered and unfiltered images, NI_i was smoothed in the horizontal direction using the Savitski-Golay filter function in MATLAB [81]. Parameters framelen=51 and order=1 were specified, as they were found to suppress noise with minimal distortion of the intensity peaks. The flame images were split on the flame axis, deconvolved separately, and recombined.

For the filtered images from the CCD camera, the initial colors were approximately reproduced using

$$\mathrm{D}\,(NI_i) = \mathrm{D}\,(NI_{GS})\, S_i \,/\, S_{GS}\ , \tag{4-5}$$

where D is the deconvolution operator and i denotes R, G, or B.

The deconvolved results were converted to image files by scaling the values linearly to a range of 0-1 and then applying the MATLAB imshow function.

Details about the onion peeling deconvolution method and its corresponding MATLAB code are provided in Appendix A and Appendix C.

Extensive soot formation was avoided with diluents. However CO_2^*, like soot, has broad luminous emissions in the visible and UV [52-56]. To correct for this, images of CO_2^* emissions at 455 nm were used to estimate and subtract the contribution of CO_2^* emissions at 310, 430, and 515 nm. For both cameras, following deconvolution the correction applied at each pixel was

$$\mathrm{D}\left(NI_{GS,\lambda,corr}\right) = \mathrm{D}\left(NI_{GS,\lambda}\right) - \alpha_\lambda \beta_\lambda \gamma_\lambda \mathrm{D}\left(NI_{GS,455\ \mathrm{nm}}\right), \qquad (4\text{-}6)$$

where corr denotes the correction for CO_2^* emissions. Parameters α, β, and γ are, respectively, the ratios of CO_2^* intensity, pixel sensitivity, and τ at wavelength λ divided by that at 455 nm. Parameter α comes from the measurements of Refs. [52,54,56] for methane-air diffusion flames, β comes from Fig. 4-3, and γ comes from the τ shown in Table 4-1. The MATLAB code for CO_2^* broadband emissions correction are provided in Appendix D

At each pixel, the deconvolved spectral emissive power (E) for the species OH^*, CH^*, and C_2^* at their chemiluminescence peaks was found from

$$\mathrm{D}\left[E(\lambda)\right] = \mathrm{D}\left(NI_{GS,corr,\lambda}\right) / \left[S_{GS}(\lambda)\,\tau(\lambda)\,FWHM\right], \qquad (4\text{-}7)$$

while for CO_2^* quantity $NI_{GS,\lambda}$ replaced $NI_{GS,corr,\lambda}$.

4.3 Results

The double blue zones were more prominent for IDFs than for NDFs, and for Ar than for the other diluents. Figure 4-4a shows an image of a representative Ar diluted methane IDF recorded by the CCD camera without a bandpass filter. Three main features are visible in this flame: orange emissions from soot high in the flame, a broad inner blue zone that is closed on the flame axis, and an outer, thinner, blue-green zone that is open on the flame axis. The inner and outer zones are named here double blue

zones and are identified with arrows in Fig. 4-4. The zones are closest low in the flame and diverge with increasing height. At the height where the inner zone closes on the axis, the outer zone is at a radius of 1.6 mm.

A white rectangle is shown in Fig. 4-4a. Quantity NI_{GS} was found for each pixel in this rectangle and averaged in the vertical direction. The results are plotted in Fig. 4- 4a and reveal that the inner blue zone is broad, the outer blue zone is narrow and brighter, and the soot region is outside the outer blue zone.

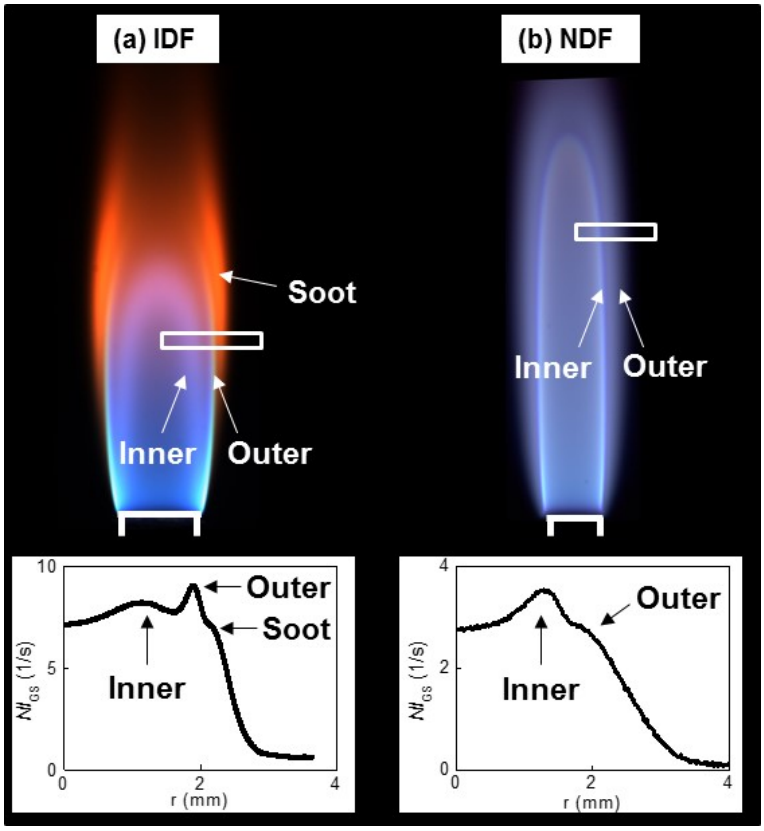

Figure 4-4: Unfiltered CCD images of a representative Ar-diluted methane (a) IDF and (b) NDF. The IDF and NDF have flow rates of $\dot{m}_{O2}$ = 5.2 mg/s and $\dot{m}_{CH4}$ = 1.63 mg/s, methane mole fractions of X_{CH4} = 0.41 and 0.19, and oxygen mole fractions of X_{O2} = 0.34 and 0.32, respectively. The burner diameter is 2.7 mm.

Figure 4-4b shows an image of a representative NDF. This flame also has double blue zones. Its inner zone is thin and blue-green. Its outer zone is thicker and blue. Here again the zones diverge with increasing height. Both zones are closed on the flame axis, where they are separated by 0.9 mm. Quantity NI_{GS} is also plotted for a region in this flame. This indicates that the inner zone is narrower and brighter than the outer zone is.

The blue zones in the IDF and NDF of Fig. 4-4 have several common features. The blue zone toward the fuel side is narrower, brighter, and blue-green, while that toward the oxidizer side is broader and dimmer. They also have some differences: in the IDF the double zones are more prominent and the outer zone is open on the flame axis.

Over 100 IDFs and NDFs with little or no soot were observed with various fuels (CH_4, C_3H_8), diluents (Ar, N_2, CO_2), stoichiometric mixture fractions (0.14 – 0.8), adiabatic flame temperatures (2052 – 2922 K), stoichiometric flame lengths (6 – 61 mm), and burner diameters (3 and 15 mm). All the flames exhibited double blue zones.

Figures 4-5a and 4-5b show representative images of CH_4 and C_3H_8 IDFs with 3 mm inner port burner. Figure 4-5c is a CH_4 IDF in a 15 mm inner port burner. Double blue zones are observed in all of these three flames.

Most flames in this study are tested by a stainless steel burner. Flames burned with a copper and a glass burner are shown in Figure 4-6. The flame color depends

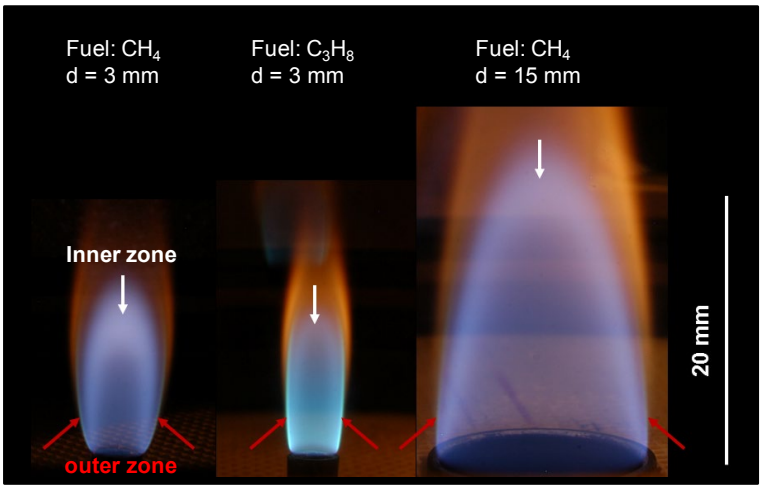

Figure 4-6: Color images of (a) CH_4 IDF with 3 mm burner diameter; (b) C_3H_8 IDF with 3 mm burner diameter; (c) CH_4 IDF with 14 mm burner diameter. Red (and white) arrows point to the outer (and inner) blue zones.

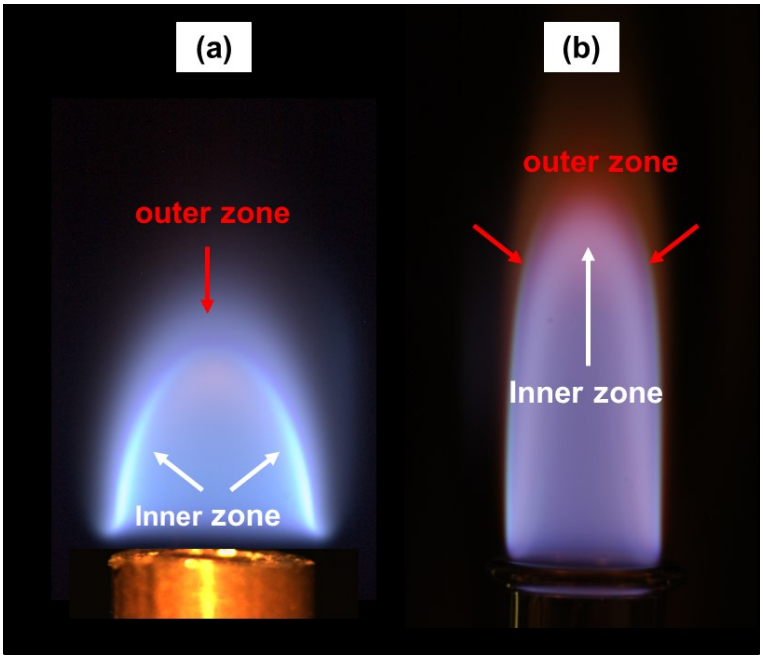

Figure 4-5: Color images of (a) CH_4 NDF with 4 mm (inner diameter) copper burner; (b) CH_4 IDF with 5 mm (inner diameter) glass burner. Red (and white) arrows point to the outer (and inner) blue zones

slightly on the burner material. For example, the flame supported by the glass burner looks more yellow. The double blue zones structure remains for both NDF and IDF

with various burner materials.

Methane IDFs diluted by He, Ar and CO_2 are compared in Figure 4-7. All of three flames present double blue zones structure**.** Compare with He and Ar, the outer zone of CO_2 diluted flame is weak.

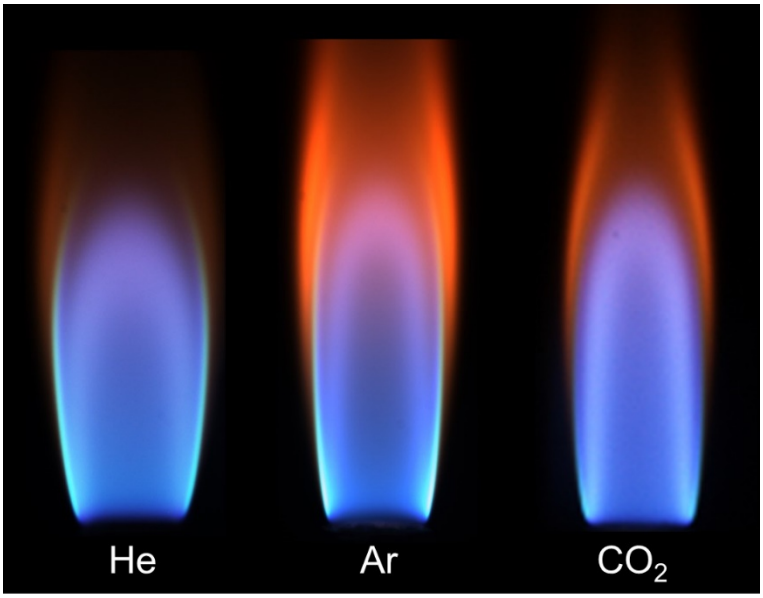

Figure 4-7: Color images of CH_4 IDFs with He, Ar and CO_2 as reactant diluents.

Reactant dilution changes the stoichiometric mixture fractions (Z_{st}) and the adiabatic flame temperature (T_{ad}). The effect of Z_{st} and T_{ad} on the double blue zones of CH_4 IDFs were discovered. Figure 4-8 lists a sequence of IDFs with constant Z_{st}. The T_{ad} of the IDF was decreased from 2712 to 2413 K by adding N_2 to both fuel and oxidizer streams. The double blue zones are observed in all of these flames. The luminosities for both inner and outer zones are decreased as both fuel stream and oxidizer stream dilution. The luminosity reduction of inner zone is higher as it has more dilution.

In comparison, Fig. 4-9 presents a sequence of IDFs with constant T_{ad}. Quantity Z_{st} is decreased from 0.73 to 0.2 by moving the N_2 dilution from fuel stream to oxidizer

stream. Double blue zones are observed in all four flames. The luminosity of the outer zone is increased as Z_{st} decreases.

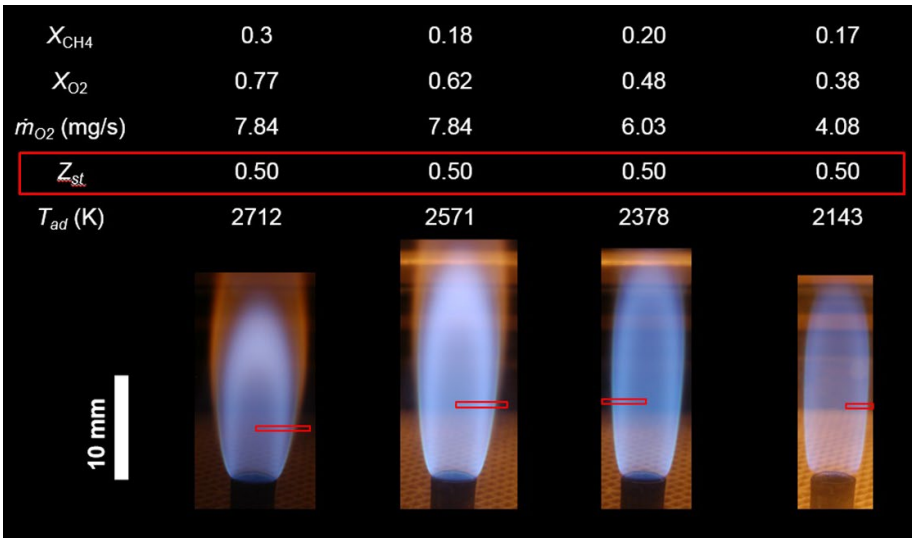

Figure 4-8: A sequence of CH_4 IDFs with constant Z_{st}. T_{ad} was decreased from 2700 K to 2100K.

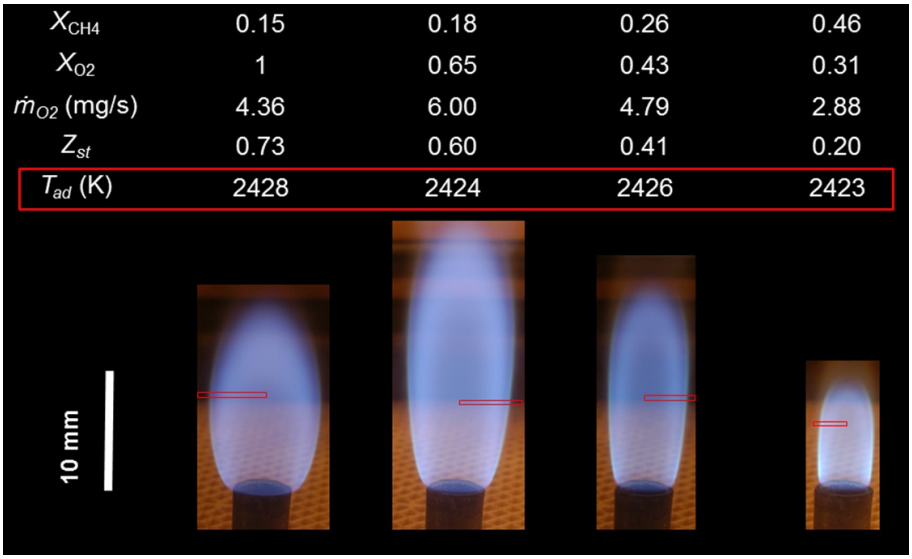

Figure 4-9: A sequence of CH_4 IDFs with constant T_{ad}. Z_{st} was decreased from 0.73 to 0.20.

Partially premixed flames can help identify whether the blue zones are lean, stoichiometric, or rich. Figure 4-10a shows a N_2 diluted methane IDF. When oxygen was added to the fuel, Fig. 4-10b, no new blue zone appeared. Because this outer gas is richer than stoichiometric (see Table 4-2), the inner and outer blue zones in Fig. 10b

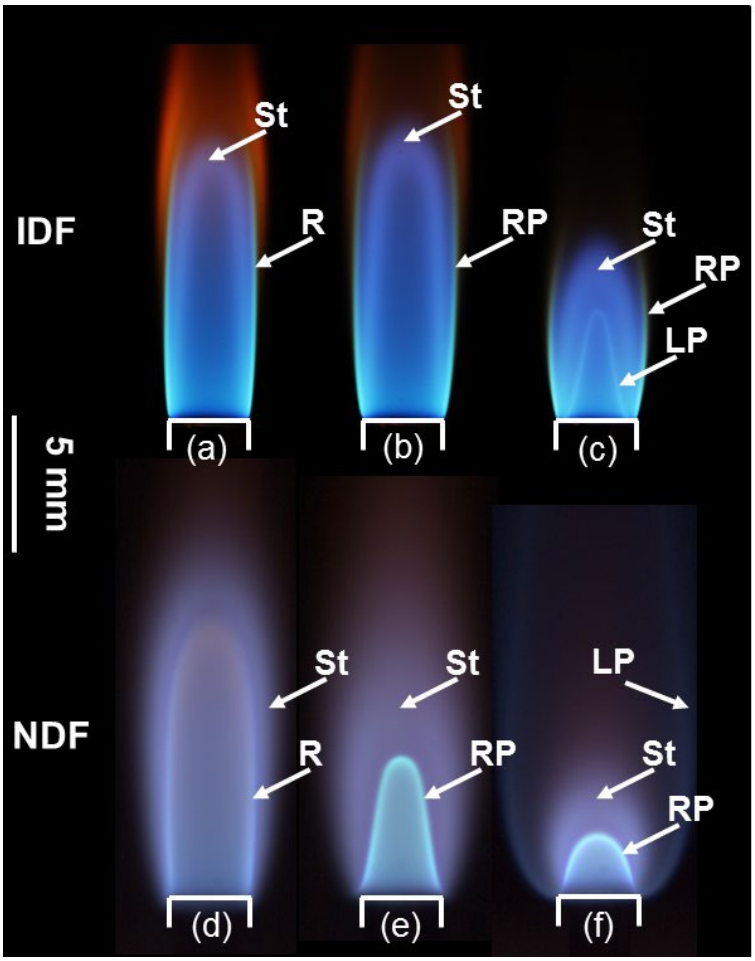

Figure 4-10: Unfiltered CCD images of diffusion flames and partially premixed flames. (a) An IDF, to which (b) O_2 is added to the outer gas, to which (c) CH_4 is added to the inner gas. (d) A NDF, to which (e) O_2 is added to the inner gas, to which (f) CH_4 is added to the outer gas. These blue zones are indicated with arrows: LP (lean premixed), R (rich), RP (rich premixed), and St (stoichiometric).

Table 4-2: Conditions for the flames of figure 4-10.

Flame	Inner gas			Outer gas		
	$\dot{m}$ mg/s	X_{CH4}	X_{O2}	$\dot{m}$ mg/s	X_{CH4}	X_{O2}
a	6.06	-	0.32	52	0.67	-
b	6.06	-	0.32	52	0.60	0.11
c	6.06	0.07	0.30	52	0.60	0.11
d	1.26	0.28	-	35.2	-	0.45
e	1.26	0.19	0.22	35.2	-	0.45
f	0.41	0.26	0.21	35.2	0.04	0.23

are expected to be stoichiometric and rich premixed, respectively. When, additionally, methane was added to the oxidizer, Fig. 4-10c, a third blue zone appeared inside the others with the shape of a premixed Bunsen burner flame. Because the inner gas is leaner than stoichiometric (see Table 4-2), this must be a lean premixed zone. These images indicate that the double blue zones of IDFs involve an inner stoichiometric zone and an outer rich zone. Additional support for this comes from OH planar laser-induced fluorescence measurements of methane and ethylene IDFs [19,60], which found the stoichiometric regions to correspond with what we identify in their flame images to be the inner zones of IDFs.

Figure 4-10d shows a N_2 diluted methane NDF. When oxygen was added to the fuel, Fig. 4-10e, the inner zone became blue-green with the shape of a premixed Bunsen burner flame, but no new blue zone appeared. Because the burner reactant is richer than stoichiometric (see Table 4-2), the inner and outer blue zones in Fig. 4-10e are expected to be a rich premixed flame and a stoichiometric diffusion flame, respectively. This finding is supported by similar tests performed by [39,84]. When, additionally, methane

was added to the oxidizer stream, Fig. 4-10f, a new blue zone appeared outside the others. Because the oxidizer is leaner than stoichiometric (see Table 4-2), this zone must be a lean premixed flame. This finding is supported by similar tests performed by [85-87]. These images indicate that the double blue zones of NDFs involve an outer stoichiometric zone and an inner rich zone. Note that most past flame shapes studies assumed the NDF inner zone to be stoichiometric, e.g., Ref. [90].

Figure 4-11 shows filtered and unfiltered images of an IDF and an NDF. The burner tip and centerline are shown in white. To the left and right of each centerline are

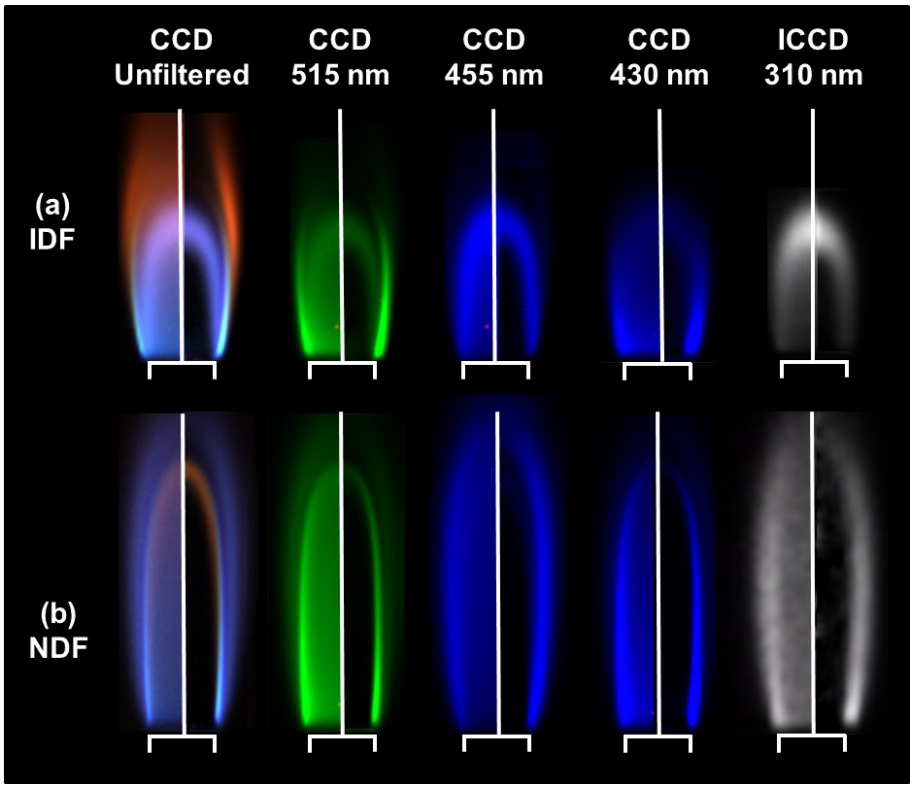

Figure 4-11: Representative methane (a) IDF and (b) NDF images. The IDF and NDF have $\dot{m}_{O2}$ = 4.02 mg/s and $\dot{m}_{CH4}$ = 1.26 mg/s, X_{CH4} = 0.45 and 0.28, and X_{O2} = 0.48 and 0.38, respectively. Images to the right of each centerline are deconvolved. The burner diameter is 2.7 mm.

the initial and deconvolved images. The unfiltered images exhibit double blue zones for both the IDF and the NDF similar to the flames of Fig. 4-4. The deconvolved images have flame features that are slightly wider and have sharper edges than the initial images. Among the filtered images in Fig. 4-11, only the 515 nm images have clear double blue zones (which appear green in this image). The 430 nm images also have double blue zones, but only the one on the rich side is readily visible. The 455 nm and 310 nm images have only a single blue zone, which is stoichiometric.

The $\mathcal{D}$ (NI_{GS}) intensities at 515 nm are presented as color contour plots in Fig. 4- 12, where both sides of the centerline are now shown. The contour plot is created by Tecplot. The peak intensities are higher in the IDF than in the NDF. This is

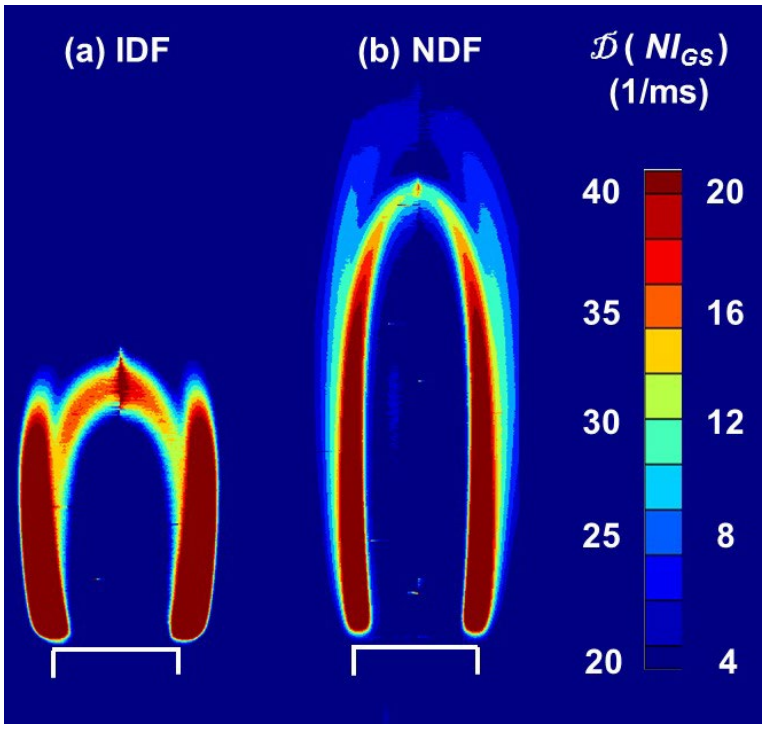

Figure 4-12: Contour plot of deconvolved normalized intensities for the 515 nm filtered CCD images of Fig. 4-11. The values to the left and right of the color bar are for the IDF and NDF, respectively.

because the IDF has higher flame temperature as its X_{CH4} and X_{O2} are higher. In both cases these peaks are higher in the rich zone as in the stoichiometric zone. This is also make sense because the characteristic chemiluminescence species at 515 nm, C_2^*, is formed to the rich side of stoichiometric.

Equation (4-6) allows the subtraction of the expected broadband contribution of CO_2^* from the images filtered at 515, 430, and 310 nm. The results are shown in Fig. 4-13. To the left of each centerline is the deconvolved image of Fig. 4-11, and to right is the image following CO_2^* subtraction. For the images at 515 and 430 nm, the stoichiometric zones disappear. This is reasonable because C_2^* and CH^* are formed to

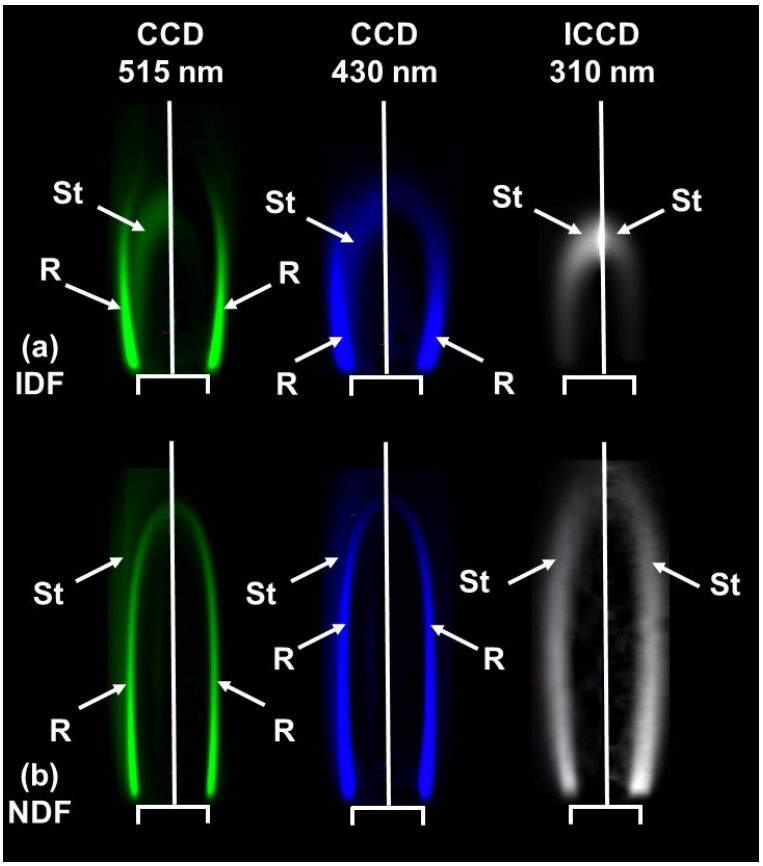

Figure 4-13: Deconvolved images of filtered images before (left of axis) and after (right of axis) CO_2^* subtraction for the flames of Fig. 4-11.

the rich side of stoichiometric. For the image at 310 nm the stoichiometric zone remains following subtraction. This is reasonable because both CO_2^* and OH^* are formed in or near the stoichiometric zone. Thus, for both IDFs and NDFs, emissions from C_2^* and CH^* peak in the rich zone, whereas those from CO_2^* and OH^* peak in the stoichiometric zone.

Figure 4-14 shows the deconvolved spectral emissive power profiles, from Eq. (4-7), for C_2^*, CO_2^*, CH^* and OH^* for representative heights in the flames of Fig. 4- 11. For both flames, the OH^* and CO_2^* emissions have coincident peaks near the stoichiometric zone and C_2^* and CH^* emissions have nearly coincident peaks on the rich side. (The C_2^* peak is about 0.1 mm toward the fuel side as compared to the CH^* peak.) For both flames the highest $\mathcal{D}$ [$E_s(\lambda)$] are for OH^* and CH^* and the lowest is CO_2^*. All the peaks are higher in the IDF than in the NDF owing to higher scalar dissipation rates. The $\mathcal{D}$ (NI_{GS}) for unfiltered CCD images are also shown. These each have two peaks coincident with the other peaks in Fig. 4-14.

Figure 4-15 shows the unfiltered images of Fig. 4-11 after deconvolution, onto which are superimposed the contours of the peak deconvolved spectral emissive power of C_2^*, CO_2^*, CH^* and OH^* at each height. For both flames, the CH^* and C_2^* emissions are aligned with the rich zone, which makes it appear blue-green. For both flames the CO_2^* and OH^* emissions are aligned with the stoichiometric zone. Because OH^* emissions from flames are essentially invisible to the unaided eye, the thick stoichiometric blue zone is primarily the result of CO_2^* emissions.

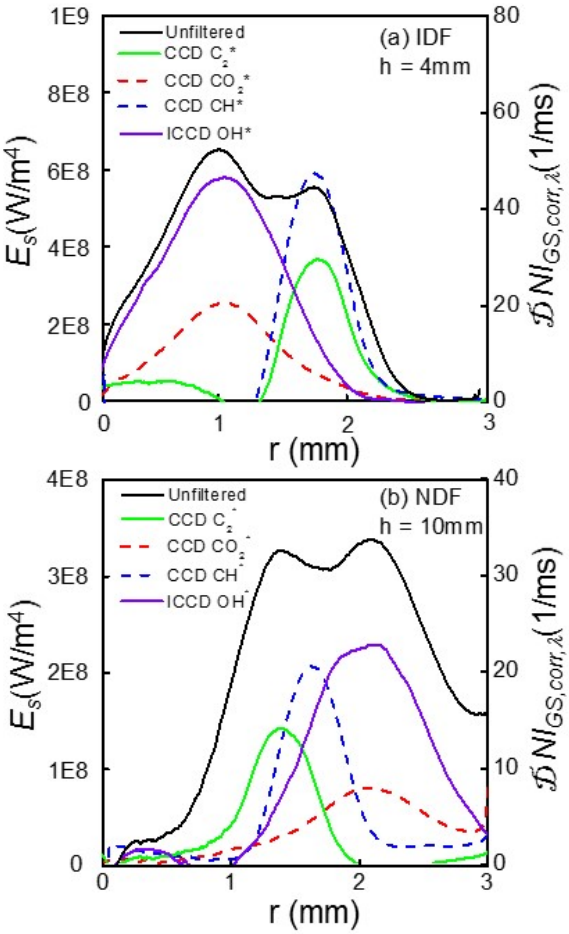

Figure 4-14: Deconvolved spectral emissive power profiles of C_2^*, CO_2^*, CH^* and OH^* along the radial length for (a) the IDF in Fig. 4-11a at a height of 4 mm and (b) the NDF in Fig. 4-11b at a height of 10 mm. The D (NI_{GS}) profile for unfiltered CCD images at same flame height are also plotted.

4.4 Conclusion

Double blue zones in both NDFs and IDFs were observed in over 100 hydrocarbon diffusion flames. The fuel type, reactant type, burner diameter, burner material and reactant dilution level are varied. Chemiluminescence associated with

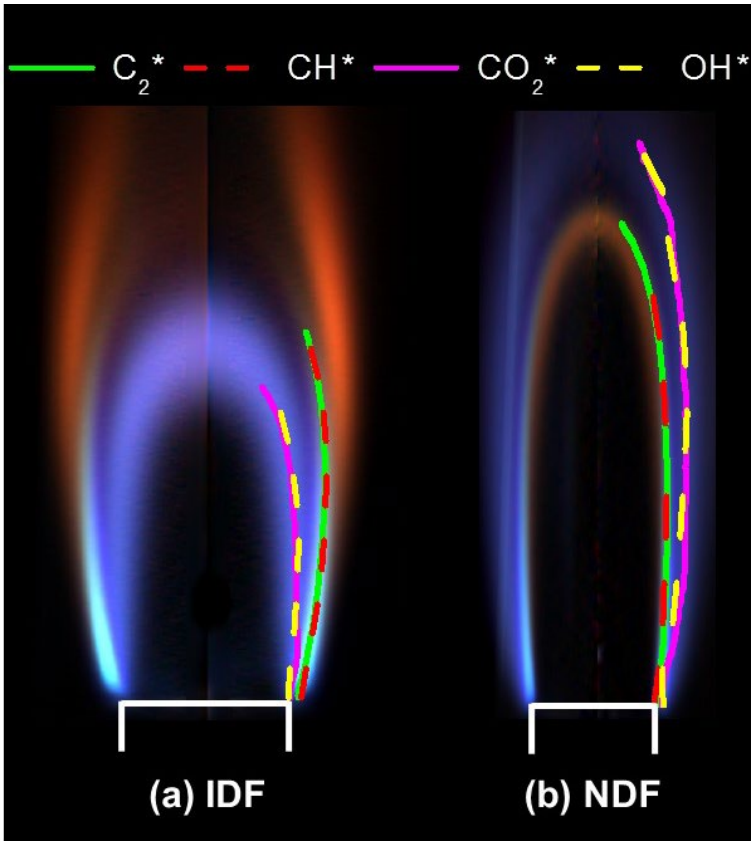

Figure 4-15: The unfiltered images of Fig. 4-11 after deconvolution. Dashed lines are contours of peak D [$E_s(\lambda)$] of C_2^*, CO_2^*, CH^* and OH^* at each height.

OH^*, CH^*, CO_2^*, and C_2^* was measured with 10 nm bandpass filters at 310, 430, 455, and 515 nm, respectively. The cameras with filters were calibrated with a blackbody furnace. Images were deconvolved by onion peeling and broadband CO_2^* emission was subtracted. The major conclusions are as follows.

1) Double blue zones are observed in non-sooty NDFs and IDFs with various conditions: fuel types; burner diameters (3 mm - 14 mm), burner materials (stainless steel, copper, glass), diluents (Ar, CO_2, He, N_2), Z_{st} and T_{ad}. These are more distinct in IDFs than in NDFs. The zones are separated by up to 1.6 mm (and 0.9 mm) at the flame tip for IDFs (and NDFs).

2) For both flame types, the blue zone toward the fuel side is rich and blue-green, while that toward the oxidizer side is stoichiometric, blue, and thicker.

3) For both flame types, the 515 nm and 430 nm images have double blue zones after deconvolution. The D (NI_{GS}) peak intensity of 515 nm is higher in rich zone (and IDF) than that in stoichiometric zone (and NDF). Their stoichiometric zones are disappeared following CO_2^* emission subtraction. The 455 nm and 310 nm images only have stoichiometric zones after deconvolution, and the zones remain following CO_2^* emission subtraction.

4) The rich zone results from emissions from CH^* and C_2^*. The stoichiometric zone results from CO_2^* emissions and is coincident with the peak in OH^*. All the deconvolved spectral emissive power peaks are higher in the IDF than in the NDF owing to higher scalar dissipation rates.

Chapter 5 : Temperature Measurement of Normal and Inverse Co-flow Diffusion Flames

5.1 Introduction

Chapter 4 found that the double blue zones in laminar diffusion flames consist of a rich zone and a stoichiometric zone. The rich zone results from emissions from CH^* and C_2^*. The stoichiometric zone results from CO_2^* emissions and is coincident with the peak in OH^*. However, the temperatures associated with these double blue zone are unknown.

In hydrocarbon diffusion flames the temperatures and major species (such as H_2, C_2, CO, and CO_2,) have been measured [21,23,73]. However, none of these studies provided sufficient spatial resolution to resolve the 0.7 mm separation between the double blue zones. Measuring these temperatures will aid the understanding of flame shapes, major species, stoichiometry location, and the local reactions. In this chapter, fine B-type thermocouples are used to measure the temperatures of both normal and inverse diffusion flames.

5.2 Experimental

B type thermocouples are used here because the adiabatic temperature of the flames of interest exceeds 2000 K. Because the separation between the double blue zones is about 1 mm, it is estimated that the thermocouple wires should be thinner than 50 μm to resolve the temperatures. In this work, B type thermocouple wires in standard grade (Platinum 6% Rhodium T/C Wire and Platinum 30% Rhodium T/C Wire) are purchased from Johnson Matthey. Thermocouple wires are welded by both acetylene oxygen torch flame and an arc welder (Omega, TL-WELD). The acetylene oxygen

torch flame weld equipment (Smith Equipment) includes an Acetylene Caddy (23- 1004A), a magnetic torch stand, welding goggles, and welding gloves. The Acetylene Caddy includes a torch (11- 1101C), torch tips (#3-#7), acetylene regulator (30-15-200), oxygen regulator (30-20-540), pair reverse flow check valves (H698), 8' (2.4 m) covered hoses, oxygen cylinder (OC20) and an acetylene cylinder (2329E).

Figure 5-1 shows the thermocouple beads made by these two welding methods. The bead diameters (D_{bead}) are similar, but the bead made with the arc welder is more spherical. Because the arc welder is also easier and faster, it was used for the 8 thermocouples in this study. The D_{bead} of each thermocouple were measured by an

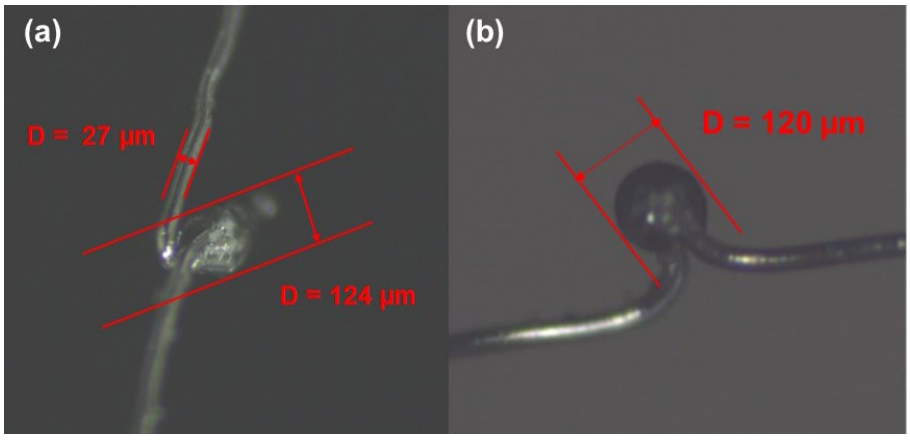

Figure 5-1: Microscope images of B type thermocouples bead welded by (a) an oxy-acetylene torch and (b) an arc welder.

Table 5-1: B type thermocouple number (TC #) and their corresponding D_{bead}.

TC #	1	2	3	4	5	6	7	8
D_{bead} (um)	106	120	104	118	98.2	79.7	137	107

optical microscope (See Table 5-1). These beads are all nearly spherical, but the D_{bead} vary.

Figure 5-2 presents an image of the experimental set up for the flame temperature measurements. Two parallel ceramic insulators are connected with an actuator (ECO- WORTHY, L11TGF12V-2), a potentiometer slide (Bourns) and a thermocouple. The potentiometer and thermocouple are connected to a data acquisition system (DATAQ Instruments, Model DI-245). The burner is the same as that in Chapters 3 and 4. Two 6 mm diameter holes are drilled in the glass chimney wall for flame access by the thermocouples. The hole centers are 12 and 18 mm above the honeycomb. The translation stages are adjusted as the actuator, slide potentiometer, thermocouple and the axis of the hole are at a same horizontal plane. When the actuator

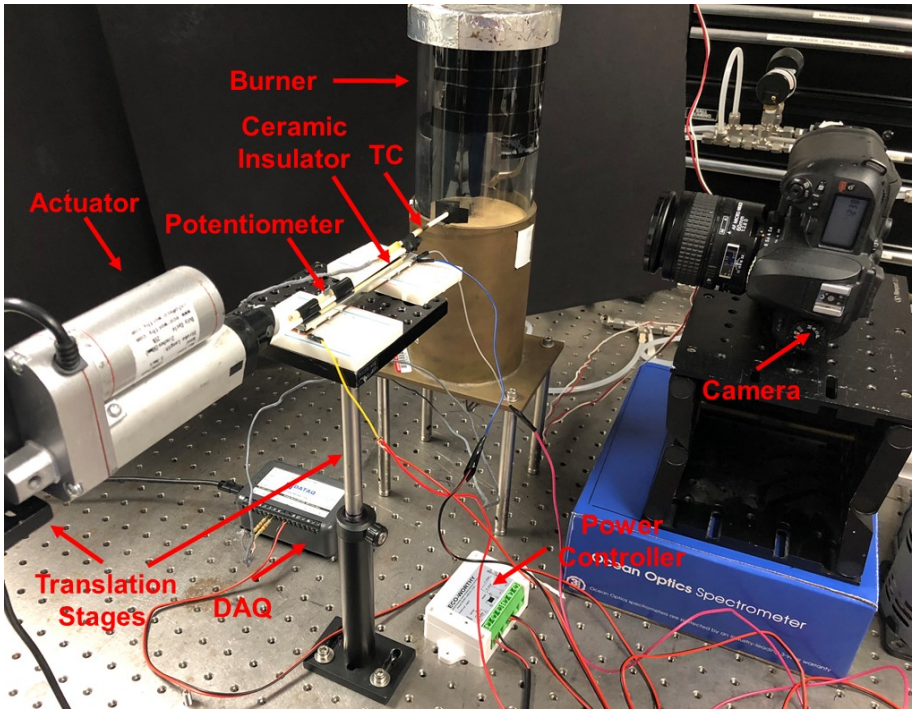

Figure 5-2: Experimental set up for the temperature measurement.

is powered by an external power controller, it translates the ceramic insulators, potentiometer slide and thermocouple forward.

A Nikon D100 SLR camera recorded the thermocouple bead initial location. A digital video camera (Casio EX-F1) recorded the bead motion at 30 frames/s. The front of the lens was 40 cm from the flame axis and its optical axis was 50 mm above the inner port. The video is saved in MOV format.

The actuator and slide potentiometer were calibrated. The actuator was supplied a fixed excitation (V). The actuator travel length (D) during the traveling time (t) are recorded at different V. Results are plotted in Figure 5-3. Quantity V varies from 3.4 – 11.6 VDC. The actuator moves in a constant speed under a fixed V. This speed is more stable when V is in the range of 5 – 10 VDC. In this study, V is 6.4 VDC.

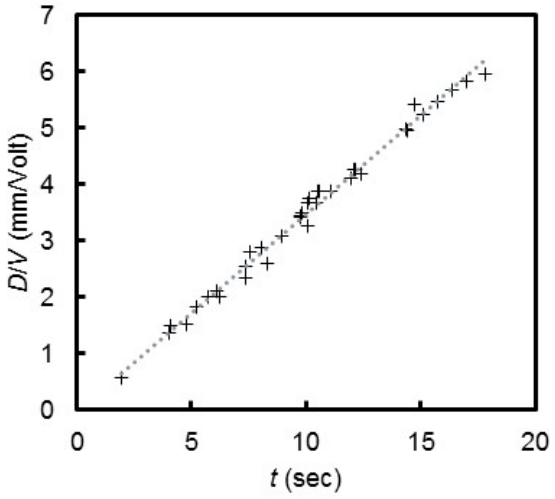

Figure 5-3: Actuator calibration result.

A slide potentiometer was supplied with a constant excitation (5 ± 0.001 VDC) provided by a Laboratory DC Power Supply (TENMA, 72-6615). The slide travelling distance (D) and the corresponding voltage (V_{slide}) presented from data acquisition

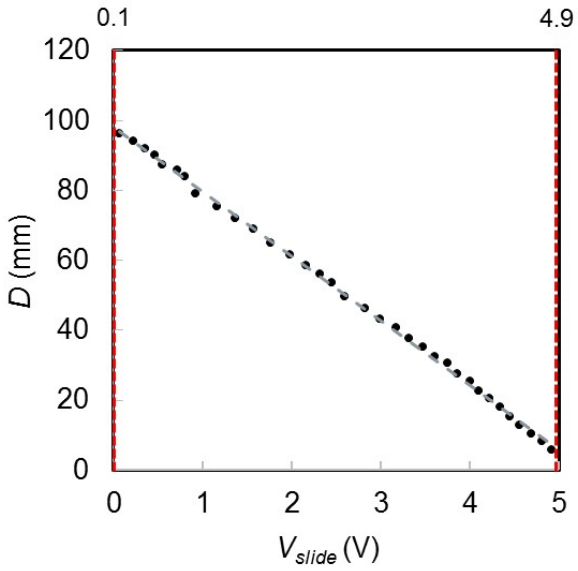

Figure 5-4: Slide potentiometer calibration result under a constant 5 V excitation

(DAQ) are recorded and plotted in Figure 5-4. The V_{slide} decreases as the D increases. The range for the V_{slide} is from 0.1 – 4.9 VDC. The calibrated data are fitted with

$$D = -18.44\ V_{slide} + 98.092, \quad (5\text{-}1)$$

Prior to the temperature measurement, the actuator was powered to push the thermocouple through the flame several times. This ensures that 1) the thermocouple will not be melted in the flame and 2) the thermocouple bead trajectory is as desired.

5.3 Results

Figure 5-5 is an image of a methane–air NDF with N_2 as fuel dilution. A thermocouple bead (TC#2) is observed in Fig. 5-5 as a white circle on the middle left side of the image. This bead is initially located at 8.24 mm (and 18 mm) away from the burner surface plane (and burner axis), as measured by Image J.

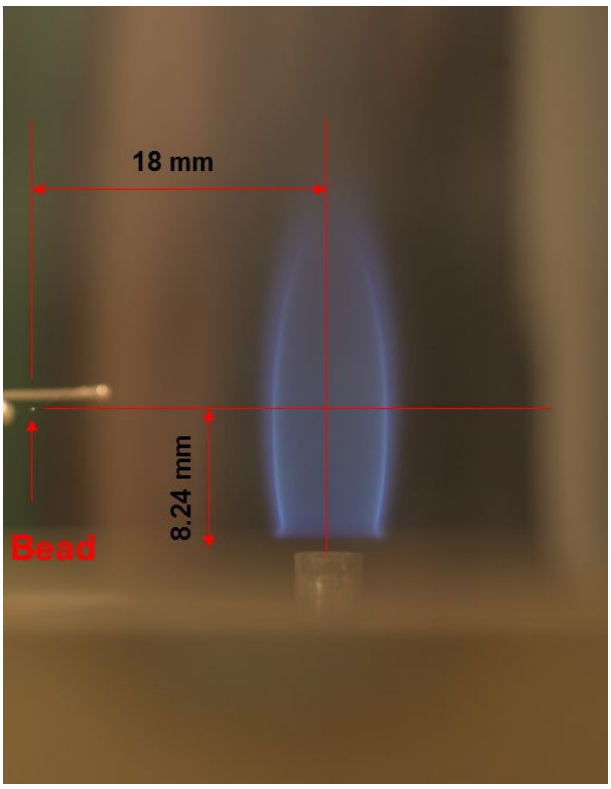

Figure 5-5: Image of a methane – air NDF with $\dot{m}_{CH4}$ = 0.94 mg/s. Fuel stream is diluted by N_2 as X_{CH4} = 0.37 and T_{ad} = 2053 K.

The video is recorded as the thermocouple passes across the flame. Figure 5-6 presents four video screenshots. The axially lengths of thermocouple bead are measured to be the same from Fig. 5-6b to 5-6d. This proves the measured temperature is at the same radial plan across the flame circle diameter.

The measured V_{slide} is converted to slide D by Eq. 5-1, with results are plotted in Fig. 5- 7a. The slide moves at a constant speed. The measured temperature profile is also plotted in Fig. 5- 7b. The measured cut off temperature is 250 ºC. Two temperature peaks are observed. The peak temperature is 1780 K. The temperature at the first peak is 9 K higher than the second one. The temperature increases and decreases smoothly

without any minimum in temperature in the vicinity of the double blue zones (see Fig. 4-4).

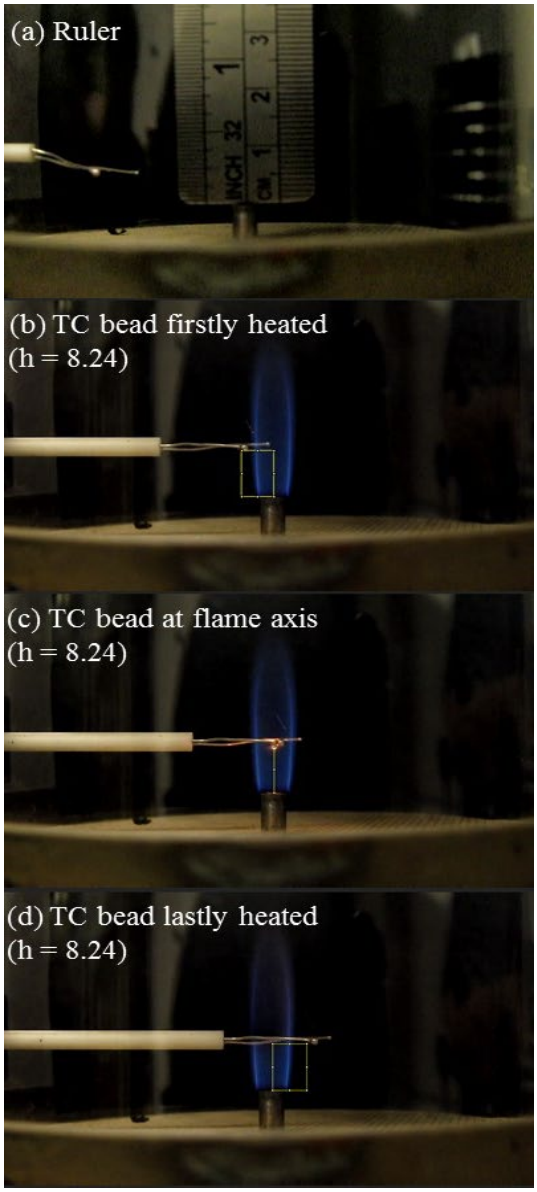

Figure 5-6: Video screenshots of (a) ruler standing on the burner tip, and thermocouple bead (b) first heated and shined by flame, (c) at the flame axis and (d) lastly heated and shined by flame. The corresponding axially height of the bead in Fig 5-6b-d is measured

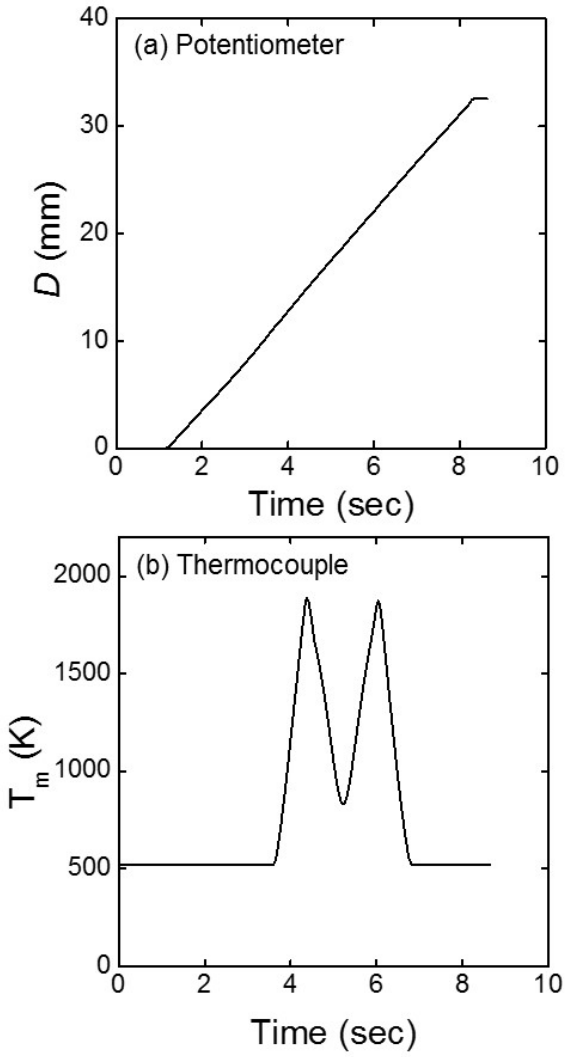

Figure 5-7: Measured results from (a) potentiometer and (b) thermocouple

The potentiometer voltage and flame temperature are recorded by the same DAQ. By combining the Fig. 5-7a and 5-7b, one obtains a relation between thermocouple temperature and slide traveling length, which is also the thermocouple traveling length (See Fig. 5-8).

The thermocouple bead starts to travel from the initial location measured in Fig. 5-5. The traveling length in Fig. 5-8 is converted to flame radial length as presented in Fig. 5-9. The two temperature peaks are symmetric about the flame axis. The peak

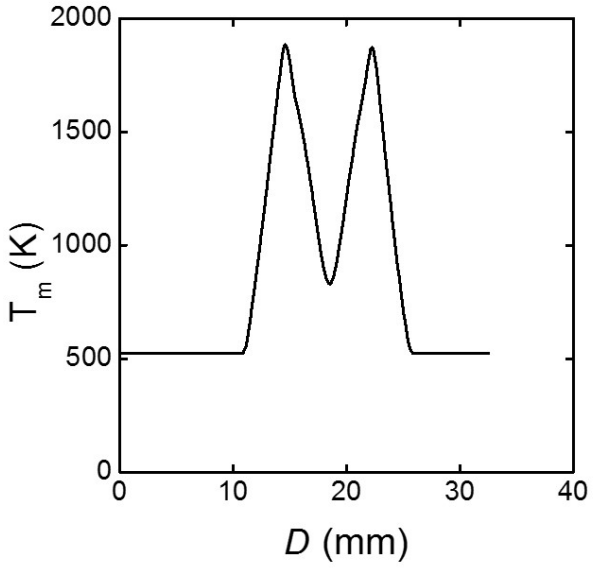

Figure 5-8: Thermocouple measured temperature with respect to its traveling length.

temperatures corresponds to the outer (stoichiometric) zones of this NDF. This agrees with our interpretation of previous measurements [23,73]. The temperature profile does not present any changes between the double blue zones. This could be because the measurement frequency (corresponding to 100 μm per measurement) is too low.

Radiation from the thermocouple is considered in Fig. 5-10. The calculation is detailed in Appendix B. The corrected temperature (ΔT) is small compared with measured temperature (T_m). The temperature corrections do not change the location of the peak temperature.

Temperature measurements for an IDF were also performed. Conditions were sought such that the peak temperatures and gas velocities are relatively low to prevent thermocouple melting. However, velocities that are too low produce flames that are too short (i.e., less than 10 mm). All the IDFs studied here were either too hot or too short.

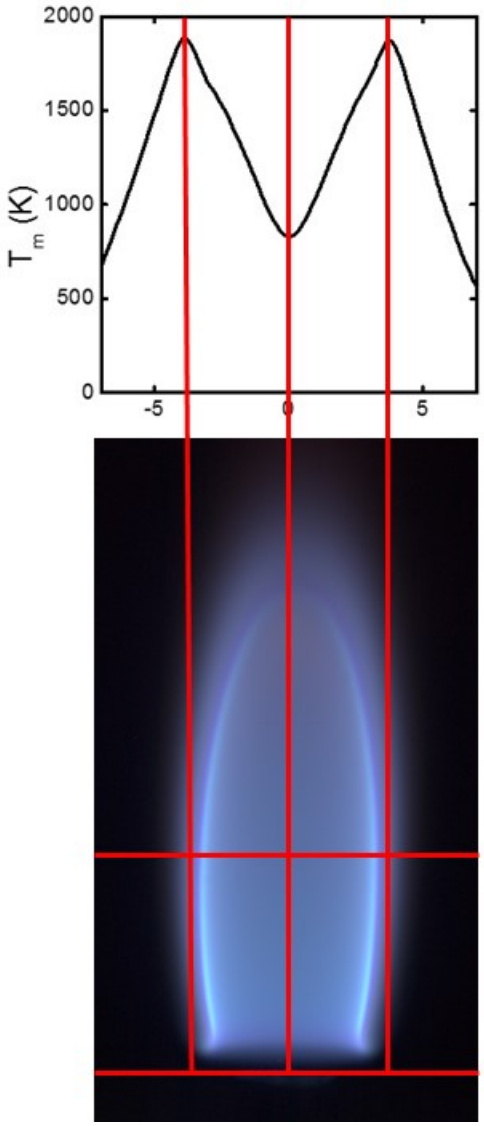

Figure 5-9: An image of the measured NDF with black background. On its top is its measured temperature profile with respect to flame radial length in a unit of mm.

A potential solution is to use a thicker thermocouple wire, but this will reduce the spatial resolution.

Temperature diagnostics other than thermocouples are possible. Thin filament pyrometery (TFP) has long been used in flames. Figure 5-11 presents an image of a

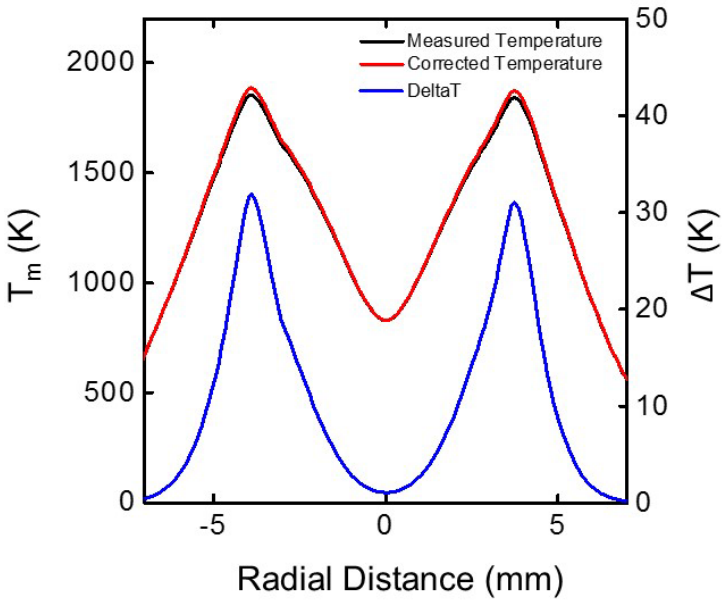

Figure 5-10: Profiles of measured temperature, corrected temperature, and ΔT with respect to flame radial distance.

methane IDF with a superimposed image of a TFP fiber in the same flame. The shutter time for the TFP fiber was reduced to 1/1500 s to avoid saturation. A fiber grayscale profile is plotted, which is a surrogate for gas temperature [91]. The grayscale peaks align with the inner blue zone, indicating that the inner zone is hotter. The TFP resolution is 20 μm, which is better than that of the thermocouple. The results from both thermocouple and TFP support the finding that the temperature peaks at the stoichiometric zone for both NDFs and IDFs.

5.4 Conclusions

B type thermocouples beads were made successfully with an arc welder. An experimental system for temperature measurement was built and calibrated. An NDF was measured by thermocouple and an IDF was measured by TFP. The major conclusions are as follows.

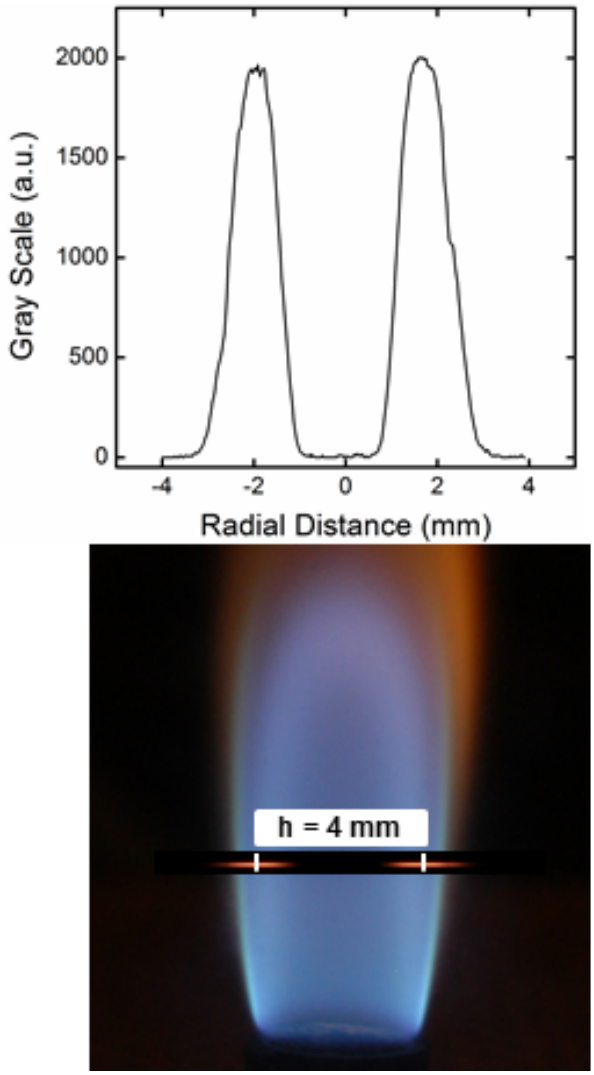

Figure 5-11: Grayscale intensity profile measured by TFP along the radial distance at 4 mm above the burner. The white bar shows the radius of peak temperature. Methane is the fuel. The IDF is in condition of $X_{O2} = 0.38$, $X_{CH4} = 0.6$, and $Z_{st} = 0.184$.

1) The temperature profile of an NDF was measured at a height of 8.25 mm. Two temperature peaks that are symmetric along the flame axis were observed. The peak temperature corresponds to the outer (stoichiometric) zone of the NDF. The peak temperature was 1780 K. The temperature

increases and decreases smoothly without a minimum near the double blue zones.

2) The thermocouple measurements were corrected for radiation. The corrections are small relative to the thermocouple bead temperatures. The location of peak temperature does not change after these corrections.
3) Temperature profiles of an IDF by B-type thermocouple were not possible, as the flames were either too hot or too short. Instead, TFP was used. The TFP peaks aligned with the inner blue zone, indicating that the inner zone is hotter.
4) The result from both thermocouple and TFP support the finding that the temperature peaks at the stoichiometric location for both NDFs and IDFs.

Chapter 6 : Conclusions

In this dissertation, the shapes and the double blue zones of the laminar co-flow jet diffusion flames have been studied for over 300 NDFs and IDFs. Flame conditions including fuel type, reactant mole fraction, reactant flow rate, diluent, burner port material, burner port diameter, T_{ad} , and Z_{st} are varied. Chemiluminescence associated with major species (C_2^*, CO_2^* CH^*, and OH^*) was measured through image deconvolution and broadband CO_2^* emission correction. Temperatures were measured with B type thermocouples and TFP. Here are the major conclusions:

1) Reactant dilution increased the stoichiometric lengths of both NDFs and IDFs when burner reactant flow rate was constant, although this effect was small for high reactant mole fractions. This counters past assertions that inert addition to the burner reactant has a negligible effect on flame length
2) The analytical model of Roper for stoichiometric flame length predictions was found to hold for normal and inverse diffusion flames over a wide range of conditions. An improved property model is proposed to improve generality and accuracy, especially for fuels with diffusivities different from methane's. The characteristic diffusivity of the gas mixture was taken to be the average diffusivity of the fuel and oxygen into the stoichiometric products. The characteristic temperature was set empirically to 0.735 times the adiabatic temperature plus 0.265 times the ambient temperature, which is the only calibration factor used in the model. The extended Roper model reproduces the measured lengths reasonably well.

3) Double blue zones are observed in non-sooty NDFs and IDFs with various conditions: fuel types (CH_4 and C_3H_8); burner diameters (3 – 14 mm), burner materials (stainless steel, copper, glass), diluents (Ar, CO_2, He, N_2), Z_{st} and T_{ad}. These are more distinct in IDFs than in NDFs. The zones are separated by up to 1.6 mm (and 0.9 mm) at the flame tip for IDFs (and NDFs).

4) For both flame types, the blue zone toward the fuel side is rich and blue-green, while that toward the oxidizer side is stoichiometric, blue, and thicker. The rich zone results from emissions from CH^* and C_2^*. The stoichiometric zone results from CO_2^* emissions and is coincident with the peak in OH^*. All the deconvolved spectral emissive power peaks are higher in the IDF than in the NDF owing to higher scalar dissipation rates.

5) The temperature profile of an NDF (and an IDF) was measured by B-type thermocouple (and TFP). The result support the finding that the temperature peaks at the stoichiometric location for both NDFs and IDFs.

Chapter 7 : Future Work

7.1 Temperature Measurement

1) Future work should find a temperature diagnostic with better spatial resolution for both NDFs and IDFs. Possible solutions include:
   a) A DAQ with higher measurement frequency.
   b) A better welding technique to prepare a thermocouple with a smaller bead.
   c) Other temperature measurement methods other than thermocouple (e.g TFP).
2) It will be helpful to find a relation between the local temperature and major species chemiluminenscence. This could aid estimating species concentrations from flame images.

7.2 Flame Chemiluminenscence and Double Blue Zones

1) Future work should apply laser-induced breakdown spectroscopy (LIBS) to find the diffusion flame stoichiometric location with respect to the double blue zones.
2) LIBS can measure the local equivalence ratio within a diffusion flame across the double blue zones. This will yield relations between flame major species chemiluminescence intensity (or intensity ratios) and local mixture fraction.
3) Future work should develop an inexpensive method to predict the local equivalence ratio within a diffusion flame by local chemiluminescence intensity (or intensity ratios) measured from filtered camera images.

7.3 Numerical Study

Future work should use computational fluid dynamics (CFD) to predict the temperatures, major species, and visible emissions of IFDs and NDFs. Comparing this with the experimental data, will aid the understanding of flame chemistry. The numerical work will also aid the work proposed in sections 7.1 and 7.2.

Appendix A. Image Deconvolution by Onion Peeling Method

Onion peeling is a simple and common deconvolution algorithm in reconstructing local properties from projections in an axisymmetric domain. In this study, the flame radial plane (perpendicular to the flame axis) is assumed to be composed of concentric onion rings. In each ring, the chemiluminenscence luminosities and emissive power of each species are constant. The flame is assumed to be optically thin. Figure A-1 is a schematic for the onion peeling method. The local property can be found as a function of radius using a reconstruction matrix following [80-83].

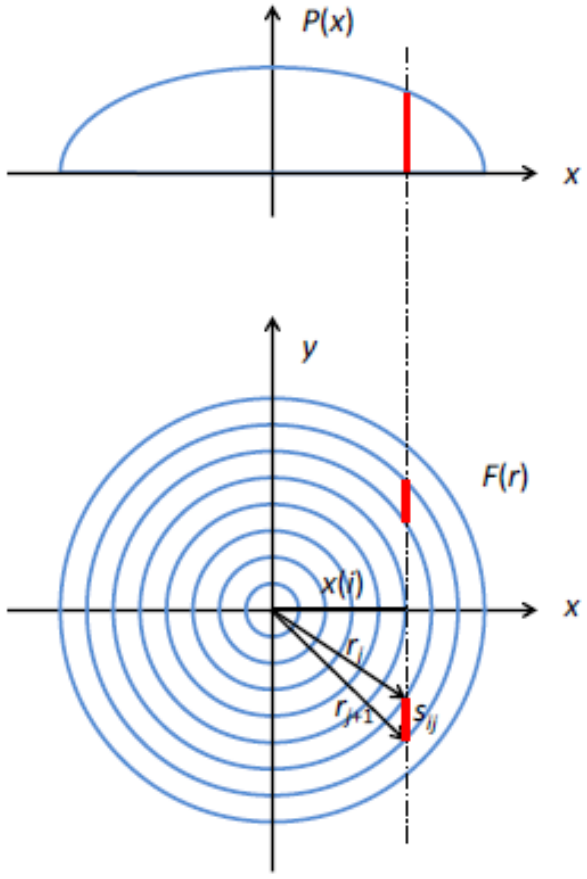

Figure A-1: Schematic of onion peeling method.

$$F(\delta_j) = \sum_{i=j}^{\infty} [S_{ji}]^{-1} P(x_i), \quad r_j < \delta_j < r_{j+1} \tag{A-1}$$

where F is the local property, P is the projected property, r is the radial direction, x is the direction perpendicular to the cord, and δ is the radial location between two adjacent rings. S_{ji} is a reconstruction matrix with the length of the i-th cord in the j-th ring [81]:

$$S_{ji} = 2(\sqrt{{r_{j+1}}^2 - {x_i}^2} - \sqrt{{r_j}^2 - {x_i}^2}) \tag{A-2}$$

Flame image deconvolution starts at flame axis, $P(x_1)$. Therefore, the flame image has to initially be cut into its left and right halves, which are deconvolved individually and then recombined. The results at the axis will be discontinuous, but this will not affect the study conclusion as the double blue zones are far from the axis.

The Savitski-Golay (S-G) filter with optimized parameters framelen=51 and order=1 is applied. Figure A-2 compares the grayscale intensity profiles among GS1 to GS4 for the IDF images from Fig. 4-11a. Deconvolution reduces the I_{GS}. Therefore, GS3 and GS4 are increased to a level that is close to GS1 and GS2 by multiplying by the same constant. Deconvolution increases noise as GS3 is noisier than GS2. GS2 (and GS4) is smoother than GS1 (and GS3). Therefore, data smoothing by the S-G filter method is applied both before and after the deconvolution. The I_{GS} peak shifts toward outside after deconvolution in all of plots. This agrees with the observations in the discussion of Fig. 4-11.

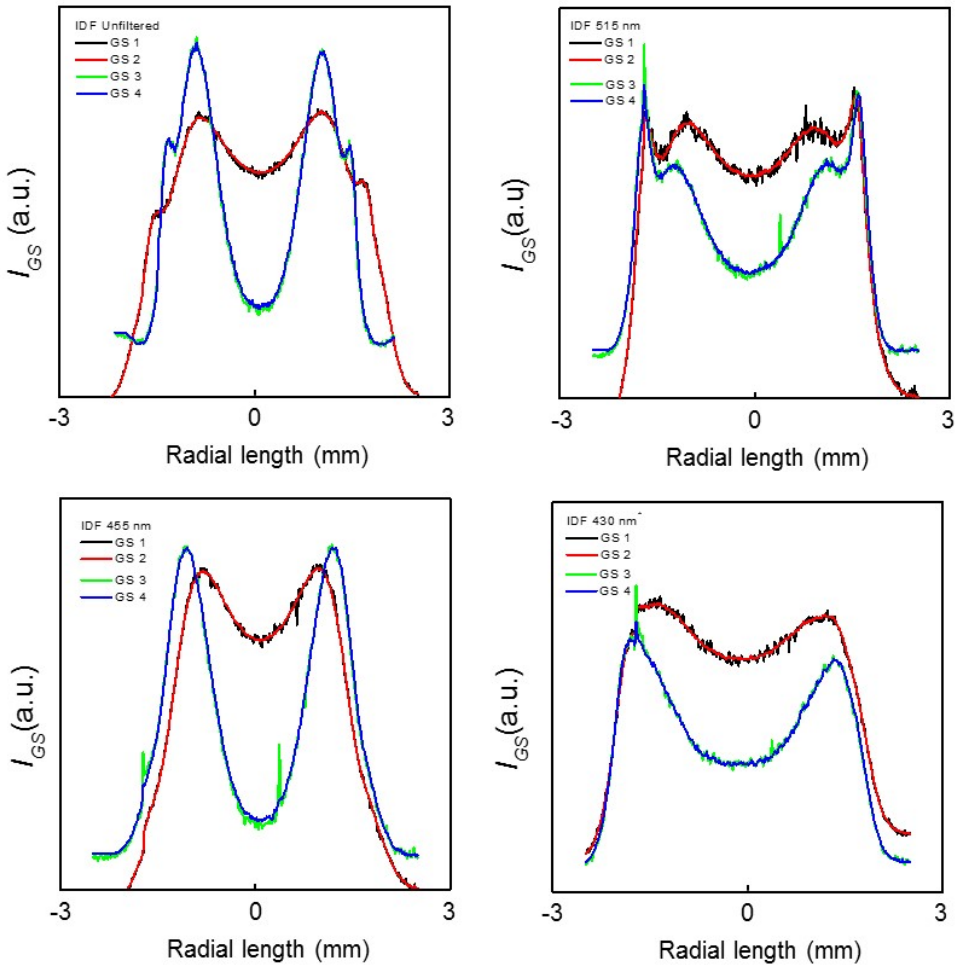

Figure A-2: Grayscale intensity profiles of unfiltered, 515 nm, 455 nm, and 430 nm IDF images in Fig. 4-11a along the radial length at a height of 4 mm. GS1 stands for the grayscale values of photo image read by MATLAB; GS2 is the grayscale value after GS1 being smoothed by S-G filter; GS3 is the grayscale value after GS2 being deconvolved by onion peeling method; GS4 is the grayscale value after GS3 being smoothed by S-G method.

Appendix B. Thermocouple Radiation Corrections

Thermocouple radiation corrections are considered here. Assuming that a steady state exists between convective heat transfer to and radiation from the thermocouple and the bead is spherical, the corrected temperature (ΔT) is [75]

$$\Delta T = (T_m^4 - T_0^4)\, \sigma\, \varepsilon\, D_{bead} / (\, Nu\, k\,) , \qquad \text{(B-1)}$$

where σ is Stefan-Boltzmann constant, 5.67×10^{-8} kg/s^{-3}-K^{-4}, ε is thermocouple emissivity, k is air thermal conductivity, and T_m and T_0 are measured and ambient temperature (298 K). Nu is Nusselt number, defined as [88]

$$Nu = 2 + 0.589\, Ra^{\,0.5} / [\, 1 + (\, 0.469 / Pr\,)^{\,9/16}\,]^{\,4/9} , \qquad \text{(B-2)}$$

where Pr and Ra are the Prandtl number and the Rayleigh number. Ra is defined as [88]

$$Ra = \rho\, \beta\, (\, T_m - T_0\,)\, D_{bead}^3\, g / (\alpha\, \mu) , \qquad \text{(B-3)}$$

where α, ρ and μ are thermal diffusivity, density and dynamic viscosity of air, g is the acceleration of gravity (9.81 m/s^2), and β is the thermal expansion coefficient, defined as.

$$\beta = 2 / (T_m - T_0) , \qquad \text{(B-4)}$$

The emissivity, ε, of a B type thermocouple bead is [89]

$$\varepsilon\,(\mathrm{BTC_{bead}}) = 6\times10^{-5}\, T_m + 0.0006 , \qquad \text{(B-5)}$$

The values of α, k, ρ, and μ from 500 – 2500 K are found from Ref. [90]. These are plotted in Figs. B-1 – B-4. The curve fits shown have as their polynomial fit equations

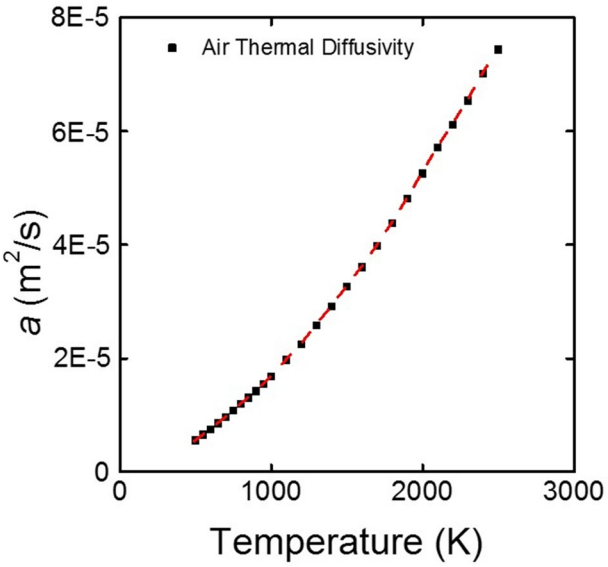

Figure B-1: Air thermal diffusivity vs. temperature.

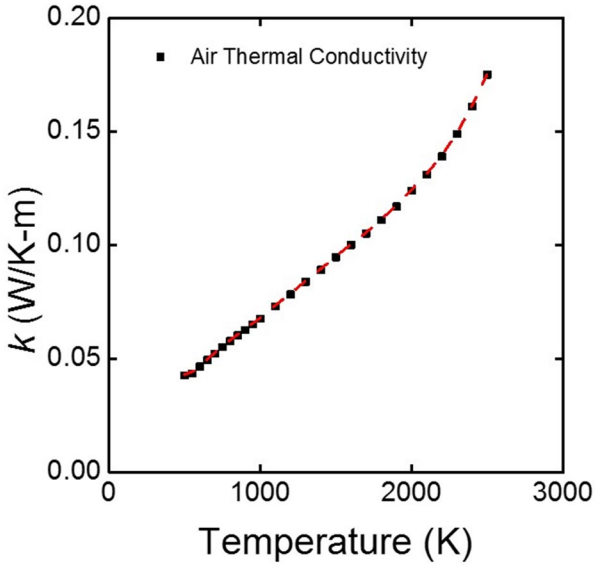

Figure B-2: Air thermal conductivity vs. temperature.

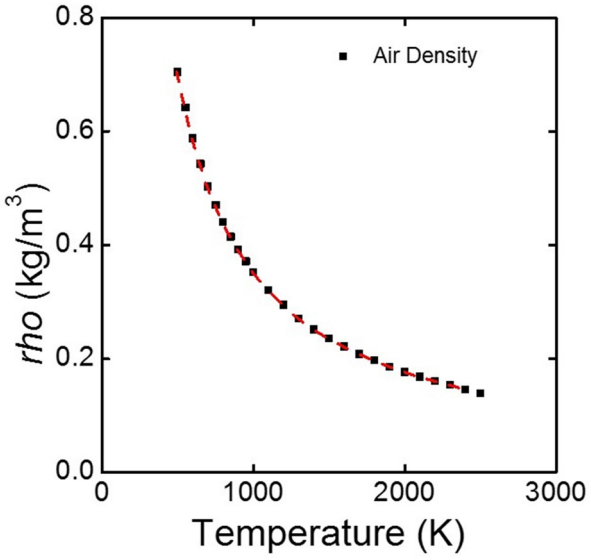

Figure B-3: Air density vs. temperature.

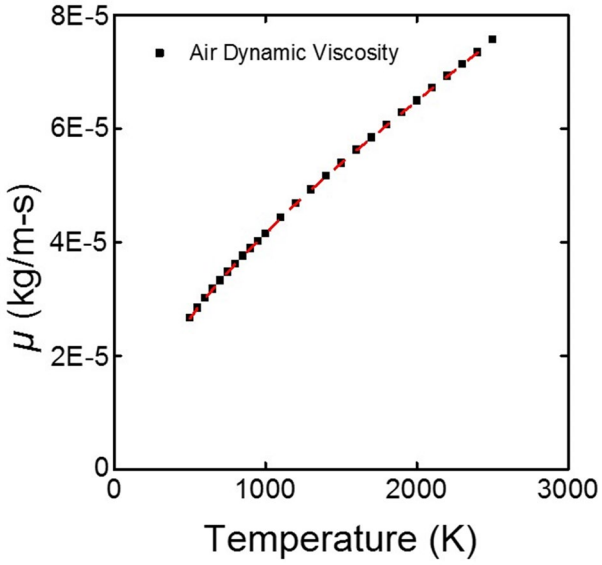

Figure B-4: Air dynamic viscosity vs. temperature.

The value of Prandtl number does not change much as T_m is increased (See Fig. B- 5). It remains constant around 0.70. Therefore, the Prandtl number is set to be 0.7.

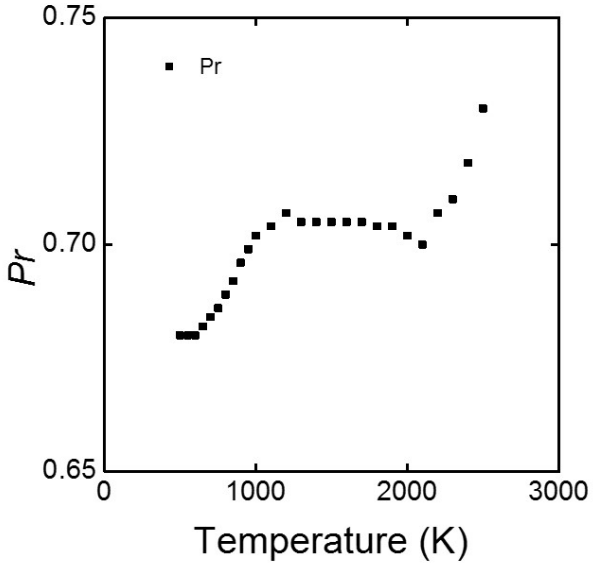

Figure B-5: Air Prandtl numbe vs. temperature.

$$\alpha = -7.289 \times 10^{-21} T_m^5 + 3.833 \times 10^{-17} T_m^4 - 7.193 \times 10^{-14} T_m^3 + 1.435 \times 10^{-10} T_m^2 + 7.919 \times 10^{-8} T_m - 1.279 \times 10^{-5}, \quad \text{(B-6)}$$

$$k = 5.807 \times 10^{-18} T_m^5 - 3.185 \times 10^{-14} T_m^4 + 6.763 \times 10^{-11} T_m^3 - 6.812 \times 10^{-8} T_m^2 + 8.435 \times 10^{-5} T_m - 1.006 \times 10^{-2}, \quad \text{(B-7)}$$

$$\rho = -8.323 \times 10^{-17} T_m^5 + 7.274 \times 10^{-13} T_m^4 - 2.529 \times 10^{-9} T_m^3 + 4.405 \times 10^{-6} T_m^2 - 4.153 \times 10^{-3} T_m + 1.989, \quad \text{(B-8)}$$

$$\mu = 7.763 \times 10^{-22} T_m^5 - 3.124 \times 10^{-18} T_m^4 + 2.036 \times 10^{-14} T_m^3 - 3.625 \times 10^{-11} T_m^2 + 5.878 \times 10^{-8} T_m + 4.267 \times 10^{-6}, \quad \text{(B-9)}$$

Appendix C. MATLAB Scripts

C-1. Onion Peeling Deconvolution

```
% deconvolution with onion peeling method. Input res is the pixel resolution m/pixel.
Input py is the projection data. Output dcy is the radially deconvolved data.

function dcy = OPDecon (res,py)
del=1; % ring size is 1 pixel
[Y,X]=size(py);
if Y >= X
   L = X;
else
   L = Y;
end
x=1:L;
s=zeros(L);
for i=1:L
   for j=i:L
      s(i,j)=2*res*(sqrt((x(i)+del*(j-i+1))^2-x(i)^2)-sqrt((x(i)+del*(j-i))^2-x(i)^2));
   end
end

dcy=s\py; % equal to inv(s)*py
```

C-2. CO_2 Deconvolution

```
close all

clear all

clc

CO2RGB = imread('DSC_1324.tiff'); % CO2 image input

CO2RGB0 = im2double(CO2RGB); % change to double

CO2gray = mean(CO2RGB0,3); % calculate grayscale value

[CO2YL0,CO2XL0]=size(CO2gray);

% crop the image to a smaller size

% remove useless background information and save calculation time

CO2Burnertip = 2876; % the pixel of burner tip

CO2xaxis= 1015; %the pixel of axis

CO2x1=CO2xaxis-300; % left boundary,

CO2y1=CO2Burnertip-1700; % upper boundary,

CO2x2=CO2xaxis+300; % right boundary,

CO2y2=CO2Burnertip+50; % lower boundary,

CO2gray0=CO2gray(CO2y1:CO2y2,CO2x1:CO2x2);

CO2RGB1=CO2RGB0(CO2y1:CO2y2,CO2x1:CO2x2,:);

% Remove background noise

% Get the same size of background

CO2X1=1; % left boundary

CO2Y1=1; % upper boundary

CO2X2=CO2X1+CO2x2-CO2x1; % right boundary
```

```
CO2Y2=CO2Y1+CO2y2-CO2y1; % lower boundary,
% Remove background noise
CO2RGBbg=CO2RGB0(CO2Y1:CO2Y2,CO2X1:CO2X2,:);
CO2gray1=CO2gray0-mean(CO2RGBbg,3);
CO2RGB2=CO2RGB1-CO2RGBbg;
%% Set 0 for negative values
[CO2YL,CO2XL]=size(CO2RGB2(:,:,1));
for i=1:3
   for j=1:CO2XL
   for k=1:CO2YL
   if CO2RGB2(k,j,i)<0
      CO2RGB2(k,j,i)=0;
   end
   end
   end
end
% Consider the transmission
CO2Trans = 0.63; % transmission of the optic filter in a unit of /nm
CO2Expo = 4; % Exposure time in sec
CO2Gray = CO2gray1./CO2Trans./CO2Expo;
CO2RGB3 = CO2RGB2./CO2Trans./CO2Expo;
%Deconvolve the GS values
%Deconvolution constant
```

```
%separate the image by center axis and deconvolved separately.
CO2XL1 = CO2xaxis-CO2x1;
CO2res=0.01; % pixel resolution (mm/pixel)
%Right side deconvolution
for k=1:CO2YL
  CO2Sgray1(k,:)= CO2Gray(CO2YL-k+1,CO2XL1:CO2XL); %flip the Y axis
end
CO2Sgray2(:,:) = CO2Sgray1(:,:)'; %reshape the Matrix. Each row in Sgray is treated as onion ring and should be deconvolved, but in function, columns are deconvolved, so switch the column and rows
%Smooth the input data by Savitzky-Golay filtering
CO2framelen = 51; %framelen must be odd
CO2order = 1;% order must be less than the frame length
CO2Sgray3(:,:)= sgolayfilt(CO2Sgray2(:,:),CO2order,CO2framelen); % Smooth the data before deconvolution
CO2VSgray1(:,:)=OPDeconWang(CO2res,CO2Sgray3(:,:)); %deconvolved the data
CO2VSgray2(:,:) =CO2VSgray1(:,:)';
 for k=1:CO2YL
  CO2VSgray3(k,:) = CO2VSgray2(CO2YL-k+1,:); %flip the Y axis back
 end
%Left side deconvolution
for k =1:CO2YL
   for j = 1: CO2XL1
```

```
  CO2Sgray4(k,j) = CO2Gray(CO2YL-k+1,CO2XL1-j+1); %flip the X and Y axis
   end
end
CO2Sgray5(:,:) = CO2Sgray4(:,:)';
CO2Sgray6(:,:)= sgolayfilt(CO2Sgray5(:,:),CO2order,CO2framelen); % Smooth the
data before deconvolution
CO2VSgray4(:,:)=OPDeconWang(CO2res,CO2Sgray6(:,:)); %deconvolve the data
CO2VSgray5(:,:) =CO2VSgray4(:,:)';
for k =1:CO2YL
   for j = 1: CO2XL1
    CO2VSgray6(k,j) = CO2VSgray5(CO2YL-k+1,CO2XL1-j+1); %flip the X and Y
axis back
   end
end
%Adding the both sides
CO2FinalVSgray(:,1: CO2XL1) = CO2VSgray6(:,:);
CO2FinalVSgray(:, CO2XL1: CO2XL) = CO2VSgray3(:,:);
%Deconvolve the RGB values
%Right side deconvolution
for i =1:3
   for k=1: CO2YL
   CO2RGB4(k,:,i)= CO2RGB3( CO2YL-k+1, CO2XL1: CO2XL,i); %flip the Y axis
   end
```

```
    CO2RGB5(:,:,i) = CO2RGB4(:,:,i)';
    CO2RGB6(:,:,i) = sgolayfilt(CO2RGB5(:,:,i),CO2order,CO2framelen); % Smooth
the data before deconvolution
    CO2RGB7(:,:,i) = OPDeconWang(CO2res,CO2RGB6(:,:,i)); %deconvolved the
data
    CO2RGB8(:,:,i) = CO2RGB7(:,:,i)' ;
   for k=1: CO2YL
    CO2RGB9(k,:,i) = CO2RGB8( CO2YL-k+1,:,i); %flip the Y axis back
   end
end
%Left side deconvolution
for i = 1:3
    for k =1: CO2YL
    for j = 1:  CO2XL1
     CO2RGB10(k,j,i) =  CO2RGB3(CO2YL-k+1,CO2XL1-j+1,i); %flip the X and Y
axis
    end
    end
     CO2RGB11(:,:,i) = CO2RGB10(:,:,i)';
     CO2RGB12(:,:,i)  =  sgolayfilt(CO2RGB11(:,:,i),CO2order,CO2framelen);  %
Smooth the data before deconvolution
     CO2RGB13(:,:,i) = OPDeconWang(CO2res,CO2RGB12 (:,:,i));%deconvolved the
data
```

```
    CO2RGB14(:,:,i) = CO2RGB13(:,:,i)';
   for k =1: CO2YL
   for j = 1:  CO2XL1
       CO2RGB15(k,j,i) = CO2RGB14( CO2YL-k+1, CO2XL1-j+1,i); %flip the X and
Y axis back
   end
end
end
%Adding the both sides
for i =1:3
  CO2FinalRGB(:,1: CO2XL1,i) = CO2RGB15(:,:,i);
  CO2FinalRGB(:, CO2XL1: CO2XL,i) = CO2RGB9(:,:,i);
end
 CO2FinalSRGB = CO2FinalRGB;
% Change RGB to grayscale
CO2FinalPlotgray = mean(CO2FinalRGB,3);
```

C-3. Target Deconvolution

```
% Target image input
TargetRGB = imread('DSC_1323.tiff');
TargetRGB0 = im2double(TargetRGB);
Targetgray = mean(TargetRGB0,3);
[TargetYL0,TargetXL0]=size(Targetgray);
% crop the image to a smaller size
```

```
% remove useless background information and save calculation time
TargetBurnertip = 2866; % the pixel of burner tip
Targetxaxis=1025; %the pixel of axis
Targetx1=Targetxaxis-300; % left location,
Targety1=TargetBurnertip-1700; % upper location
Targetx2=Targetxaxis+300; % right location
Targety2=TargetBurnertip+50; % lower location, the burner tip.
gray0=Targetgray(Targety1:Targety2,Targetx1:Targetx2);
TargetRGB1=TargetRGB0(Targety1:Targety2,Targetx1:Targetx2,:);
%% Remove background noise
%% Get the same size of background
TargetX1=1; % left location,
TargetY1=1; % upper location
TargetX2=TargetX1+Targetx2-Targetx1; % right location
TargetY2=TargetY1+Targety2-Targety1; % lower location,
%% Remove background noise
TargetRGBbg=TargetRGB0(TargetY1:TargetY2,TargetX1:TargetX2,:);
Targetgray1=gray0-mean(TargetRGBbg,3);
TargetRGB2=TargetRGB1-TargetRGBbg;
%% Set 0 for negative values
[TargetYL,TargetXL]=size(TargetRGB2(:,:,1));
for i=1:3
   for j=1:TargetXL
```

```
    for k=1:TargetYL
    if TargetRGB2(k,j,i)<0
      TargetRGB2(k,j,i)=0;
    end
    end
    end
end
% % Consider the transmission
TargetTrans = 0.65; % transmission of the optic filter in a unit of /nm
TargetExpo = 4; % Exposure time
TargetGray = Targetgray1./TargetTrans./TargetExpo;
TargetRGB3 = TargetRGB2./TargetTrans./TargetExpo;
%Smooth the input data by Savitzky-Golay filtering
Targetframelen = 51; %framelen must be odd
Targetorder = 1;% order must be less than the frame length
%Deconvolute the GS values
TargetXL1 = Targetxaxis-Targetx1;
Targetres=0.01; % pixel resolution (mm/pixel)
%Right side deconvolution
for k=1:TargetYL
  TargetSgray1(k,:)= TargetGray(TargetYL-k+1,TargetXL1:TargetXL); %flip the Y
axis
end
```

```
TargetSgray2(:,:) = TargetSgray1(:,:)'; %reshape the Matrix. Each row in Sgray is treated as onion ring and should be deconvolved, but in function, columns are deconvolved, so switch the column and rows
TargetSgray3(:,:)= sgolayfilt(TargetSgray2(:,:),Targetorder,Targetframelen); % Smooth the data before deconvolution
TargetVSgray1(:,:)=OPDeconWang(Targetres,TargetSgray3(:,:)); %deconvolve the data
TargetVSgray2(:,:) =TargetVSgray1(:,:)';
 for k=1:TargetYL
   TargetVSgray3(k,:) = TargetVSgray2(TargetYL-k+1,:); %flip the Y axis back
 end
%Left side deconvolution
for k =1:TargetYL
    for j = 1: TargetXL1
   TargetSgray4(k,j) = TargetGray(TargetYL-k+1,TargetXL1-j+1); %flip the X and Y axis
    end
end
TargetSgray5(:,:) = TargetSgray4(:,:)';
TargetSgray6(:,:)= sgolayfilt(TargetSgray5(:,:),Targetorder,Targetframelen); % Smooth the data before deconvolution
TargetVSgray4(:,:)=OPDeconWang(Targetres,TargetSgray6(:,:)); %deconvolve the data
```

```
TargetVSgray5(:,:) =TargetVSgray4(:,:)';
for k =1:TargetYL
   for j = 1: TargetXL1
    TargetVSgray6(k,j) = TargetVSgray5(TargetYL-k+1,TargetXL1-j+1); %flip the X
and Y axis back
   end
end
%Adding the both sides
TargetFinalVSgray(:,1: TargetXL1) = TargetVSgray6(:,:);
TargetFinalVSgray(:, TargetXL1: TargetXL) = TargetVSgray3(:,:);
%Deconvolve the RGB values
%Right side deconvolution
for i =1:3
   for k=1: TargetYL
   TargetRGB4(k,:,i)=  TargetRGB3( TargetYL-k+1, TargetXL1: TargetXL,i); %flip
the Y axis
   end
   TargetRGB5(:,:,i) =  TargetRGB4(:,:,i)';
   TargetRGB6(:,:,i)  =  sgolayfilt(TargetRGB5(:,:,i),Targetorder,Targetframelen);  %
Smooth the data before deconvolution
   TargetRGB7(:,:,i)  =  OPDeconWang(Targetres,TargetRGB6(:,:,i));  %deconvolve
the data
   TargetRGB8(:,:,i) = TargetRGB7(:,:,i)' ;
```

```
  for k=1: TargetYL
   TargetRGB9(k,:,i) = TargetRGB8( TargetYL-k+1,:,i); %flip the Y axis back
  end
end
%Left side deconvolution
for i = 1:3
   for k =1: TargetYL
   for j = 1:  TargetXL1
    TargetRGB10(k,j,i) =  TargetRGB3(TargetYL-k+1,TargetXL1-j+1,i); %flip the X
and Y axis
   end
   end
    TargetRGB11(:,:,i) = TargetRGB10(:,:,i)';
    TargetRGB12(:,:,i)  =  sgolayfilt(TargetRGB11(:,:,i),Targetorder,Targetframelen);
% Smooth the data before deconvolution
    TargetRGB13(:,:,i) =OPDeconWang(Targetres,TargetRGB12 (:,:,i));%deconvolve
the data
    TargetRGB14(:,:,i) = TargetRGB13(:,:,i)';
   for k =1:TargetYL
   for j = 1:TargetXL1
       TargetRGB15(k,j,i) = TargetRGB14( TargetYL-k+1, TargetXL1-j+1,i); %flip
the X and Y axis back
   end
```

```
end
end
%Adding the both sides
for i =1:3
   TargetFinalRGB(:,1: TargetXL1,i) = TargetRGB15(:,:,i);
   TargetFinalRGB(:, TargetXL1: TargetXL,i) = TargetRGB9(:,:,i);
end
 TargetFinalSRGB = TargetFinalRGB;
% Change RGB to grayscale
TargetFinalPlotgray = mean(TargetFinalRGB,3);
%% For Unfiltered Image
% TargetFinalPlotgray1= sgolayfilt(TargetFinalPlotgray,Targetorder,Targetframelen);
% Y = TargetBurnertip - 400; % Choose a Y location to plot
% t=0:TargetXL-1;
% Test2(1,:)= TargetFinalPlotgray1(round(Y-Targety1),:)*1000;
```

C-4. Deduct CO2 Intensity from Target Intensity

```
%defining alpha, the ratio of the CO2* intensity at wavelength lamda divided by that
at 455 nm for methane-air diffusion flames
CHSensitivity = 0.89; % m2/Ws
CO2Sensitivity = 1;
C2Sensitivity = 0.75;
%defineing beta, the ratio of the camera sensitivity with a filter at wavelength lamda
divided by that at 455 nm
```

```
CHBackgroundfactor = 1;

CO2Backgroundfactor = 1;

C2Backgroundfactor = 2/3;


TargetFinalPlotgray1 = TargetFinalPlotgray/C2Sensitivity/C2Backgroundfactor;

CO2FinalPlotgray1= CO2FinalPlotgray/CO2Sensitivity/CO2Backgroundfactor;

FinalVSgray0 = (TargetFinalPlotgray1- CO2FinalPlotgray1);

FinalVSgray1 = FinalVSgray0;


% % For unfiltered image

% TargetFinalPlotgray1 = TargetFinalPlotgray;

% CO2FinalPlotgray1= CO2FinalPlotgray/CO2Sensitivity/CO2Backgroundfactor;

% FinalVSgray0 = TargetFinalPlotgray;

% FinalVSgray1 = FinalVSgray0;

%Smooth the deconvolve data by Savitzky-Golay filtering

Finalframelen = 11; %framelen must be odd

Finalorder = 1;% order must be less than the frame length

FinalVSgray2 = sgolayfilt(FinalVSgray1,Finalorder,Finalframelen);

%increase the signal intensity to plot the images.

Factor = 5; % Intensity factor

FinalVSgray3 =  FinalVSgray2 * Factor;

%Calculate the Intensity of each color pixel

%The sensitivity ratio of colors at each wavelength are taken into calculation.
```

```
%The following values are calibrated by blackbody furnace
CHredratio = 0.036312;
CHgreenratio = 0.000258;
CHblueratio = 0.963430;
CO2redratio = 0.006721;
CO2greenratio = 0.000009;
CO2blueratio = 0.993270;
C2redratio = 0.000005;
C2greenratio = 0.998605;
C2blueratio = 0.001390;
FinalSRGB = TargetRGB1;
FinalSRGB (:,:,1) = FinalVSgray3 * C2redratio;
FinalSRGB (:,:,2) = FinalVSgray3 * C2greenratio;
FinalSRGB (:,:,3) = FinalVSgray3 * C2blueratio;
```

C-5. Plots

```
Y = TargetBurnertip - 400; % Choose a Y location to plot
t=0:TargetXL-1;
% Compare the Deconvolution CO2 GS, Deconvolution Target GS and Corrected
Target GS
figure (1)
plot(t,CO2FinalPlotgray1(round(Y-Targety1),:),'r',t,TargetFinalPlotgray1(round(Y-
Targety1),:),'g',t,FinalVSgray2(round(Y-Targety1),:),'b');
title('Deconvoluted C2 IDF');
```

```
legend('Deconvolution CO2 GS','Deconvolution C2 GS','Corrected C2 GS');
Test1(1,:)= CO2FinalPlotgray1(round(Y-Targety1),:);
Test1(2,:)= TargetFinalPlotgray1(round(Y-Targety1),:);
Test1(3,:)= FinalVSgray2(round(Y-Targety1),:);


figure (2)
CO2Gray1 = CO2Gray/CO2Sensitivity*C2Sensitivity/6;
TargetGray1 =TargetGray/4;
plot(t,CO2Gray1(round(Y-Targety1),:),'r',t,TargetGray1(round(Y-Targety1),:),'g');
title('CO2 Gray From Image vs Target Gray From Image');
legend('CO2 Gray From Image','Target Gray From Image');


figure (3)
plot(t,FinalSRGB(round(Y-Targety1),:,1),'r',t,FinalSRGB(round(Y-
Targety1),:,2),'g',t,FinalSRGB(round(Y-Targety1),:,3),'b');
title('CO2 Corrected C2 IDF');
legend('Corrected C2 Red','Corrected C2 Green','Corrected C2 Blue');


% Plot the photo image
figure (4)
imshow( TargetRGB1,[],'InitialMagnification',10);
title(' C2 color Image');
```

```
figure (5)
TargetFinalSRGBx = TargetFinalSRGB*10;
imshow(  TargetFinalSRGBx,[],'InitialMagnification',10);
title(' Deconvoluted C2  Image');

% Plot CO2
figure (6)
CO2FinalSRGBx = CO2FinalSRGB.*15;
imshow(  CO2FinalSRGBx,[],'InitialMagnification',10);
title(' Deconvoluted C2  Image');

%%Plot the final image
figure (7)
FinalSRGBx= FinalSRGB*10;
imshow( FinalSRGBx,[],'InitialMagnification',10);
title(' Deconvoluted + Corrected C2 Image');

%Plot the compare image
figure (8)
imshow( CompareFinalRGB,[],'InitialMagnification',10);
title('left : deconvolution image; right : deconvolutiion + correction image');
```

```
% Plot the highest intensity location along the axis
figure (9)
z0 = Targety2-TargetBurnertip;
Ylimit = 00;
Xlimit = 0;
% For Target
for k=1:TargetYL
  FinalVSgray4(k,:)= FinalVSgray1(TargetYL-k+1,:); %flip the Y axis
end
FinalVSgray5 =FinalVSgray4 (z0:TargetYL-Ylimit,1: TargetXL1-Xlimit); % Matrix
with Y start at burner tip
[~,MaxGSC2x] = max(FinalVSgray5,[],2); % Find the Max value at each raw.
% [~,MaxGSCHx] = max(FinalVSgray5,[],2); % Find the Max value at each raw.

% For CO2
for k=1: CO2YL
 CO2FinalPlotgray2(k,:)= CO2FinalPlotgray (CO2YL-k+1,:); %flip the Y axis
end
CO2FinalPlotgray3 =CO2FinalPlotgray2(z0: CO2YL-Ylimit,1:  CO2XL1-Xlimit); %
Matrix with Y start at burner tip
[~,MaxGSCO2x] = max(CO2FinalPlotgray3,[],2); % Find the Max value at each raw.
z = 0:TargetYL-Ylimit-z0;
plot(MaxGSC2x,z,'g',MaxGSCO2x,z,'b');
```

```
% plot(MaxGSC2x,z,'g',MaxGSCO2x,z,'b');
title('Max GS Intensity along the flame height');
legend('CH IDF','CO2 IDF');
xlabel('Radius') % x-axis label
ylabel('axis') % y-axis label% %% Check the Gs intensity before and after deconvolution
```

Appendix D. Detailed Information of Flames in Fig.3-6

Table D-1 Information of the methane NDFs.

Flame #	Photo #	Q_{CH4} (ccm)	X_{CH4}	X_{O2}	S	T_{ad} (K)	T_{char} (K)	D_{Char} (mm^2/s)	$L_{St,model}$ (mm)	$L_{St,meas}$ (mm)
N1	0012	123.58	0.61	0.21	5.77	2156.88	1664.28	19.77	27.17	19.57
N2	0013	123.58	0.53	0.21	5.08	2134.11	1647.54	19.79	27.60	20.88
N3	0015	123.58	0.47	0.21	4.48	2109.07	1629.14	19.82	28.09	21.62
N4	0016	123.58	0.47	0.21	4.48	2109.07	1629.14	19.82	28.09	22.43
N5	0017	123.58	0.42	0.21	3.97	2081.87	1609.15	19.84	28.63	24.48
N6	0021	123.58	0.61	0.30	3.98	2466.52	1891.87	19.34	18.19	12.47
N7	0022	123.58	0.33	0.30	2.17	2320.85	1784.79	19.57	20.27	19.41
N8	0025	123.58	0.53	0.30	3.50	2442.76	1874.40	19.38	18.52	13.48
N9	0026	123.58	0.47	0.30	3.09	2416.30	1854.95	19.42	18.89	14.75
N10	0027	123.58	0.42	0.30	2.74	2387.14	1833.52	19.47	19.30	16.00
N11	0029	123.58	0.37	0.30	2.43	2355.31	1810.12	19.52	19.76	17.31
N12	0030	123.58	0.30	0.30	1.95	2283.85	1757.60	19.62	20.82	20.94
N13	0032	123.58	0.27	0.30	1.75	2244.43	1728.62	19.67	21.42	23.10
N14	0035	123.58	0.53	0.40	2.65	2611.84	1998.67	19.03	14.17	10.21
N15	0036	123.58	0.47	0.40	2.34	2585.35	1979.20	19.09	14.48	10.99
N16	0037	123.58	0.42	0.40	2.07	2556.33	1957.87	19.16	14.83	11.87
N17	0038	123.58	0.37	0.40	1.84	2524.72	1934.64	19.22	15.22	13.01
N18	0039	123.58	0.33	0.40	1.64	2490.46	1909.45	19.29	15.65	14.28
N19	0040	123.58	0.30	0.40	1.47	2453.48	1882.28	19.36	16.11	16.13
N20	0042	123.58	0.27	0.40	1.32	2413.76	1853.08	19.43	16.62	17.57
N21	0043	123.58	0.24	0.40	1.20	2371.31	1821.88	19.49	17.17	19.15
N22	0044	123.58	0.22	0.40	1.09	2326.20	1788.73	19.56	17.77	20.48
N23	0045	123.58	0.20	0.40	0.99	2278.60	1753.74	19.62	18.41	21.77
N24	0047	123.58	0.42	0.51	1.63	2668.41	2040.25	18.88	12.07	9.52
N25	0048	123.58	0.47	0.51	1.84	2698.30	2062.22	19.47	18.11	18.79

Flame #	Photo #	Q_{CH4} (ccm)	X_{CH4}	X_{O2}	S	T_{ad} (K)	T_{char} (K)	D_{Char} (mm^2/s)	$L_{St,model}$ (mm)	$L_{St,meas}$ (mm)
N26	0049	123.58	0.37	0.51	1.45	2636.15	2016.54	19.55	18.38	18.96
N27	0050	123.58	0.33	0.51	1.29	2601.54	1991.10	19.59	18.52	19.05
N28	0051	123.58	0.30	0.51	1.16	2564.52	1963.89	19.62	18.66	19.14
N29	0052	123.58	0.27	0.51	1.04	2524.98	1934.83	19.66	18.79	19.22
N30	0054	123.58	0.24	0.51	0.94	2482.78	1903.82	19.69	18.92	19.31
N31	0055	123.58	0.22	0.51	0.86	2437.84	1870.78	19.73	19.05	19.39
N32	0056	123.58	0.20	0.51	0.78	2390.10	1835.70	19.76	19.17	19.47
N33	0058	123.58	0.20	0.60	0.66	2452.31	1881.42	19.72	19.01	19.36
N34	0059	123.58	0.22	0.60	0.73	2499.86	1916.37	19.68	18.87	19.27
N35	0060	123.58	0.24	0.60	0.80	2544.67	1949.31	19.64	18.72	19.18
N36	0062	123.58	0.27	0.60	0.89	2586.91	1980.35	19.60	18.57	19.09
N37	0064	123.58	0.30	0.60	0.99	2626.75	2009.63	19.56	18.42	18.99
N38	0065	123.58	0.33	0.60	1.10	2664.32	2037.25	19.51	18.26	18.89
N39	0066	123.58	0.37	0.60	1.23	2699.64	2063.21	19.47	18.10	18.79
N40	0068	123.58	0.42	0.60	1.39	2732.62	2087.44	19.42	17.94	18.68
N41	0069	123.58	0.20	0.70	0.57	2502.06	1917.99	19.68	18.86	19.27
N42	0071	123.58	0.22	0.70	0.62	2549.52	1952.87	19.64	18.71	19.17
N43	0072	123.58	0.24	0.70	0.69	2594.43	1985.88	19.59	18.55	19.07
N44	0074	123.58	0.27	0.70	0.76	2637.02	2017.18	19.55	18.38	18.96
N45	0075	123.58	0.30	0.70	0.85	2677.43	2046.88	19.50	18.20	18.85
N46	0076	123.58	0.33	0.70	0.94	2715.67	2074.99	19.45	18.02	18.74
N47	0078	123.58	0.37	0.70	1.06	2751.58	2101.38	19.40	17.84	18.62
N48	0079	123.58	0.42	0.70	1.19	2784.93	2125.89	19.34	17.66	18.50
N49	0080	123.58	0.47	0.70	1.34	2815.51	2148.37	19.29	17.47	18.38
N50	0081	123.58	0.20	0.80	0.50	2540.09	1945.94	19.64	18.74	19.19
N51	0084	123.58	0.22	0.80	0.55	2587.61	1980.86	19.60	18.57	19.09
N52	0085	123.58	0.24	0.80	0.60	2632.81	2014.09	19.55	18.39	18.97
N53	0086	123.58	0.27	0.80	0.67	2675.88	2045.74	19.50	18.21	18.86

Flame #	Photo #	Q_{CH4} (ccm)	X_{CH4}	X_{O2}	S	T_{ad} (K)	T_{char} (K)	D_{Char} (mm^2/s)	$L_{St,model}$ (mm)	$L_{St,meas}$ (mm)
N54	0088	123.58	0.30	0.80	0.74	2716.85	2075.86	19.45	18.02	18.73
N55	0089	123.58	0.33	0.80	0.82	2755.56	2104.30	19.39	17.82	18.61
N56	0090	123.58	0.37	0.80	0.92	2791.70	2130.87	19.33	17.62	18.47
N57	0091	123.58	0.42	0.80	1.04	2825.07	2155.39	19.27	17.41	18.34
N58	0093	123.58	0.20	0.90	0.44	2568.28	1966.66	19.62	18.64	19.13
N59	0095	123.58	0.22	0.90	0.49	2615.97	2001.71	19.57	18.46	19.02
N60	0096	123.58	0.24	0.90	0.54	2661.52	2035.18	19.52	18.27	18.90
N61	0097	123.58	0.27	0.90	0.59	2705.02	2067.16	19.46	18.08	18.77
N62	0099	123.58	0.30	0.90	0.66	2746.38	2097.56	19.40	17.87	18.64
N63	0100	123.58	0.33	0.90	0.74	2785.28	2126.15	19.34	17.65	18.50
N64	0101	123.58	0.37	0.90	0.83	2821.44	2152.73	19.28	17.43	18.36
N65	0104	123.58	0.20	0.96	0.42	2582.95	1977.44	19.60	18.59	19.10
N66	0105	123.58	0.22	0.96	0.46	2630.78	2012.60	19.55	18.40	18.98
N67	0106	123.58	0.24	0.96	0.50	2676.54	2046.23	19.50	18.21	18.85
N68	0107	123.58	0.27	0.96	0.56	2720.28	2078.38	19.44	18.00	18.72
N69	0108	123.58	0.30	0.96	0.62	2761.80	2108.89	19.38	17.79	18.58
N70	0109	123.58	0.33	0.96	0.69	2800.74	2137.52	19.32	17.56	18.44
N71	0110	123.58	0.37	0.96	0.77	2836.89	2164.09	19.25	17.33	18.29
N72	0113	123.58	1.00	0.19	10.58	2115.69	1634.00	19.90	19.72	19.81
N73	0114	123.58	0.18	0.96	0.39	2541.10	1946.68	19.64	18.74	19.19
N74	0115	123.58	0.15	0.96	0.32	2432.34	1866.74	19.73	19.06	19.40
N75	0117	123.58	0.18	0.93	0.39	2535.81	1942.79	19.65	18.75	19.20
N76	0118	123.58	0.15	0.93	0.33	2427.02	1862.83	19.73	19.08	19.41
N77	0120	123.58	0.18	0.91	0.41	2528.97	1937.76	19.65	18.78	19.22
N78	0121	123.58	0.15	0.91	0.34	2420.15	1857.78	19.74	19.10	19.42
N79	0123	123.58	0.18	0.87	0.42	2519.82	1931.04	19.66	18.81	19.23
N80	0124	123.58	0.15	0.87	0.35	2410.94	1851.01	19.74	19.12	19.43
N81	0125	123.58	0.14	0.87	0.33	2357.42	1811.67	19.78	19.25	19.51

Flame #	Photo #	Q_{CH4} (ccm)	X_{CH4}	X_{O2}	S	T_{ad} (K)	T_{char} (K)	D_{Char} (mm^2/s)	$L_{St,model}$ (mm)	$L_{St,meas}$ (mm)
N82	0126	123.58	0.18	0.83	0.44	2508.00	1922.35	19.67	18.84	19.26
N83	0127	123.58	0.15	0.83	0.37	2399.04	1842.27	19.75	19.15	19.45
N84	0129	123.58	0.18	0.79	0.47	2493.45	1911.66	19.68	18.89	19.29
N85	0130	123.58	0.15	0.79	0.39	2384.41	1831.51	19.76	19.19	19.47
N86	0132	123.58	0.18	0.71	0.52	2463.03	1889.30	19.71	18.98	19.34
N87	146	31.45	0.48	0.21	4.57	2113.21	1632.18	19.90	19.73	19.81
N88	152	31.45	0.67	0.21	6.37	2172.68	1675.89	19.87	19.63	19.75
N89	184	268.45	0.38	0.50	1.50	2635.87	2016.34	19.55	18.38	18.97
N90	185	268.45	0.33	0.50	1.31	2594.39	1985.84	19.59	18.55	19.07
N91	186	268.45	0.28	0.50	1.13	2544.30	1949.03	19.64	18.73	19.18
N92	187	268.45	0.25	0.50	1.00	2495.70	1913.31	19.68	18.88	19.28
N93	188	268.45	0.23	0.50	0.90	2448.39	1878.54	19.72	19.02	19.37
N94	189	268.45	0.21	0.50	0.82	2402.33	1844.68	19.75	19.14	19.45
N95	190	268.45	0.19	0.50	0.75	2357.59	1811.80	19.78	19.25	19.51
N96	191	268.45	0.18	0.50	0.70	2314.29	1779.98	19.80	19.35	19.58
N97	195	268.45	0.33	0.70	0.94	2715.98	2075.22	19.45	18.02	18.74
N98	196	268.45	0.25	0.70	0.72	2614.89	2000.92	19.57	18.47	19.02
N99	197	268.45	0.21	0.70	0.59	2521.62	1932.36	19.66	18.80	19.23
N100	208	268.45	0.52	0.21	4.93	2128.35	1643.31	19.89	19.70	19.80
N101	211	268.45	0.48	0.21	4.55	2112.21	1631.45	19.90	19.73	19.81
N102	212	268.45	0.44	0.21	4.20	2095.05	1618.84	19.90	19.76	19.83
N103	0221	123.58	0.42	0.21	3.97	2081.87	1609.15	19.91	19.78	19.84
N104	0222	123.58	0.37	0.21	3.53	2052.66	1587.67	19.92	19.82	19.87
N105	0224	123.58	0.47	0.21	4.48	2109.07	1629.14	19.90	19.73	19.82
N106	0229	166.01	0.54	0.21	5.18	2137.90	1650.33	19.89	19.69	19.79
N107	0230	166.01	0.49	0.21	4.66	2117.34	1635.21	19.90	19.72	19.81
N108	0231	166.01	0.44	0.21	4.20	2095.12	1618.89	19.90	19.76	19.83
N109	0237	166.01	0.44	0.51	1.73	2682.99	2050.96	19.49	18.18	18.83

Flame #	Photo #	Q_{CH4} (ccm)	X_{CH4}	X_{O2}	S	T_{ad} (K)	T_{char} (K)	D_{Char} (mm^2/s)	$L_{St,model}$ (mm)	$L_{St,meas}$ (mm)
N110	0238	166.01	0.33	0.51	1.28	2599.16	1989.36	19.59	18.53	19.06
N111	0239	166.01	0.27	0.51	1.07	2534.28	1941.67	19.65	18.76	19.20
N112	0242	166.01	0.40	0.70	1.14	2772.96	2117.10	19.36	17.72	18.54
N113	0243	166.01	0.33	0.70	0.94	2713.21	2073.18	19.45	18.04	18.74
N114	0244	166.01	0.27	0.70	0.78	2646.49	2024.14	19.54	18.34	18.94
N115	0245	394.33	0.47	0.70	1.35	2815.98	2148.72	19.29	17.47	18.38
N116	0246	166.01	0.27	1.00	0.55	2739.96	2092.84	19.41	17.90	18.66
N117	0247	166.01	0.33	1.00	0.66	2808.26	2143.04	19.30	17.52	18.41
N118	0248	166.01	0.40	1.00	0.80	2868.43	2187.27	19.18	17.11	18.15
N119	0249	166.01	0.49	1.00	0.98	2922.19	2226.78	19.05	16.69	17.87
N120	0250	166.01	0.29	1.00	0.58	2762.78	2109.61	19.38	17.78	18.58
N121	0251	166.01	0.24	1.00	0.47	2675.36	2045.36	19.50	18.21	18.86
N122	0252	166.01	0.20	1.00	0.40	2593.83	1985.44	19.59	18.55	19.07
N123	0253	166.01	0.17	1.00	0.35	2516.50	1928.60	19.67	18.82	19.24
N124	0254	166.01	0.15	1.00	0.31	2441.71	1873.63	19.72	19.04	19.38
N125	0255	166.01	0.14	1.00	0.28	2368.75	1820.00	19.77	19.22	19.50
N126	0259	394.33	0.30	1.00	0.61	2780.53	2122.66	19.35	17.68	18.52
N127	0260	394.33	0.26	1.00	0.52	2717.07	2076.02	19.45	18.02	18.73
N128	0261	394.33	0.23	1.00	0.45	2656.85	2031.75	19.52	18.29	18.91
N129	0262	394.33	0.20	1.00	0.40	2598.29	1988.72	19.59	18.53	19.06
N130	0263	394.33	0.19	1.00	0.37	2554.24	1956.34	19.63	18.69	19.16
N131	0264	166.01	0.29	0.70	0.83	2668.65	2040.43	19.51	18.24	18.88
N132	0265	166.01	0.20	0.70	0.57	2503.42	1918.99	19.68	18.86	19.27
N133	0266	166.01	0.15	0.70	0.44	2350.83	1806.83	19.78	19.27	19.52
N134	0269	394.33	0.37	0.70	1.06	2752.72	2102.22	19.40	17.84	18.62
N135	0270	394.33	0.30	0.70	0.87	2685.97	2053.16	19.49	18.16	18.83
N136	0271	394.33	0.26	0.70	0.74	2624.30	2007.83	19.56	18.43	19.00
N137	0272	394.33	0.23	0.70	0.65	2565.66	1964.73	19.62	18.65	19.14

Flame #	Photo #	Q_{CH4} (ccm)	X_{CH4}	X_{O2}	S	T_{ad} (K)	T_{char} (K)	D_{Char} (mm^2/s)	$L_{St,model}$ (mm)	$L_{St,meas}$ (mm)
N138	0273	394.33	0.20	0.70	0.57	2507.86	1922.25	19.67	18.84	19.26
N139	0274	394.33	0.19	0.70	0.53	2463.87	1889.91	19.71	18.98	19.34
N140	0275	166.01	0.29	0.51	1.13	2555.96	1957.60	19.63	18.69	19.16
N141	0279	394.33	0.37	0.51	1.46	2637.25	2017.35	19.55	18.38	18.96
N142	0280	394.33	0.30	0.51	1.19	2572.81	1969.98	19.61	18.63	19.12
N143	0281	394.33	0.23	0.51	0.89	2454.03	1882.68	19.71	19.00	19.36
N144	0282	394.33	0.26	0.51	1.01	2512.43	1925.61	19.67	18.83	19.25
N145	0283	394.33	0.20	0.51	0.79	2395.94	1839.98	19.75	19.16	19.46
N146	0285	268.45	0.29	1.00	0.57	2759.93	2107.51	19.38	17.80	18.59
N147	0286	268.45	0.23	1.00	0.46	2662.17	2035.66	19.52	18.27	18.89
N148	0287	268.45	0.19	1.00	0.38	2572.54	1969.78	19.61	18.63	19.12
N149	0288	268.45	0.17	1.00	0.33	2486.85	1906.81	19.69	18.91	19.30
N150	0289	268.45	0.15	1.00	0.29	2401.62	1844.16	19.75	19.14	19.45
N151	0290	268.45	0.13	1.00	0.27	2336.64	1796.40	19.79	19.30	19.54
N152	0291	268.45	0.19	1.00	0.38	2572.54	1969.78	19.61	18.63	19.12
N125	0255	166.01	0.14	1.00	0.28	2368.75	1820.00	19.77	19.22	19.50

Table D-2; Information of the methane IDFs.

Flame #	Photo #	Q_{O2} (ccm)	X_{O2}	X_{CH4}	S	T_{ad} (K)	T_{char} (K)	D_{Char} (mm^2/s)	$L_{St,model}$ (mm)	$L_{St,meas}$ (mm)
I1	326	181.20	0.38	0.67	0.29	2622.94	2006.83	19.00	6.18	6.72
I2	327	181.20	0.35	0.67	0.26	2568.70	1966.97	19.13	6.51	7.80
I3	329	181.20	0.32	0.67	0.24	2511.17	1924.68	19.25	6.87	7.88
I4	330	181.20	0.28	0.67	0.21	2417.87	1856.10	19.42	7.47	9.06
I5	332	181.20	0.28	0.67	0.21	2417.87	1856.10	19.42	7.47	9.14
I6	347	181.20	0.51	0.48	0.53	2704.04	2066.44	18.77	6.49	6.02
I7	348	181.20	0.42	0.48	0.44	2612.14	1998.90	19.03	7.09	7.15
I8	349	181.20	0.35	0.48	0.36	2507.69	1922.12	19.26	7.80	8.03
I9	350	181.20	0.32	0.48	0.33	2450.06	1879.76	19.37	8.20	9.31
I10	351	181.20	0.28	0.48	0.29	2356.46	1810.97	19.52	8.88	10.62
I11	355	181.20	0.76	0.32	1.20	2729.48	2085.14	18.69	7.58	7.22
I12	356	181.20	0.63	0.32	0.98	2666.22	2038.64	18.88	8.03	7.60
I13	357	181.20	0.51	0.32	0.80	2589.77	1982.45	19.08	8.60	8.93
I14	358	181.20	0.42	0.32	0.66	2499.86	1916.37	19.27	9.30	10.80
I15	359	181.20	0.35	0.32	0.55	2395.23	1839.46	19.46	10.14	12.89
I16	364	90.46	0.27	0.32	0.42	2207.52	1701.50	19.71	5.86	6.90
I17	365	305.06	0.85	0.32	1.33	2757.10	2105.44	18.60	12.43	11.65
I18	366	305.06	0.74	0.32	1.16	2719.06	2077.48	18.73	12.88	12.73
I19	367	305.06	0.64	0.32	1.00	2672.63	2043.36	18.86	13.44	14.70
I20	369	305.06	0.47	0.32	0.74	2556.10	1957.70	19.16	14.91	18.57
I21	371	305.06	0.39	0.32	0.62	2466.62	1891.93	19.34	16.09	21.44
I22	372	305.06	0.55	0.32	0.86	2618.29	2003.42	19.01	14.12	15.70
I23	373	305.06	0.85	0.48	0.88	2875.60	2192.54	18.11	9.18	7.00
I24	374	305.06	0.74	0.48	0.77	2837.12	2164.25	18.29	9.56	7.60
I25	375	305.06	0.64	0.48	0.66	2789.83	2129.49	18.48	10.04	9.04
I26	376	305.06	0.55	0.48	0.57	2733.61	2088.17	18.68	10.62	9.41
I27	377	305.06	0.47	0.48	0.49	2669.33	2040.93	18.87	11.31	10.92

Flame #	Photo #	Q_{O2} (ccm)	X_{O2}	X_{CH4}	S	T_{ad} (K)	T_{char} (K)	D_{Char} (mm^2/s)	$L_{St,model}$ (mm)	$L_{St,meas}$ (mm)
I28	378	305.06	0.39	0.48	0.41	2578.76	1974.36	19.11	12.31	12.76
I29	379	305.06	0.74	0.67	0.55	2902.52	2212.33	17.98	7.75	6.47
I30	380	305.06	0.64	0.67	0.48	2854.25	2176.84	18.21	8.18	7.37
I31	381	305.06	0.55	0.67	0.41	2797.90	2135.43	18.45	8.70	8.15
I32	382	305.06	0.47	0.67	0.35	2732.65	2087.47	18.68	9.32	9.36
I33	383	305.06	0.39	0.67	0.30	2640.30	2019.59	18.95	10.22	11.15
I34	387	305.06	0.51	0.67	0.38	2763.31	2110.01	18.58	9.03	8.38
I35	388	305.06	0.46	0.67	0.34	2714.26	2073.95	18.74	9.50	9.36
I36	389	305.06	0.41	0.67	0.31	2666.56	2038.89	18.88	9.96	10.32
I37	390	305.06	0.38	0.67	0.29	2620.24	2004.85	19.01	10.43	11.48
I38	391	305.06	0.35	0.67	0.26	2575.07	1971.65	19.11	10.89	12.28
I39	392	305.06	0.33	0.67	0.25	2530.76	1939.08	19.21	11.36	13.34
I40	393	305.06	0.31	0.67	0.23	2487.06	1906.96	19.30	11.82	13.89
I41	394	305.06	0.29	0.67	0.22	2443.88	1875.22	19.38	12.29	14.95
I42	395	305.06	0.41	0.48	0.44	2602.25	1991.62	19.05	12.10	12.11
I43	396	305.06	0.38	0.48	0.40	2556.60	1958.07	19.16	12.62	13.54
I44	397	305.06	0.35	0.48	0.37	2511.69	1925.06	19.25	13.14	14.45
I45	398	305.06	0.33	0.48	0.34	2467.35	1892.47	19.34	13.67	15.70
I46	399	305.06	0.32	0.48	0.33	2445.36	1876.31	19.37	13.93	16.11
I47	400	305.06	0.31	0.48	0.32	2423.50	1860.24	19.41	14.19	16.99
I48	403	305.06	0.41	0.28	0.73	2452.72	1881.72	19.36	17.08	17.46
I49	404	305.06	0.38	0.28	0.67	2406.98	1848.10	19.44	17.73	18.64
I50	405	305.06	0.35	0.28	0.62	2361.77	1814.87	19.51	18.38	21.17
I51	406	305.06	0.33	0.28	0.58	2317.21	1782.12	19.57	19.03	21.57
I52	410	305.06	0.51	1.00	0.25	2819.08	2150.99	18.37	7.27	7.27
I53	411	305.06	0.46	1.00	0.23	2769.74	2114.73	18.56	7.68	8.95
I54	412	305.06	0.41	1.00	0.21	2721.26	2079.10	18.72	8.10	9.66
I55	413	305.06	0.35	1.00	0.18	2628.26	2010.74	18.98	8.92	12.64

Flame #	Photo #	Q_{O2} (ccm)	X_{O2}	X_{CH4}	S	T_{ad} (K)	T_{char} (K)	D_{Char} (mm^2/s)	$L_{St,model}$ (mm)	$L_{St,meas}$ (mm)
I56	415	305.06	0.31	1.00	0.15	2539.90	1945.79	19.19	9.74	13.57
I57	416	305.06	0.29	1.00	0.14	2496.83	1914.14	19.28	10.15	14.47
I58	417	406.04	0.48	1.00	0.24	2799.37	2136.50	18.44	9.90	9.98
I59	419	406.04	0.42	1.00	0.21	2727.80	2083.90	18.70	10.70	11.84
I60	421	406.04	0.37	1.00	0.19	2659.38	2033.61	18.90	11.50	15.30
I61	422	406.04	0.35	1.00	0.18	2626.45	2009.41	18.99	11.89	16.18
I62	423	406.04	0.33	1.00	0.17	2594.28	1985.77	19.07	12.29	17.71
I63	424	406.04	0.58	0.67	0.43	2817.25	2149.65	18.37	11.35	9.56
I64	425	406.04	0.48	0.67	0.36	2743.65	2095.55	18.65	12.27	12.17
I65	426	406.04	0.42	0.67	0.31	2672.98	2043.61	18.86	13.18	14.37
I66	427	406.04	0.37	0.67	0.28	2605.79	1994.22	19.04	14.08	16.91
I67	428	406.04	0.33	0.67	0.25	2541.36	1946.87	19.19	14.97	18.51
I68	429	406.04	0.58	0.48	0.61	2750.40	2100.51	18.62	13.97	11.46
I69	430	406.04	0.48	0.48	0.51	2677.69	2047.07	18.85	15.00	14.12
I70	431	406.04	0.42	0.48	0.44	2608.55	1996.25	19.03	16.01	17.01
I71	432	406.04	0.37	0.48	0.39	2542.27	1947.54	19.19	17.02	18.74
I72	433	406.04	0.33	0.48	0.35	2477.98	1900.29	19.32	18.02	21.62
I73	434	406.04	0.58	0.28	1.02	2596.87	1987.67	19.06	20.13	17.98
I74	435	406.04	0.48	0.28	0.85	2527.00	1936.31	19.22	21.37	21.17
I75	436	406.04	0.42	0.28	0.74	2459.00	1886.33	19.35	22.62	23.93
I76	437	406.04	0.37	0.28	0.65	2392.56	1837.50	19.46	23.87	26.74
I77	439	406.04	0.33	0.28	0.59	2327.87	1789.96	19.56	25.12	29.62
I78	440	406.04	0.32	0.48	0.33	2446.45	1877.11	19.37	18.52	22.27
I79	443	406.04	0.30	0.67	0.23	2478.92	1900.97	19.31	15.85	19.54
I80	444	406.04	0.30	1.00	0.15	2531.76	1939.82	19.21	13.07	18.44
I81	449	406.04	1.00	0.28	1.76	2755.73	2104.43	18.60	17.45	12.08
I82	450	305.06	1.00	0.28	1.76	2755.73	2104.43	18.60	13.11	9.21
I83	451	305.06	0.77	0.28	1.36	2691.36	2057.12	18.81	13.90	10.67

Flame #	Photo #	Q_{O2} (ccm)	X_{O2}	X_{CH4}	S	T_{ad} (K)	T_{char} (K)	D_{Char} (mm^2/s)	$L_{St,model}$ (mm)	$L_{St,meas}$ (mm)
I84	452	406.04	0.82	0.28	1.44	2707.25	2068.80	18.76	18.24	13.74
I85	453	406.04	0.82	0.20	2.06	2547.61	1951.46	19.18	24.65	20.28
I86	454	305.06	0.77	0.20	1.94	2532.30	1940.21	19.21	18.75	16.10
I87	455	305.06	1.00	0.20	2.51	2593.98	1985.55	19.07	17.82	13.43
I88	456	406.04	1.00	0.20	2.51	2593.98	1985.55	19.07	23.72	17.94
I89	459	305.06	1.00	0.13	3.86	2307.28	1774.82	19.59	27.28	24.38
I90	460	406.04	1.00	0.13	3.86	2307.28	1774.82	19.59	36.31	32.38
I91	461	406.04	0.82	0.13	3.17	2260.98	1740.79	19.65	37.53	35.47
I92	462	305.06	0.77	0.13	2.99	2245.74	1729.59	19.66	28.50	27.19
I93	463	305.06	1.00	0.12	4.29	2217.71	1708.99	19.70	30.57	28.86
I94	464	406.04	1.00	0.12	4.29	2217.71	1708.99	19.70	40.68	34.72
I95	466	305.06	1.00	0.10	4.99	2075.69	1604.60	19.85	36.31	35.22
I96	467	406.04	1.00	0.10	4.99	2075.69	1604.60	19.85	48.33	44.97

Table D-3: Information of the propane NDFs.

Flame #	Photo #	Q_{O2} (ccm)	X_{O2}	X_{CH4}	S	T_{ad} (K)	T_{char} (K)	D_{Char} (mm^2/s)	$L_{St,model}$ (mm)	$L_{St,meas}$ (mm)
N1	192	62.96	0.14	0.41	1.72	2491.46	1910.19	14.93	25.16	22.53
N2	194	47.50	0.11	0.41	1.34	2408.24	1849.02	13.77	22.18	21.13
N3	195	47.50	0.09	0.41	1.06	2306.29	1774.09	13.96	23.86	24.21
N4	196	47.50	0.11	0.48	1.15	2483.78	1904.55	13.59	19.52	18.18
N5	197	47.50	0.11	0.55	1.00	2538.95	1945.09	13.44	17.61	16.41
N6	198	47.50	0.11	0.66	0.83	2600.81	1990.56	13.25	15.48	14.56
N7	199	47.50	0.11	0.30	1.82	2225.00	1714.34	14.09	29.00	27.16
N8	200	47.50	0.11	0.36	1.52	2340.04	1798.90	13.90	24.64	23.06
N9	201	47.50	0.15	0.41	1.88	2516.24	1928.41	13.51	20.50	16.12
N10	203	145.62	0.11	0.37	1.41	2348.77	1805.32	13.88	68.51	64.14
N11	206	145.62	0.12	0.37	1.56	2386.42	1832.99	13.81	66.78	62.78
N12	208	145.62	0.10	0.47	1.02	2430.74	1865.56	13.72	58.00	57.62
N13	209	145.62	0.11	0.47	1.17	2485.45	1905.78	13.59	55.75	52.46
N14	210	145.62	0.11	0.47	1.17	2485.45	1905.78	13.59	55.75	52.22
N15	212	145.62	0.13	0.47	1.38	2541.97	1947.32	13.43	53.50	48.61
N16	231	17.63	1.00	0.17	29.99	2019.21	1563.09	14.37	16.41	14.01
N17	234	20.55	0.34	0.19	9.00	2082.04	1609.27	14.29	17.22	12.51
N18	237	14.72	0.39	0.19	10.39	2097.84	1620.88	14.27	12.20	13.56
N19	238	26.44	0.46	0.19	12.20	2112.55	1631.69	14.25	21.71	15.05
N20	239	20.55	0.48	0.19	12.55	2114.92	1633.44	14.25	16.85	13.69
N21	240	20.55	0.57	0.19	15.05	2128.68	1643.55	14.23	16.70	12.73
N22	243	20.55	0.40	0.21	9.36	2220.57	1711.09	14.10	14.80	11.30

Table D-4: Information of the propane IDFs.

Flame #	Photo #	Q_{O2} (ccm)	X_{O2}	X_{CH4}	S	T_{ad} (K)	T_{char} (K)	D_{Char} (mm^2/s)	$L_{St,model}$ (mm)	$L_{St,meas}$ (mm)
I1	213	181.20	0.27	0.39	0.14	2406.95	1848.08	15.00	8.44	11.44
I2	214	181.20	0.30	0.39	0.16	2507.83	1922.22	13.53	8.42	10.15
I3	215	181.20	0.37	0.39	0.19	2625.68	2008.84	13.16	7.55	8.54
I4	216	181.20	0.45	0.39	0.23	2730.01	2085.53	12.74	6.85	6.47
I5	217	181.20	0.45	0.39	0.23	2730.01	2085.53	12.74	6.85	6.36
I6	218	181.20	0.45	0.26	0.35	2674.04	2044.39	12.98	8.41	8.22
I7	219	181.20	0.39	0.26	0.30	2599.06	1989.28	13.25	9.00	9.55
I8	220	181.20	0.34	0.26	0.26	2515.42	1927.80	13.51	9.68	11.14
I9	221	181.20	0.28	0.26	0.22	2387.17	1833.54	13.81	10.78	12.91
I10	222	260.10	0.34	0.26	0.27	2527.09	1936.38	13.48	13.76	16.21
I11	223	260.10	0.34	0.26	0.27	2527.09	1936.38	13.48	13.76	16.30
I12	224	260.10	0.42	0.26	0.33	2638.78	2018.47	13.11	12.46	13.27
I13	247	147.28	0.32	0.38	0.17	2615.60	2001.44	13.43	6.57	6.86
I14	248	147.28	0.32	0.23	0.28	2251.37	1733.72	13.62	9.09	7.40
I15	249	147.28	0.32	0.57	0.11	2579.09	1974.60	13.32	5.63	6.64
I16	250	147.28	0.32	0.72	0.09	2594.19	1985.70	13.27	5.15	6.36
I17	251	147.28	0.32	1.00	0.06	2610.18	1997.45	13.22	4.59	6.09

Appendix E. Photo Images of Flames in Fig.3-6

Appendix E-1: Photo images of the methane diffusion flames. The corresponding flame information can be found at Table D-1 and Table D-2.

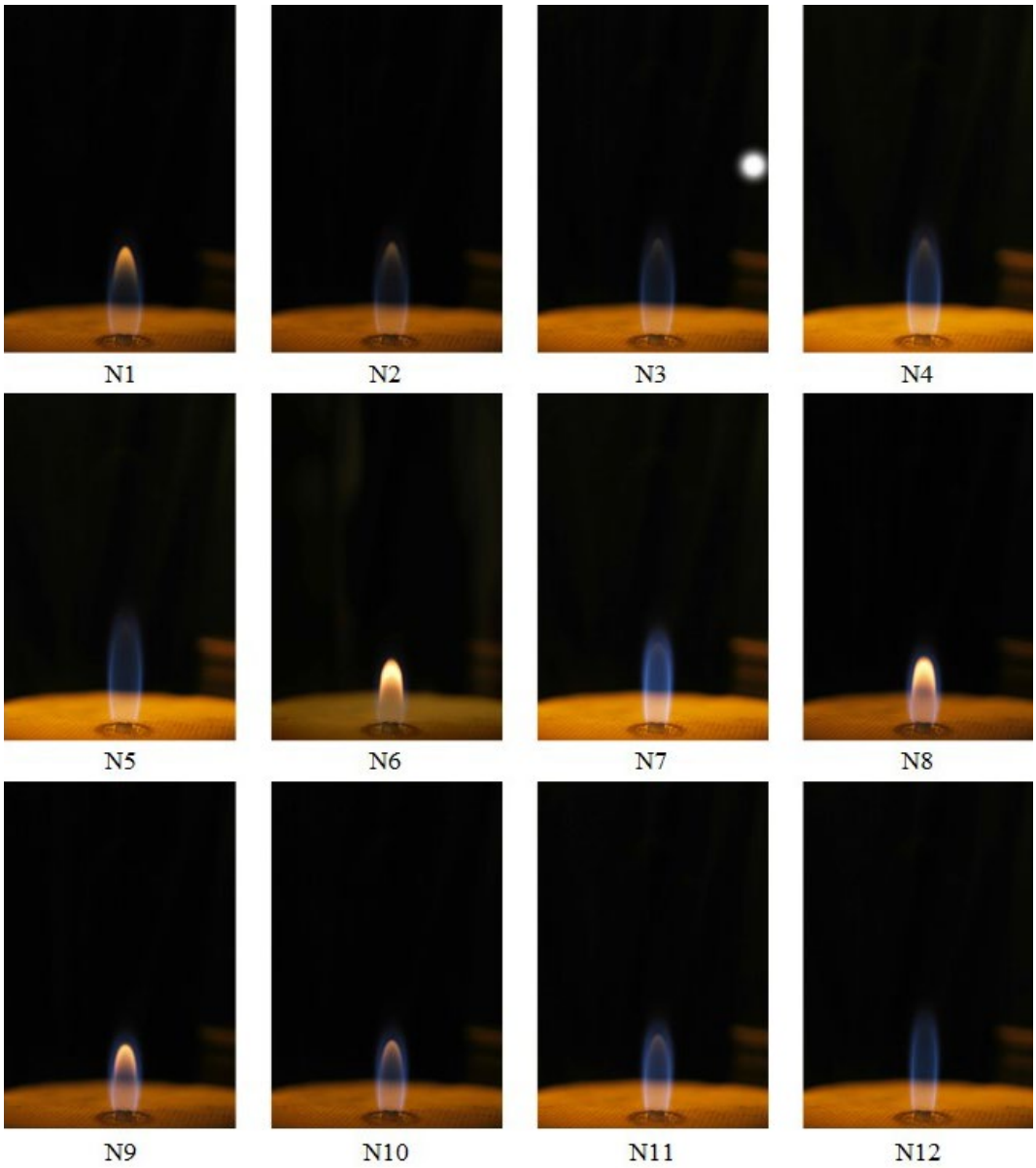

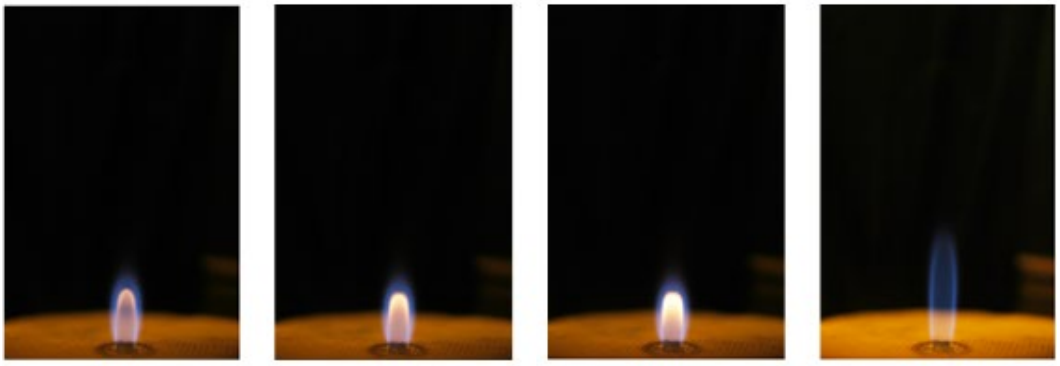

N13 N14 N15 N16

N17 N18 N19 N20

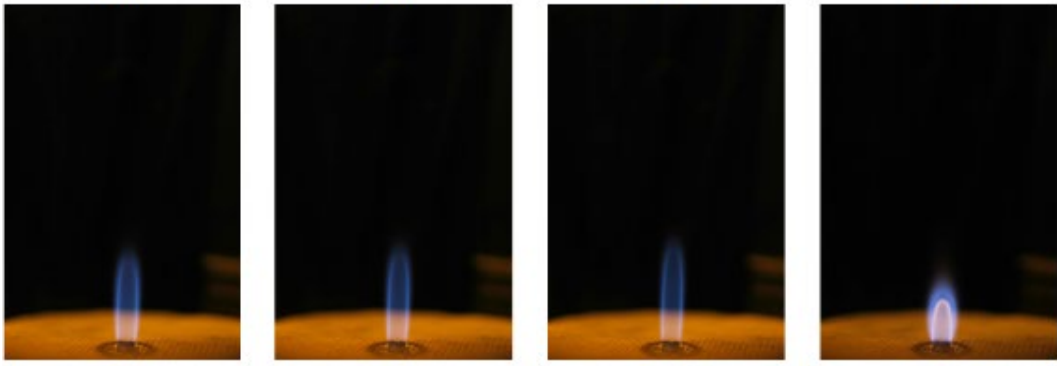

N21 N22 N23 N24

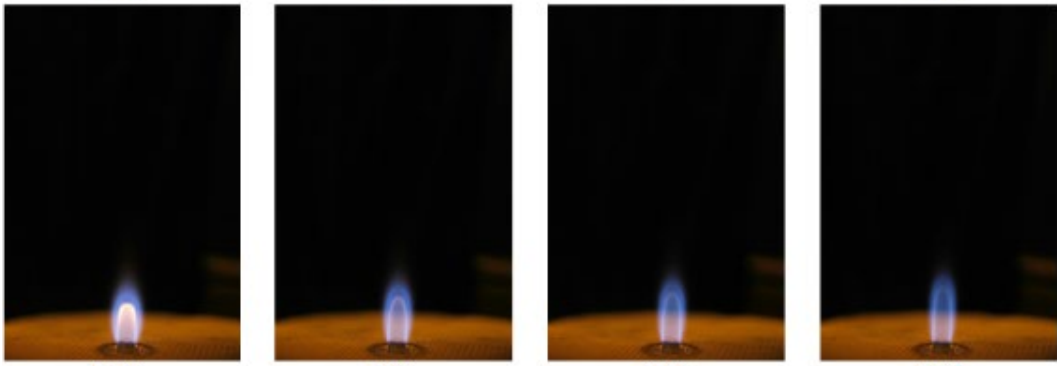

N25 N26 N27 N28

N29

N30

N31

N32

N33

N34

N35

N36

N37

N38

N39

N40

N41

N42

N43

N44


N45


N46


N47


N48


N49


N50


N51


N52


N53


N54


N55


N56


N57


N58


N59


N60


N61


N62


N63


N64


N65


N66


N67


N68


N69


N70


N71


N72


N73


N74


N75


N76


N77


N78


N79


N80


N81


N82


N83


N84


N85


N86


N87


N88


N89


N90


N91


N92


N93


N94


N95


N96


N97


N98


N99


N100


N101


N102


N103


N104


N105


N106


N107


N108


N109


N110


N111


N112


N113


N114


N115


N116


N117


N118


N119


N120


N121


N122


N123


N124


N125


N126


N127


N128


N129


N130


N131


N132


N133


N134


N135


N136


N137


N138


N139


N140

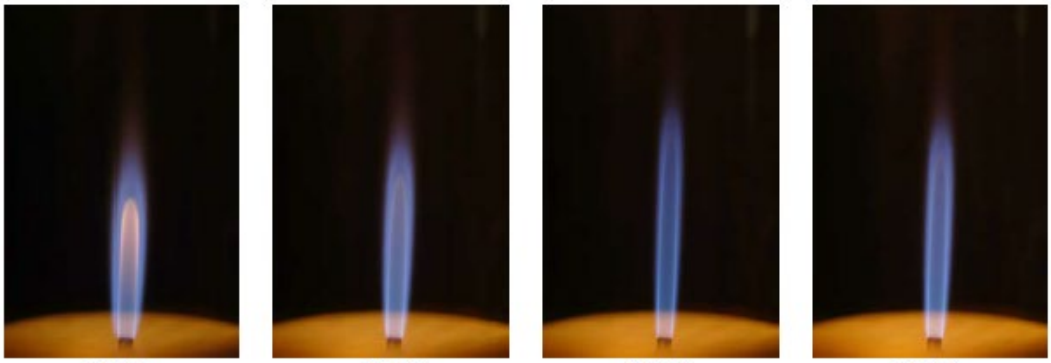

N141 N142 N143 N144

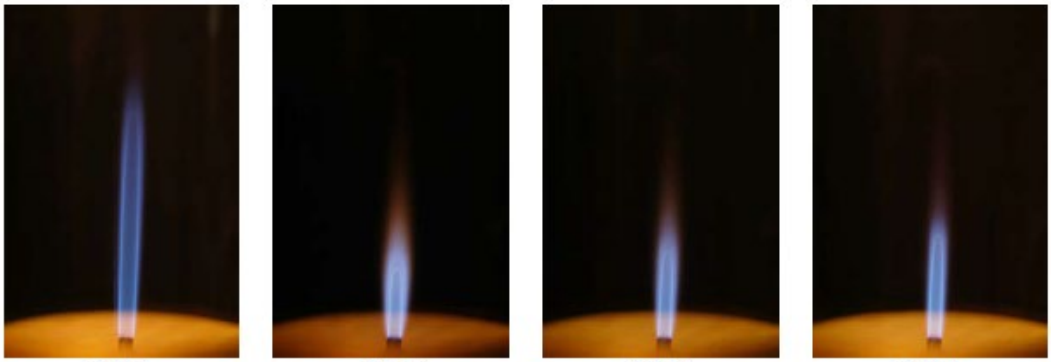

N145 N146 N147 N148

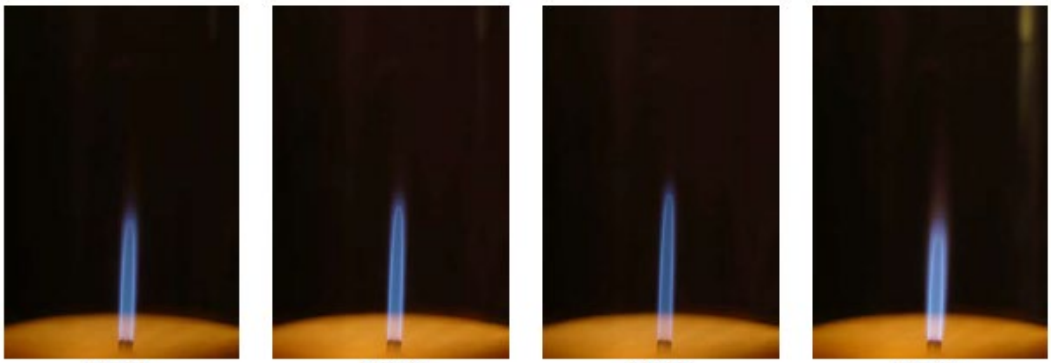

N149 N150 N151 N152

I1 I2 I3 I4

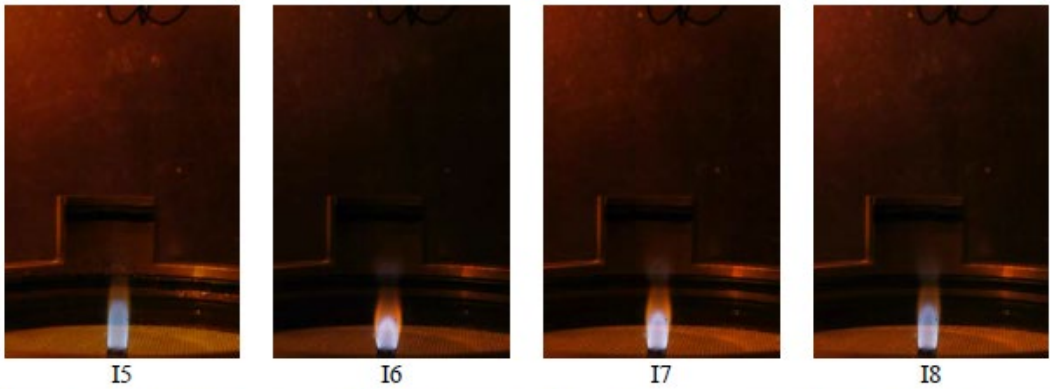

I5 I6 I7 I8

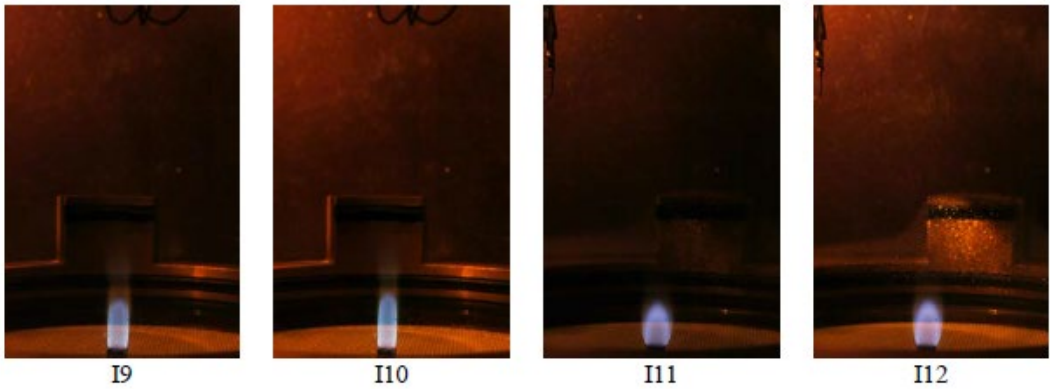

I9 I10 I11 I12

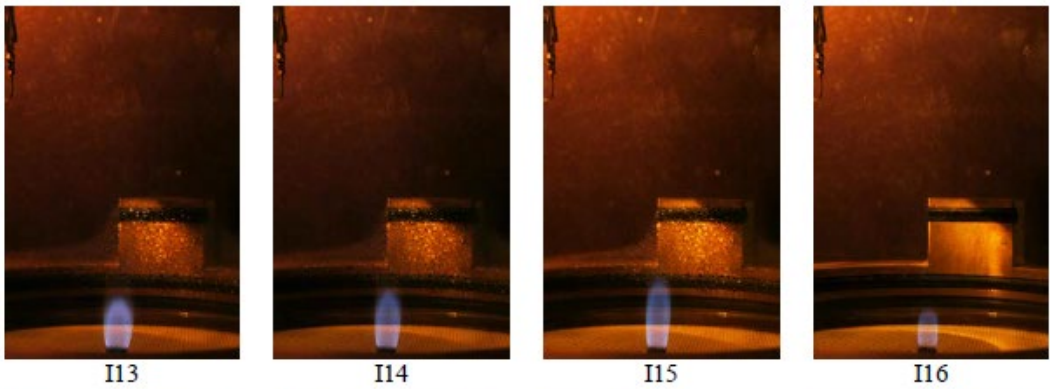

I13 I14 I15 I16

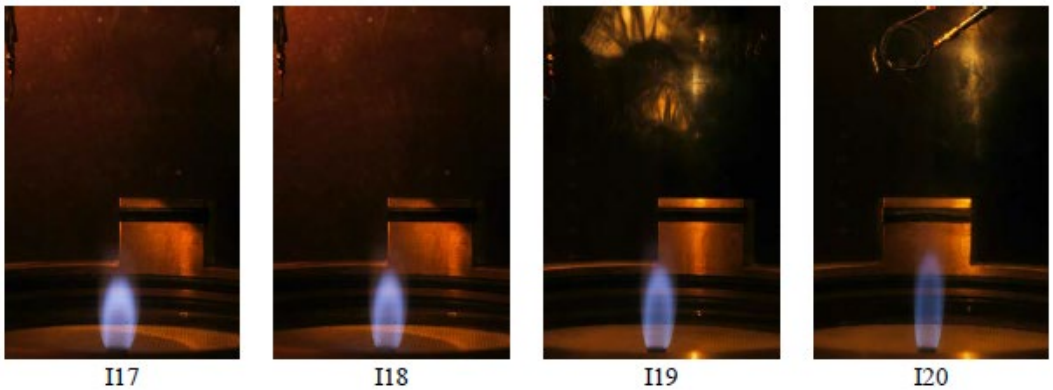

I17 I18 I19 I20


I21


I22


I23


I24


I25


I26


I27


I28


I29


I30


I31


I32


I33


I34


I35


I36

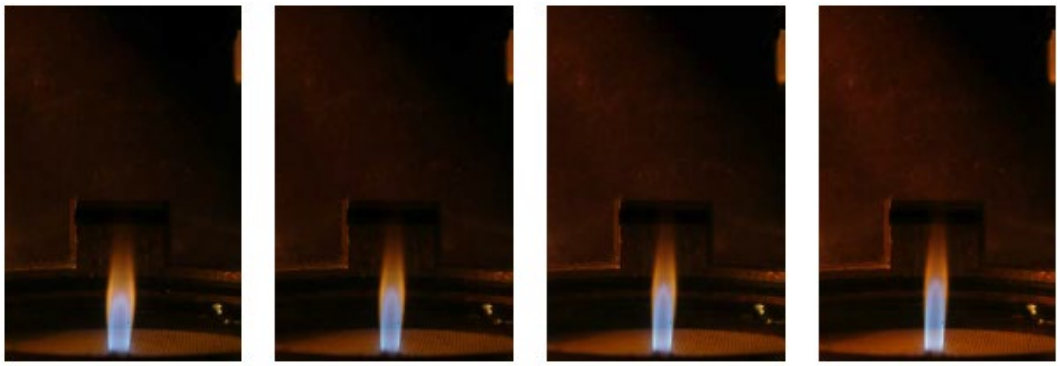

I37 I38 I39 I40

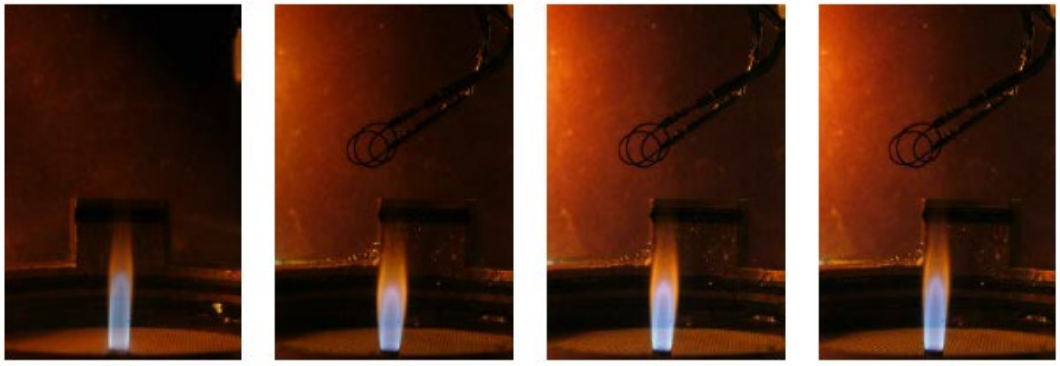

I41 I42 I43 I44

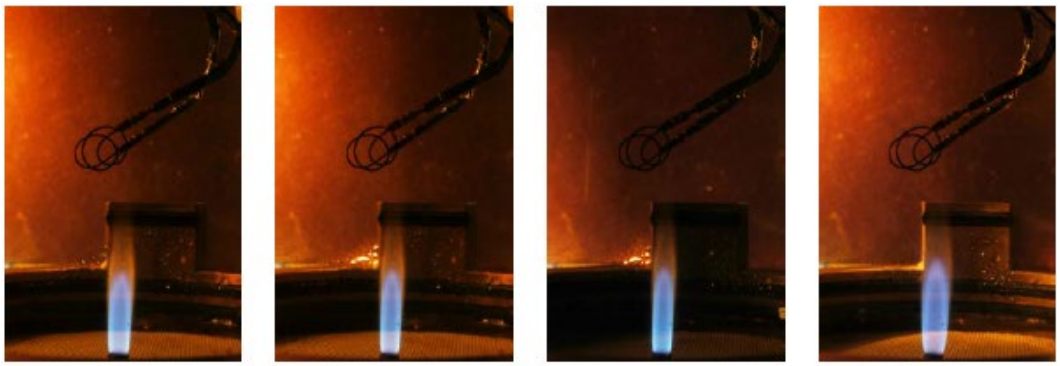

I45 I46 I47 I48

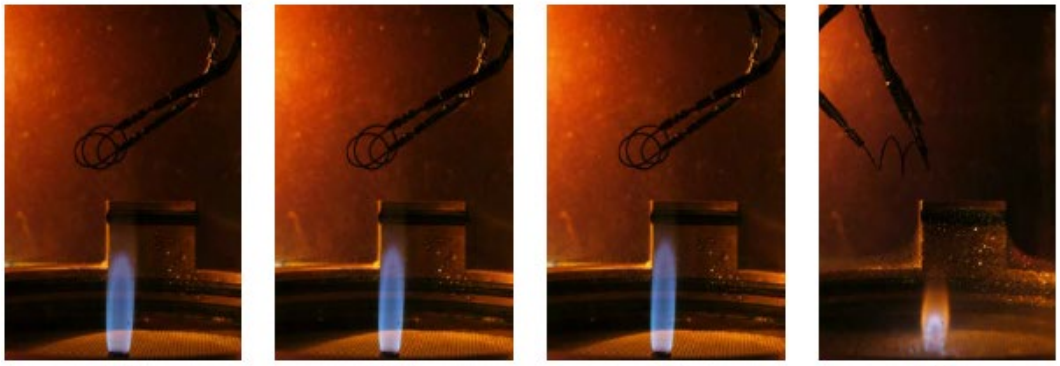

I49 I50 I51 I52


I53


I54


I55


I56


I57


I58


I59


I60


I61


I62


I63


I64


I65


I66


I67


I68


I69


I70

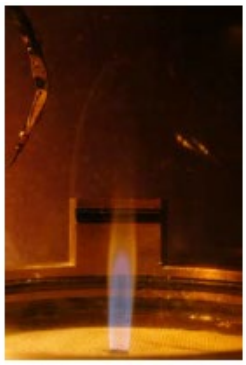
I71


I72


I73

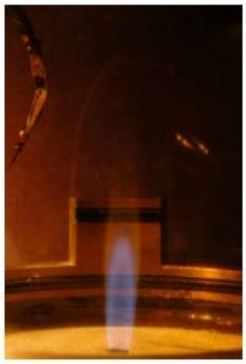
I74


I75


I76

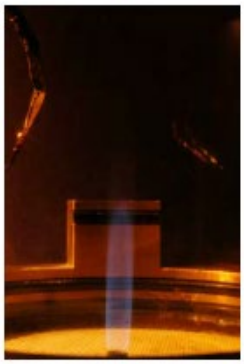
I77


I78


I79


I80


I81


I82


I83


I84


I85


I86


I87


I88

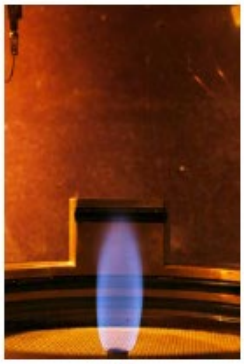
I89


I90


I91


I92

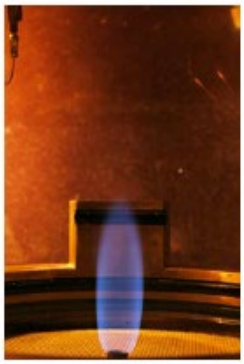
I93


I94


I95


I96

Appendix E-2: Photo images of the propane diffusion flames. The corresponding flame information can be found at Table D-3 and Table D-4.

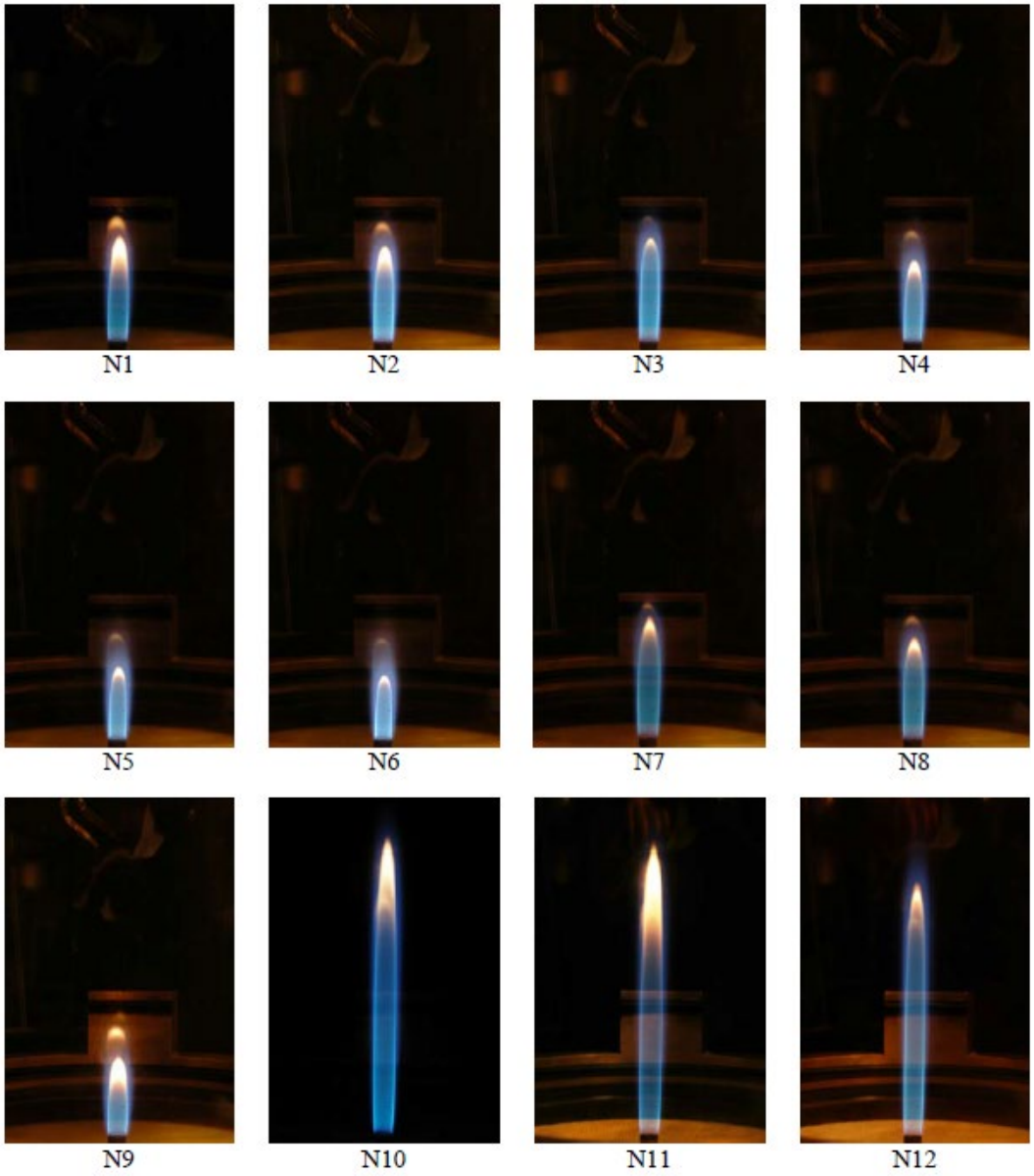


N13


N14


N15


N16


N17


N18


N19


N20


N21


N22


I1


I2


I3


I4


I5


I6


I7


I8


I9


I10


I11


I12


I13


I14


I15


I16


I17

Chapter 8 List of Contribution During Ph. D

Peer-Reviewed Articles

- **Z. Wang**, P.B. Sunderland, R.L. Axelbaum. Dilution Effects on Laminar Jet Diffusion Flame Lengths. Proceedings of the Combustion Institute. 2019 37 1547-1553
- W. Gan, C. Chen, **Z. Wang,** J. Song, Y. Kuang, S. He, R. Mi, P. B. Sunderland, L. Hu, Dense, Self-Formed Char Layer Enables Fire-Retardant Wood Structural Material, Advanced Functional Materials. 2019 1807444 (Co-first author)
- **Z. Wang**, P.B. Sunderland, R.L. Axelbaum. Double Blue Zones in Laminar Jet Diffusion Flames, submitted to Combustion and flame. (In preparation)
- W. Gan, C. Chen, **Z. Wang**, Y. Pei, W. Ping, S. Xiao, J. Dai, Y. Yao, S. He, B. Yang, P. B. Sunderland, L. Hu Fire-Resistant Wood Enabled by an Anisotropic Thermally Conductive Hexagonal Boron Nitride Coating, Materials Today, (Submitted as co-first author)

Conference Presentation or Poster

- Z. Wang, Double Blue Zones in Inverse and Normal Laminar Jet Diffusion Flames. US National Combustion Meeting, Pasadena, CA, 2019.
- Z. Wang, Double Luminous Zones in LaminarJet Diffusion Flames. ASGSR, North Bethesda, MD, 2018
- Z. Wang, Double Blue Zones in Inverse Laminar Jet Diffusion Flames. 37th International Symposium on Combustion, Dublin, Ireland, 2018
- Z. Wang, Dilution Effects on Laminar Jet Diffusion Flame Lengths. 37th International Symposium on Combustion, Dublin, Ireland, 2018
- Z. Wang, Double Luminous Zones in Inverse Laminar Jet Diffusion Flames. Eastern States Section of the Combustion Institute, State College, PA, 2018.
- Z. Wang, Observations of Double Flames in Inverse Gas Jet Diffusion Flames, US National Combustion Meeting, College Park, MD 2017
- Z. Wang, Effects of Nitrogen Addition on Lengths of Laminar Jet Diffusion Flames. US National Combustion Meeting, College Park, MD, 2017.
- Z. Wang, The Effects of Reactant Dilution on Lengths of Laminar Jet Diffusion Flames, ASGSR, Cleveland, OH, 2016

Chapter 9 Bibliography

[1] Ju, Y., 2014. Recent progress and challenges in fundamental combustion research. Advances in Mechanics, 44(20), p.201402.

[2] Finegan, D.P., Scheel, M., Robinson, J.B., Tjaden, B., Hunt, I., Mason, T.J., Millichamp, J., Di Michiel, M., Offer, G.J., Hinds, G. and Brett, D.J., 2015. In-operando high-speed tomography of lithium-ion batteries during thermal runaway. Nature communications, 6, p.6924.

[3] Liu, X., Stoliarov, S.I., Denlinger, M., Masias, A. and Snyder, K., 2015. Comprehensive calorimetry of the thermally-induced failure of a lithium ion battery. Journal of Power Sources, 280, pp.516-525.

[4] Kong, L., Li, C., Jiang, J. and Pecht, M., 2018. Li-ion battery fire hazards and safety strategies. *Energies*, *11*(9), p.2191.

[5] Cao, S., Ma, B., Bennett, B.A.V., Giassi, D., Stocker, D.P., Takahashi, F., Long, M.B. and Smooke, M.D., 2015. A computational and experimental study of coflow laminar methane/air diffusion flames: Effects of fuel dilution, inlet velocity, and gravity. Proceedings of the Combustion Institute, 35(1), pp.897-903.

[6] Urban, D.L., Yuan, Z.G., Sunderland, P.B., Linteris, G.T., Voss, J.E., Lin, K.C., Dai, Z., Sun, K. and Faeth, G.M., 1998. Structure and soot properties of nonbuoyant ethylene/air laminar jet diffusion flames. AIAA journal, 36(8), pp.1346-1360.

[7] Lin, K.C., Faeth, G.M., Sunderland, P.B., Urban, D.L. and Yuan, Z.G., 1999. Shapes of nonbuoyant round luminous hydrocarbon/air laminar jet diffusion flames. Combustion and Flame, 116(3), pp.415-431.

[8] Aalburg, C., Diez, F.J., Faeth, G.M., Sunderland, P.B., Urban, D.L. and Yuan, Z.G., 2005. Shapes of nonbuoyant round hydrocarbon-fueled laminar-jet diffusion flames in still air. Combustion and Flame, 142(1-2), pp.1-16.

[9] Burke, S.P. and Schumann, T.E.W., 1928. Diffusion flames. Industrial & Engineering Chemistry, 20(10), pp.998-1004.

[10] Roper, F.G., 1977. The prediction of laminar jet diffusion flame sizes: Part I. Theoretical model. Combustion and Flame, 29, pp.219-226.

[11] Sunderland, P.B., Mendelson, B.J., Yuan, Z.G. and Urban, D.L., 1999. Shapes of buoyant and nonbuoyant laminar jet diffusion flames. *Combustion and Flame*, *116*(3), pp.376-386.

[12] Durox, D., Yuan, T., Baillot, F. and Most, J.M., 1995. Premixed and diffusion flames in a centrifuge. *Combustion and flame*, *102*(4), pp.501-511.

[13] Sunderland, P.B., Krishnan, S.S. and Gore, J.P., 2004. Effects of oxygen enhancement and gravity on normal and inverse laminar jet diffusion flames. *Combustion and flame*, *136*(1-2), pp.254-256.

[14] Sunderland, P.B., Haylett, J.E., Urban, D.L. and Nayagam, V., 2008. Lengths of laminar jet diffusion flames under elevated gravity. *Combustion and Flame*, *152*(1-2), pp.60-68.

[15] Spalding, D.B., 2013. *Combustion and mass transfer: a textbook with multiple-choice exercises for engineering students*. Elsevier.

[16] Min, J., Baillot, F., Guo, H., Domingues, E., Talbaut, M. and Patte-Rouland, B., 2011. Impact of CO2, N2 or Ar diluted in air on the length and lifting behavior of a laminar diffusion flame. *Proceedings of the Combustion Institute*, *33*(1), pp.1071-1078.

[17] Saito, K., Williams, F.A. and Gordon, A.S., 1986. Structure of Laminar Coflow Methane–Air Diffusion Flames. *Journal of heat transfer*, *108*(3), pp.640-648.

[18] Gordon, A.S., Li, S.C. and Williams, F.A., 1999. Visible flame heights of laminar coflow diffusion flames. *Combustion science and technology*, *141*(1-6), pp.1-18.

[19] Mikofski, M.A., Williams, T.C., Shaddix, C.R. and Blevins, L.G., 2006. Flame height measurement of laminar inverse diffusion flames. *Combustion and Flame*, *146*(1-2), pp.63-72.

[20] Roper, F.G., Smith, C. and Cunningham, A.C., 1977. The prediction of laminar jet diffusion flame sizes: Part II. Experimental verification. *Combustion and Flame*, *29*, pp.227-234.

[21] Wu, K.T. and Essenhigh, R.H., 1985, January. Mapping and structure of inverse diffusion flames of methane. In *Symposium (International) on Combustion* (Vol. 20, No. 1, pp. 1925-1932). Elsevier.

[22] McENALLY, C.S. and Pfefferle, L.D., 2000. The effect of nitrogen dilution on nonfuel hydrocarbons in laminar nonpremixed flames. *Combustion science and technology*, *151*(1), pp.133-155.

[23] Mitchell, R.E., Sarofim, A.F. and Clomburg, L.A., 1980. Experimental and numerical investigation of confined laminar diffusion flames. *Combustion and flame*, *37*, pp.227-244.

[24] Hottel, H.C. and Hawthorne, W.R., 1948, January. Diffusion in laminar flame jets. In *Symposium on Combustion and Flame, and Explosion Phenomena* (Vol. 3, No. 1, pp. 254-266). Elsevier.

[25] Melvin, A., Moss, J.B. and Clarke, J.F., 1971. The structure of a reaction-broadened diffusion flame. *Combustion Science and Technology*, *4*(1), pp.17-30.

[26] Schug, K.P., Manheimer-Timnat, Y., Yaccarino, P. and Glassman, I., 1980. Sooting behavior of gaseous hydrocarbon diffusion flames and the influence of additives. *Combustion Science and Technology*, *22*(5-6), pp.235-250

[27] Axelbaum, R.L. and Law, C.K., 1991, January. Soot formation and inert addition in diffusion flames. In *Symposium (International) on Combustion* (Vol. 23, No. 1, pp. 1517-1523). Elsevier.

[28] Glassman, I., 1998, January. Sooting laminar diffusion flames: Effect of dilution, additives, pressure, and microgravity. In *Symposium (International) on Combustion* (Vol. 27, No. 1, pp. 1589-1596). Elsevier.

[29] Lock, A., Briones, A.M., Aggarwal, S.K., Puri, I.K. and Hegde, U., 2007. Liftoff and extinction characteristics of fuel-and air-stream-diluted methane–air flames. *Combustion and flame*, *149*(4), pp.340-352.

[30] Xu, H., Liu, F., Sun, S., Zhao, Y., Meng, S. and Tang, W., 2017. Effects of H2O and CO2 diluted oxidizer on the structure and shape of laminar coflow syngas diffusion flames. *Combustion and Flame*, *177*, pp.67-78.

[31] Zebib, A., Williams, F.A. and Kassoy, D.R., 1975. Effects of kinetic mechanism on diffusion-controlled structure of hydrogen-halogen reaction zones. *Combustion Science and Technology*, *10*(1-2), pp.37-44.

[32] Walker, Flames in which air is introduced into a flammable gas rather than vice versa, *American Journal of Science.* 241 (1979) 192-200.

[33] Kent, J.H. and Wagner, H.G., 1984. A reversed coflowing laminar diffusion flame. *Zeitschrift für Physikalische Chemie*, *139*(139), pp.59-68.

[34] Sidebotham, G.W. and Glassman, I., 1992. Flame temperature, fuel structure, and fuel concentration effects on soot formation in inverse diffusion flames. *Combustion and flame*, *90*(3-4), pp.269-283.

[35] Unrau, C.J., Axelbaum, R.L., Biswas, P. and Fraundorf, P., 2007. Synthesis of single-walled carbon nanotubes in oxy-fuel inverse diffusion flames with online diagnostics. *Proceedings of the Combustion Institute*, *31*(2), pp.1865-1872.

[36] Kumfer, B.M., Skeen, S.A. and Axelbaum, R.L., 2008. Soot inception limits in laminar diffusion flames with application to oxy–fuel combustion. *Combustion and Flame*, *154*(3), pp.546-556

[37] Wang, B., Eri, Q., Li, T. and Duan, R., 2016, November. Experimental Investigation on the Effect of Oxygen Enhancement on Radiation Distribution in Inverse Diffusion Flames. In *ASME 2016 International Mechanical Engineering Congress and Exposition* (pp. V008T10A024-V008T10A024). American Society of Mechanical Engineers.

[38] Xu, F., Liu, X. and Stephen, D.T., 2006. Synthesis of carbon nanotubes on metal alloy substrates with voltage bias in methane inverse diffusion flames. *Carbon*, *44*(3), pp.570-577.

[39] Shaddix, C.R. and Williams, T.C., 2009. Measurements of the velocity field in laminar ethylene inverse jet diffusion flames. *Combustion and Flame*, *4*(156), pp.942-945.

[40] Stelzner, B., Hunger, F., Voss, S., Keller, J., Hasse, C. and Trimis, D., 2013. Experimental and numerical study of rich inverse diffusion flame structure. *Proceedings of the Combustion Institute*, *34*(1), pp.1045-1055.

[41] Sunderland, P.B., Axelbaum, R.L., Urban, D.L., Chao, B.H. and Liu, S., 2003. Effects of structure and hydrodynamics on the sooting behavior of spherical microgravity diffusion flames. *Combustion and Flame*, *132*(1-2), pp.25-33.

[42] Sunderland, P.B., Urban, D.L., Stocker, D.P., Chao, B.H. and AXELBAUM∗, R.L., 2004. Sooting limits of microgravity spherical diffusion flames in oxygen-enriched air and diluted fuel. *Combustion science and technology*, *176*(12), pp.2143-2164.

[43] Joo, H.I. and Gülder, Ö.L., 2010. Soot formation and temperature structure in small methane–oxygen diffusion flames at subcritical and supercritical pressures. *Combustion and Flame*, *157*(6), pp.1194-1201.

[44] Joo, P.H., Charest, M.R., Groth, C.P. and Gülder, Ö.L., 2013. Comparison of structures of laminar methane–oxygen and methane–air diffusion flames from atmospheric to 60 atm. *Combustion and Flame*, *160*(10), pp.1990-1998.

[45] Liu, F., Karataş, A.E., Gülder, Ö.L. and Gu, M., 2015. Numerical and experimental study of the influence of CO2 and N2 dilution on soot formation in laminar coflow C2H4/air diffusion flames at pressures between 5 and 20 atm. *Combustion and Flame*, *162*(5), pp.2231-2247.

[46] Weinberg, F. and Carleton, F., 2009. Ionization and chemiluminescence during the progressive aeration of methane flames. *Combustion and Flame*, *156*(12), pp.2276-2284.

[47] Weinberg, F., Carleton, F., Houdmont, R., Dunn-Rankin, D. and Karnani, S., 2011. Syngas formation in methane flames and carbon monoxide release during quenching. *Combustion and Flame*, *158*(2), pp.273-280.

[48] Sung, C.J., Zhu, D.L. and Law, C.K., 1998, January. On micro-buoyancy spherical diffusion flames and a double luminous zone structure of the hydrogen/methane flame. In *Symposium (International) on Combustion* (Vol. 27, No. 2, pp. 2559-2566). Elsevier.

[49] Yan, W., Zhou, H., Jiang, Z., Lou, C., Zhang, X. and Chen, D., 2013. Experiments on measurement of temperature and emissivity of municipal solid waste (MSW) combustion by spectral analysis and image processing in visible spectrum. *Energy & Fuels*, *27*(11), pp.6754-6762.

[50] García-Armingol, T., Hardalupas, Y., Taylor, A.M.K.P. and Ballester, J., 2014. Effect of local flame properties on chemiluminescence-based stoichiometry measurement. *Experimental Thermal and Fluid Science*, *53*, pp.93-103.

[51] Giassi, D., Cao, S., Bennett, B. A. V., Stocker, D. P., Takahashi, F., Smooke, M. D., and Long, M. B. (2016). Analysis of CH* concentration and flame heat release rate in laminar coflow diffusion flames under microgravity and normal gravity. Combustion and Flame, 167, 198-206.

[52] Guiberti, T.F., Durox, D. and Schuller, T., 2017. Flame chemiluminescence from CO2-and N2-diluted laminar CH4/air premixed flames. Combustion and Flame, 181, pp.110-122.

[53] Merotto, L., Sirignano, M., Commodo, M., D'Anna, A., Dondè, R., and De Iuliis, S. (2017). Experimental characterization and modeling for equivalence ratio sensing in non-premixed flames using chemiluminescence and laser-induced breakdown spectroscopy techniques. Energy and Fuels, 31(3), 3227-3233.

[54] Wang, K., Li, F., Wu, Y. and Yu, X., 2018. Quantitative Measurements of Chemiluminescence in a Laminar Methane–Air Premixed Flame and Comparison to Numerical Methods. Energy and Fuels, 32(4), pp.5536-5543.

[55] Samaniego, J.M., Egolfopoulos, F.N. and Bowman, C.T., 1995. CO2* chemiluminescence in premixed flames. Combustion Science and Technology, 109(1-6), pp.183-203.

[56] Kojima, J., Ikeda, Y. and Nakajima, T., 2000. Spatially resolved measurement of OH*, CH*, and C_2* chemiluminescence in the reaction zone of laminar methane/air premixed flames. Proceedings of the Combustion institute, 28(2), pp.1757-1764.

[57] Li, S.C., Gordon, A.S. and Williams, F.A., 1995. A simplified method for the computation of Burke-Schumann flames in infinite atmospheres. *Combustion Science and Technology*, *104*(1-3), pp.75-91.

[58] Lee, E.J., Oh, K.C. and Shin, H.D., 2005. Soot formation in inverse diffusion flames of diluted ethene. *Fuel*, *84*(5), pp.543-550.

[59] Jung, Y., Oh, K.C., Bae, C. and Shin, H.D., 2012. The effect of oxygen enrichment on incipient soot particles in inverse diffusion flames. *Fuel*, *102*, pp.199-207.

[60] Escudero, F., Fuentes, A., Demarco, R., Consalvi, J.L., Liu, F., Elicer-Cortés, J.C. and Fernandez-Pello, C., 2016. Effects of oxygen index on soot production and temperature in an ethylene inverse diffusion flame. *Experimental Thermal and Fluid Science*, *73*, pp.101-108.

[61] Lamige, S., Min, J., Galizzi, C., André, F., Baillot, F., Escudié, D. and Lyons, K.M., 2013. On preheating and dilution effects in non-premixed jet flame stabilization. *Combustion and Flame*, *160*(6), pp.1102-1111.

[62] Ahmed, P., Habib, M.A., Ben-Mansour, R. and Ghoniem, A.F., 2016. Computational Fluid Dynamics (CFD) Investigation of the Oxy-combustion Characteristics of Diesel Oil, Kerosene, and Heavy Oil Liquid Fuels in a Model Furnace. *Energy & Fuels*, *30*(3), pp.2458-2473.

[63] Gülder, Ö.L. and Snelling, D.R., 1993. Influence of nitrogen dilution and flame temperature on soot formation in diffusion flames. *Combustion and flame*, *92*(1-2), pp.115-124.

[64] Kumar, P. and Mishra, D.P., 2009. Experimental study of N 2 dilution on bluff-body stabilized LPG jet diffusion flame. *Combustion, Explosion, and Shock Waves*, *45*(1), pp.1-7.

[65] Li, L. and Sunderland, P.B., 2013. Smoke points of fuel–fuel and fuel–inert mixtures. *Fire Safety Journal*, *61*, pp.226-231.

[66] Bhatia, P., Katta, V.R., Krishnan, S.S., Zheng, Y., Sunderland, P.B. and Gore, J.P., 2012. Simulations of normal and inverse laminar diffusion flames under oxygen enhancement and gravity variation. *Combustion Theory and Modelling*, *16*(5), pp.774-798.

[67] Mikofski, M.A., Williams, T.C., Shaddix, C.R., Fernandez-Pello, A.C. and Blevins, L.G., 2007. Structure of laminar sooting inverse diffusion flames. *Combustion and Flame*, *149*(4), pp.463-478.

[68] Lecoustre, V.R., Sunderland, P.B., Chao, B.H. and Axelbaum, R.L., 2012. Numerical investigation of spherical diffusion flames at their sooting limits. *Combustion and Flame*, *159*(1), pp.194-199.

[69] Krishnan, S.S., Abshire, J.M., Sunderland, P.B., Yuan, Z.G. and Gore, J.P., 2008. Analytical predictions of shapes of laminar diffusion flames in microgravity and earth gravity. *Combustion Theory and Modelling*, *12*(4), pp.605-620.

[70] Elbaz, A.M. and Roberts, W.L., 2014. Experimental characterization of methane inverse diffusion flame. *Combustion Science and Technology*, *186*(9), pp.1249-1272.

[71] Bird, R.B., Stewart, W.E., W.E Lightfoot, W.E., Transport phenomena, John Wiley and Sons, New York, USA ,1960, p.571.

[72] Reid, R.C., Prausnitz, J.M. and Poling, B.E., 1987. The properties of gases and liquids.

[73] Smyth, K.C., Miller, J.H., Dorfman, R.C., Mallard, W.G. and Santoro, R.J., 1985. Soot inception in a methane/air diffusion flame as characterized by detailed species profiles. *Combustion and Flame*, *62*(2), pp.157-181.

[74] Zhang, T., Guo, Q., Song, X., Zhou, Z. and Yu, G., 2012. The chemiluminescence and structure properties of normal/inverse diffusion Flames. *Journal of Spectroscopy*, *2013*.

[75] Zhu, H., Hu, C., Guo, Q., Gong, Y. and Yu, G., 2019. Investigation on chemiluminescence and structure characteristics in CH4/O2 diffusion flames. *Experimental Thermal and Fluid Science*, *102*, pp.595-602.

[76] Guo, H., Castillo, J.A. and Sunderland, P.B., 2013. Digital camera measurements of soot temperature and soot volume fraction in axisymmetric flames. *Applied optics*, *52*(33), pp.8040-8047.

[77] Meneses, D.D.S., Melin, P., Del Campo, L., Cosson, L. and Echegut, P., 2015. Apparatus for measuring the emittance of materials from far infrared to visible wavelengths in extreme conditions of temperature. *Infrared Physics & Technology*, *69*, pp.96-101.

[78] Kuhn, P.B., Ma, B., Connelly, B.C., Smooke, M.D. and Long, M.B., 2011. Soot and thin-filament pyrometry using a color digital camera. *Proceedings of the Combustion Institute*, *33*(1), pp.743-750.

[79] Ma, B., Wang, G., Magnotti, G., Barlow, R.S. and Long, M.B., 2014. Intensity-ratio and color-ratio thin-filament pyrometry: uncertainties and accuracy. *Combustion and Flame*, *161*(4), pp.908-916.

[80] Dasch, C.J., 1992. One-dimensional tomography: a comparison of Abel, onion-peeling, and filtered backprojection methods. *Applied optics*, *31*(8), pp.1146-1152.

[81] Guo, H., 2015. *Soot oxidation in hydrocarbon-free flames*(Doctoral dissertation).

[82] Yuan, Z., 1995. The filtered Abel transform and its application in combustion diagnostics, Western Section of the Combustion Institute.

[83] Daun, K.J., Thomson, K.A., Liu, F. and Smallwood, G.J., 2006. Deconvolution of axisymmetric flame properties using Tikhonov regularization. Applied optics, 45 (19), pp.4638-4646.

[84] Lock, A., Aggarwal, S.K. and Puri, I.K., 2009. Effect of fuel type on the extinction of fuel and air stream diluted partially premixed flames. *Proceedings of the Combustion Institute*, *32*(2), pp.2583-2590.

[85] Shu, Z., Krass, B.J., Choi, C.W., Aggarwal, S.K., Katta, V.R. and Puri, I.K., 1998, January. An experimental and numerical investigation of the structure of steady two-dimensional partially premixed methane-air flames. In *Symposium (International) on Combustion* (Vol. 27, No. 1, pp. 625-632). Elsevier.

[86] Azzoni, R., Ratti, S., Aggarwal, S.K. and Puri, I.K., 1999. The structure of triple flames stabilized on a slot burner. *Combustion and Flame*, *119*(1-2), pp.23-40.

[87] Aggarwal, S.K., 2009. Extinction of laminar partially premixed flames. *Progress in energy and combustion science*, *35*(6), pp.528-570.

[88] Holman, J.P., 2010. Heat Transfer (McGraw-Hill Series in Mechanical Engineering).

[89] Hindasageri, V., Vedula, R.P. and Prabhu, S.V., 2013. Thermocouple error correction for measuring the flame temperature with determination of emissivity and heat transfer coefficient. Review of Scientific Instruments, 84(2), p.024902.

[90] Eckert, E.R.G. and Drake Jr, R.M., 1987. Analysis of heat and mass transfer.

[91] Maun, J.D., Sunderland, P.B. and Urban, D.L., 2007. Thin-filament pyrometry with a digital still camera. *Applied optics*, *46*(4), pp.483-488.